Measurement of the momentum spectrum of atmospheric muons with the L3 Detector

D I S S E R T A T I O N

zur Erlangung des akademischen Grades

d o c t o r r e r u m n a t u r a l i u m
(Dr. rer. nat.)

im Fach Physik

eingereicht an der

Mathematisch-Naturwissenschaftlichen Fakultät I

der Humboldt-Universität zu Berlin

von

Dipl.-Phys. Michael Unger
geboren am 1. Dezember 1971 in Donauwörth

Präsident der Humboldt-Universität zu Berlin
Prof. Dr. Jürgen Mlynek

Dekan der Mathematisch-Naturwissenschaftlichen Fakultät I
Prof. Dr. Michael Linscheid

Gutachter:
1. Prof. Thomas Hebbeker (RWTH Aachen)
2. Prof. Nikolaj Pavel (HU Berlin)
3. Dr. Pierre Le Coultre (ETH Zürich)

Tag der mündlichen Prüfung: 9. Februar 2004

ZUSAMMENFASSUNG

In der vorliegenden Arbeit wird die Messung des Impulsspektrums atmosphärischer Myonen beschrieben. Die Messung basiert auf der Analyse von Daten, die mit dem L3-Detektor am Forschungszentrum CERN in Genf in den Jahren 1999 und 2000 aufgezeichnet wurden.
Die Impulsauflösung dieses Detektors wurde mittels einer neuen Spurrekonstruktion entschieden verbessert. Auf diese Weise vergrößerte sich der messbare Impulsbereich um den Faktor 4.3. Für eine möglichst genaue Bestimmung der absoluten Normierung des Spektrums atmosphärischer Myonen wurden die Effizienzen jeder Detektorkomponente eingehend untersucht.

Die Impulsabhängigkeit des atmosphärischen Myonflusses konnte somit im Impulsbereich von 20 bis 2000 GeV und in Abhängigkeit vom Zenithwinkel zwischen 0 und 58^o gemessen werden. Die höchste Präzision wurde um 200 GeV erreicht, wo die absolute Normierung des Flusses mit einer mittleren Genauigkeit von 3.0% bestimmt wurde. Das Verhältnis des Flusses positiver und negativer Myonen wurde bis 630 GeV bestimmt und zeigt keine Impuls- oder Zenithwinkelabhängigkeit innerhalb der experimentellen Fehler. Es beträgt $\langle R \rangle = 1.277 \pm 0.002\,(\text{stat.}) \pm 0.011\,(\text{sys.})$.

ABSTRACT

The subject of this thesis is the measurement of the momentum spectrum of atmospheric muons. The measurement is based on the analysis of data recorded in the years 1999 and 2000 with the L3 detector at the particle physics laboratory CERN in Geneva.
The momentum resolution of this apparatus was improved considerably by a new track reconstruction algorithm, increasing the explorable momentum range by a factor of 4.3. For a precise determination of the absolute normalization of the muon spectrum, the efficiency of each subdetector was studied carefully.

The momentum dependence of the atmospheric muon flux was measured between 20 and 2000 GeV as a function of zenith angle between 0 and 58^o. The best precision was achieved around 200 GeV, where the absolute normalization of the spectrum was determined with an average accuracy of 3.0%. The ratio of the flux of positive to negative muons was measured up to 630 GeV. Within the experimental errors, no dependence on momentum or zenith angle was found. Its average value is $\langle R \rangle = 1.277 \pm 0.002\,(\mathrm{stat.}) \pm 0.011\,(\mathrm{sys.})$.

CONTENTS

Chapter 1

INTRODUCTION

The earth's atmosphere is exposed to a continuous bombardment of high energetic charged particles, usually referred to as cosmic rays. Since their discovery in the beginning of the last century [81], the cosmic ray research has focused on two topics:
Firstly, as these particles are assumed to originate from astrophysical sources, they open a new window for astronomical research. Current activities focus on a precise determination of the chemical composition and the energy spectrum of cosmic rays to learn more about the nature of their origin and mechanisms responsible for their production.
Secondly, cosmic rays constitute a particle beam for high energy physics experiments. Figure 1.1 displays the setup of this giant natural fixed target experiment: Atomic nuclei are accelerated in far distant sources and may finally reach the atmosphere of the earth (the target), where they interact with the atmospheric air nuclei and initiate an avalanche of secondary produced particles, the so called air shower. Before the advent of artificial high energy laboratory accelerators, the investigation of these secondary particles was the major experimental trigger of progress in elementary particle physics. A famous example is the discovery of the positron by Anderson in 1932 [19], which confirmed the theoretical prediction of anti matter by Dirac.
Despite the progress in accelerator techniques, cosmic ray research remained on the particle physics agenda due to the properties of the cosmic particle beam, which are still unrivaled by artificial sources: The highest detected energies in air shower experiments exceed 100 EeV, corresponding to center of mass energies above 400 TeV. This is about a factor 20 higher than the energies which will be available at the 'Large Hadron Collider', which is currently built at the CERN laboratory in Geneva. Even at lower energies, the measured phase space is complementary to that investigated in accelerator experiments. This is because the small-angle forward energy flow is lost in the beam pipe of the accelerator, whereas the air shower experiments are dominated by these forward particles due to the fixed target geometry. The standard theory of

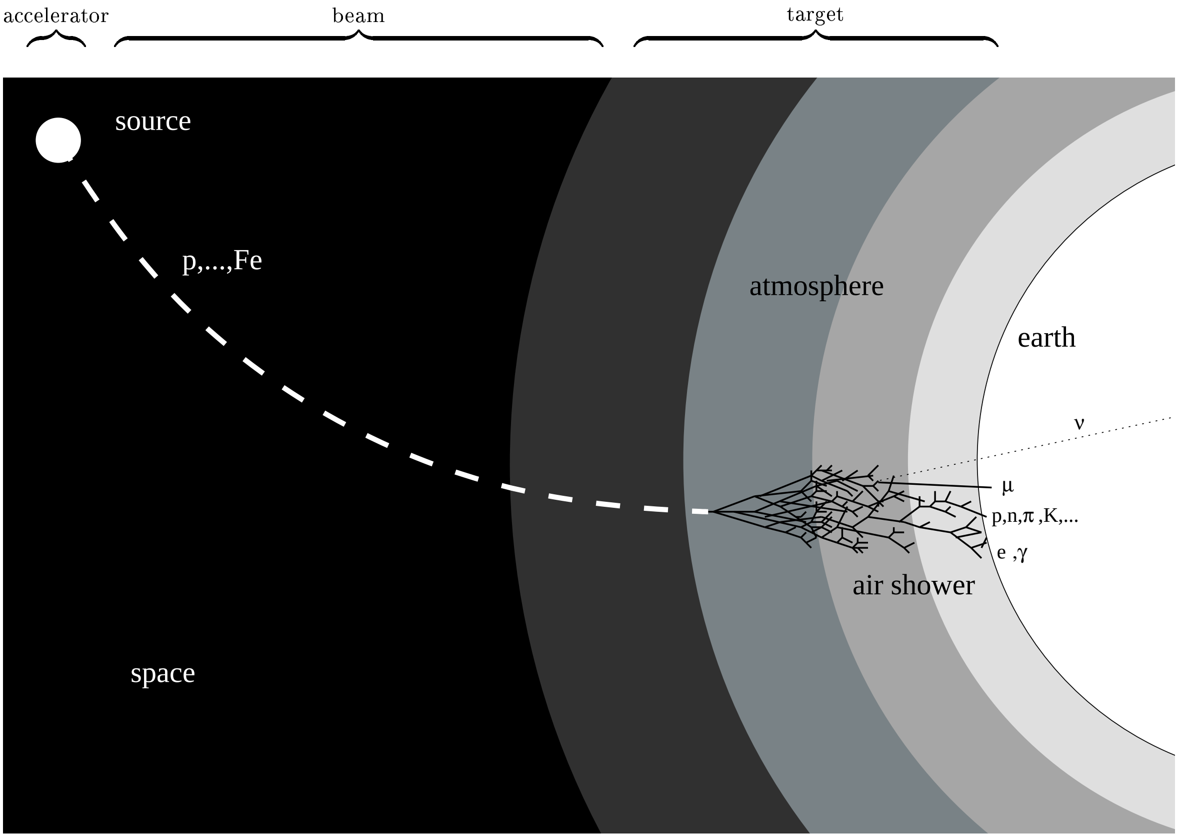

Fig. 1.1: *Schematic view of the cosmic 'fixed target' setup.*

strong interactions, governing the development of the hadronic part of air showers, breaks down in the forward phase space region, therefore its theoretical description relies on models, which still fail to predict all shower observables.

Finally, a large fraction of the secondary particles reaching (and penetrating) the earth are neutrinos. As these particles are known to have a small interaction probability with matter, the detection of them relies on a sufficiently large flux entering the detector. The analysis of atmospheric neutrino data, together with observations of neutrinos originating from the sun and those from artificial accelerators, reveals discrepancies between the measurements [15,18,63] and the standard theoretical expectations [8,83], currently interpreted as the consequence of neutrino oscillations (see [88] for a recent review on this topic).

This work is dedicated to the measurement of muons created in air showers. These elementary particles themselves were first discovered in a cosmic ray experiment in 1937 [114]. Since then, many experiments measured their flux, energy spectrum and the ratio of positive and negative muons. As there is a close relation between the properties of atmospheric muons and neutrinos, which will be further explained in chapter 1, these measurements could in principle be used to constrain the theoretical predictions of the atmospheric neutrino beam and help to interpret the parameters of the above mentioned neutrino oscillations. However, current muon measurements do not agree with each other and the overall uncertainties are between 7 and 31% depending on the energy (see section 2.4).

A new precise measurement is presented here, together with a thorough evaluation of the experimental errors.

The measurement was performed using the precision muon spectrometer of the L3 detector at CERN in Geneva/Switzerland, which was designed to detect muons originating from collisions of the LEP accelerator beam. Starting from the year 1998, the L3 apparatus was equipped with new read out electronics and additional detector components to allow for the measurement of cosmic ray induced muons, too. This new setup, known as L3+C, will be explained in chapter 3. With the new data reconstruction algorithm explained in chapter 4 and the improved momentum resolution, the muon momentum spectrum could be measured in a momentum range between 20 and 2000 GeV* and the charge ratio between 20 and 630 GeV. After the description of the detector performance in chapter 5, the results are presented in chapter 6 followed by a comparison to theoretical predictions based on the current knowledge of the primary particle flux and high energy interactions.

*Throughout this thesis the convention $\hbar = c = 1$ is used.

Chapter 2

ATMOSPHERIC MUONS

Atmospheric muons are amongst the end products of the nuclear cascades initiated by the collision of cosmic ray particles with the air nuclei of the earths' atmosphere. At muon energies below a few TeV, they predominantly originate from the decay of charged π and K mesons via

$$(\pi/K)^+ \to \mu^+ + \nu_\mu \tag{2.1}$$

and

$$(\pi/K)^- \to \mu^- + \overline{\nu}_\mu \ . \tag{2.2}$$

Due to the small energy loss of approximately 2 GeV for a muon traversing the whole atmosphere, their relatively long lifetime of about 2.6 μs and the relativistic time dilatation, most of the muons above 10 GeV can reach the surface of the earth before stopping and decaying.

The parent mesons in (2.1) and (2.2) are produced mainly in the interactions of the primary cosmic nuclei A with the air in the atmosphere:

$$A + \mathrm{Air} \to \pi, K + X. \tag{2.3}$$

Whereas the calculation of the meson decays is governed by the well known kinematics of a two body decay, the main difficulty of a quantitative prediction of the atmospheric muon and neutrino fluxes at the surface of the earth arises from calculating the meson spectra in (2.3). This is because the incoming flux of primary cosmic nuclei is not precisely known and the relevant hadronic cross sections are measured only at low energies and in a limited phase space region. These predictions have gained importance in the last few decades, as the more and more sophisticated neutrino flux measurements revealed a significant difference between the experimental results [15, 18, 63] and theoretical calculations [8, 83].

Because of the close relation of atmospheric muons and neutrinos due to their common origin, a precise determination of the relatively easy to measure muon flux will improve also the knowledge of the neutrino flux. Before giving a more quantitative description of this close relation, the properties of the particle beam impinging on the atmosphere will be reviewed followed by a short description of the atmospheric target.

2.1 The cosmic particle beam

In figure 2.1 the flux of cosmic particles arriving at the earth's atmosphere is shown. The flux is given by the number of particles per time, area, solid angle and energy interval. As can be seen, the observed flux is steeply falling with energy. The measured particle spectrum is covering twelve decades in energy and within this range, the flux drops 32 orders of magnitude.

Below about 100 GeV, the flux is sufficiently large, that the particles can be measured directly in short balloon flights. The energy range until about 100 TeV is covered by long duration balloon flights or satellite experiments. Beyond these energies, only indirect measurements are available. The experimental techniques include air shower arrays, which infer the energy of the primary particle from the number of secondary shower particles observed at ground level, and fluorescence detectors which detect the fluorescence light of showers produced in the atmosphere.

The observed primary spectrum is remarkably featureless and can be described by a simple power law

$$\Phi(E) = \Phi_0 \cdot E^{-\gamma} \tag{2.4}$$

with a spectral index of $\gamma = 2.7$ over a wide energy range between 10 GeV and a few PeV.

At lower energies, not all particles can reach the earth because of the shielding of the geomagnetic field and the solar wind emitted by the sun, and correspondingly the observed spectrum starts flattening below 10 GeV.

Two changes of the spectral index seem to happen at high energies: At a few PeV, a steepening of the spectrum called the 'knee' is observed, when γ changes from 2.7 to about 3. The origin of this change, though discovered about half a century ago [93], is still unclear. A possible explanation is, that at these energies the major mechanism for accelerating the particles starts to get inefficient. This mechanism is currently thought to be a stochastic acceleration [59] in the shock fronts of supernova remnants, which naturally explains the observed power law and can provide particles up to about 100 TeV [100].

Nevertheless, the observed spectrum continues up to 100 EeV, indicating the presence

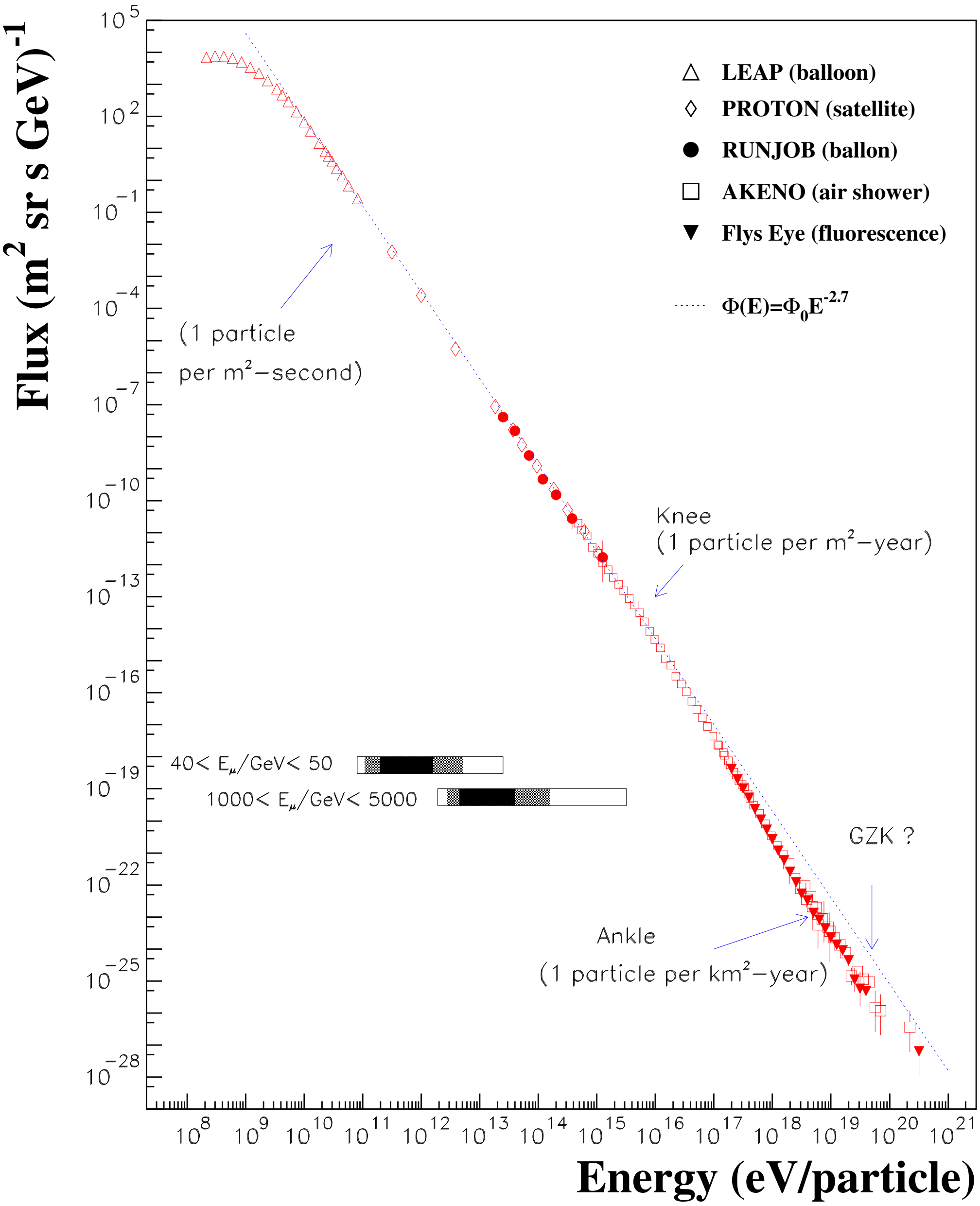

Fig. 2.1: *The primary cosmic particle spectrum as measured by different experimental techniques: Balloon borne spectrometers at low energy [124], satellite measurements [70] and balloon borne emulsion chambers at medium energies [20] and indirect ground based air shower [112] and fluorescence [34] measurements at high energies (figure based on [128]). The boxes in the lower part show the primary energy range causing a fraction of 95 (full box), 90 (shaded area) and 68% (black area) of the total atmospheric surface muon flux at two muon energies according to a simulation with the* ***TARGET*** *shower simulation program.*

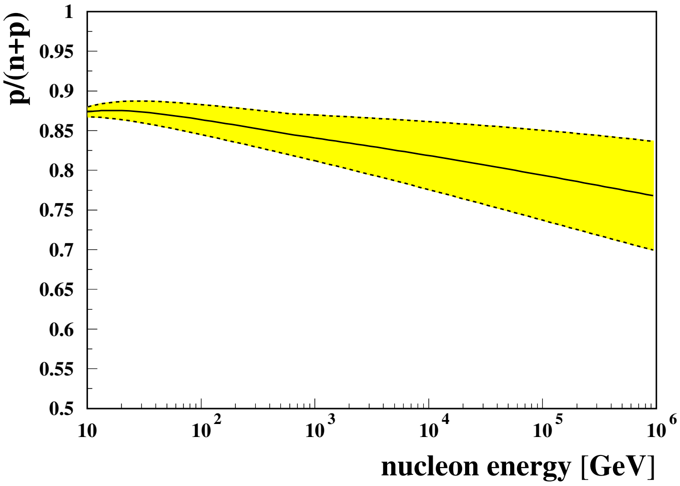

Fig. 2.2: *The fractional contribution of protons to the cosmic nucleon flux. The band denotes the experimental uncertainty as estimated from the difference between different parameterizations of primary flux measurements (see chapter 7).*

of other sources of acceleration (see [64] for a review on this topic) and the spectral slope changes again at the 'ankle' around 10 EeV.
The particles observed at the highest energies are one of the major puzzles of cosmic ray physics, as at these energies the particles should interact with the cosmic microwave background radiation and therefore not be able to reach earth from far distances (the so called Greisen-Zatsepin-Kuzmin cutoff [68, 141]), or originate within our galactic neighborhood at distances <100 Mpc, where no possible sources of such high energetic events are known.
The primary energies responsible for the muons measured in this analysis are estimated with an air shower simulation program [57] and shown as the horizontal areas in 2.1. As can be seen, muons below 5 TeV are mainly originating from the sub-'knee' energy region.

The cosmic nuclei hitting the atmosphere of the earth cover elements from hydrogen up to uranium. The largest fraction of the all nucleon flux is contributed by hydrogen nuclei (75% at 10 GeV/nucleon), followed by helium nuclei which make up 16% of the total flux at 10 GeV/nucleon [75]. Whereas the relative abundances of the different chemical elements can provide informations on the astrophysical objects accelerating the particles, in the light of muon and neutrino production in the atmosphere, mainly the nucleon content of the cosmic particle beam is of interest. The ratio of protons to all nucleons reaching the atmosphere of the earth is shown in figure 2.2 as a function of nucleon energy. It was calculated using parameterizations [38, 65] of current primary flux measurements, which will be further discussed in chapter 7. As can be seen, protons dominate the cosmic nucleons flux over the full energy range currently investigated by direct measurements. At high energies, the proton to nucleon ratio slightly decreases as some of the measurements determined a different spectral index for the primary hydrogen and helium nuclei flux [33].

2.2 The atmospheric target

The atmosphere of the earth consists mainly out of nitrogen and oxygen, contributing to the total number of atmospheric nuclei with a fraction of 0.78 and 0.21 respectively. For the description of the development of the cascades in the atmosphere, it is convenient to use the amount of traversed matter X (often called the 'slant depth') rather than the height h above the ground:

$$X(h) = \int_h^\infty \rho(h')\, dh' \approx X_0\, e^{-h/h_0} \tag{2.5}$$

Here $\rho(h)$ is the air density at a given height and in the last step an approximation for an isothermal atmosphere with scale height h_0 was used.
This approximation gives a good description of the matter profile in the stratosphere at altitudes between 10 and 40 km, where most of the high energetic atmospheric muons are created. For this layer of the atmosphere the scale height h_0 is about 6.4 km and $X_0 \approx 1300$ gcm^{-2}. The ground level slant depth is of the order of 1000 gcm^{-2} corresponding to eleven nuclear interaction lengths and 27 radiation lengths.

The relation (2.5) is valid for vertically incident particles. At reasonably small zenith angles ($\theta \lesssim 60^o$), for which the spherical geometry of the earth can be neglected, it is

$$X(h, \cos\theta) = \frac{X(h)}{\cos\theta}\,. \tag{2.6}$$

As the atmosphere slightly expands in summer due to the rise of the temperature, a seasonal change of h_0 is observed. The possible related influence on the muon fluxes will be further discussed in section 6.4.5.

2.3 Muon and neutrino production in the atmosphere

For the calculation of the ground level muon and neutrino spectra, the particles produced in the interaction of the primary particles with an air nucleus need to be transported through the atmosphere. These secondary particles themselves can interact with the atmospheric material and produce another sub-shower. Therefore a complete description of an air shower requires a complicated set of coupled transport equations, which can not be solved analytically.
Theoretical predictions of the ground level muon and neutrino fluxes are consequently calculated numerically [44, 45, 105] or with a detailed Monte Carlo simulation of the shower development, in which the particles are explicitly tracked from their point of origin to the next interaction or decay [8,32,83,137]. One of these simulation programs, `TARGET` [57], will be further discussed in chapter 7.
Although analytical approximations can not compete with these methods concerning the accuracy of the result, they can provide a useful tool for understanding the dependence of the atmospheric muon and neutrino fluxes on the key input quantities, such as the primary spectrum and the hadronic interaction parameters. Therefore, a widely used analytic approximation will be briefly described here. In the following only the major 'ingredients' will be discussed and the reader is referred to [44, 62, 64] for complete derivation of the formulae.

Primary spectrum:

As seen above, the spectrum of primary particles is well described by a power law in the relevant energy range. In the so-called superposition approximation it is further assumed that a nucleus of mass A with energy E can be treated as A independent nucleons of energy E/A. This simplification is justified by the fact, that at energies relevant for air showers the binding energies of the nucleons can be neglected.
Furthermore, all primary nucleons are supposed to follow the same energy dependence, such that the total nucleon flux reads as

$$\Phi(E) = \Phi_0 \cdot E^{-\gamma} = (n_0 + p_0) \cdot E^{-\gamma} \tag{2.7}$$

where n_0 and p_0 denote the flux of neutrons and protons respectively.

Hadronic interactions:

The cross sections σ_i for an inelastic collision of a particle of type i with an air nucleus is assumed to be constant with energy. This is justified by the observation, that measured particle collision cross sections exhibit only a small logarithmic dependence with the laboratory energy above $p_{\text{lab}} \approx 200$ GeV (see for instance [75]). The related interaction length in units of slant depth is given by

$$\lambda_i = \frac{A\, m_p}{\sigma_i} \,, \tag{2.8}$$

where A is the mean mass number of air nuclei ($A \approx 14.4$) and m_p denotes the proton mass. For small changes dX in the slant depth, dX/λ_i states the probability of particle i to interact with the atmosphere along dX.
The inclusive production of secondary particles of type b in the process

$$a + A \to b + X \tag{2.9}$$

is described by the normalized single particle cross section

$$f(E_b, E_a) = \frac{E_b}{\sigma_{aA}^{\text{inel}}} \frac{d\sigma_{a\to b}}{dE_b} \,, \tag{2.10}$$

where $\sigma_{aA}^{\text{inel}}$ denotes the total inelastic cross section in $a - A$ collisions. For an incoming power law flux of primary particles a, the spectrum of secondary particles of type b is thus given by

$$\Phi^b(E_b) = \frac{1}{E_b} \int_{E_b}^{\infty} \Phi_0^a \, {E_a}^{-\gamma} \, f(E_b, E_a) \, dE_a \,. \tag{2.11}$$

This relation can be considerably simplified under the so called scaling approximation, which states, that at high energies the inclusive particle production f depends only on the fraction of primary energy carried away by the produced secondary:

$$f(E_b, E_a) \approx f(E_b/E_a) \equiv f_{ab}(x) \,. \tag{2.12}$$

Then

$$\Phi^b(E_b) \approx \Phi_0^a \, {E_b}^{-\gamma} \, Z_{ab} \tag{2.13}$$

with

$$Z_{ab} = \int_0^1 x^{\gamma-2} f_{ab}(x) \, dx \,. \tag{2.14}$$

In this way, the details of the hadronic interactions are conveniently hidden in a single number, usually referred to as 'Z-factor'. Unfortunately, data on the particle distributions are sparse and only available at low energies. Moreover they do not cover

model	$Z_{p\pi^+}$	$Z_{p\pi^-}$	Z_{pK^+}	Z_{pK^-}
TARGET [57]	0.043	0.030	0.0096	0.0020
SIBYLL [56]	0.038	0.029	0.0138	0.0020
QGSJET [89]	0.034	0.028	0.0041	0.0025
Gaisser [64]	0.046	0.033	0.0090	0.0028
RMS [%]	13.2	7.3	43.5	17.8

Tab. 2.1: *Parameters of interaction models at meson energies of 100 GeV for a spectral index of 2.7.*

the full phase space region in x and the corresponding theoretical extrapolations cause additional uncertainties [55].
In table 2.1 the Z-factors for meson production in proton-air collisions are listed for a spectral index of 2.7. In the first three rows, the values predicted by the hadronic interaction models discussed in the last chapter are given for meson energies of 100 GeV followed by the numbers used in the analytic calculation of [64]. The root mean square variance shown in the last row gives an estimate of the large uncertainties of the Z-factors.
Despite this differences a clear tendency of $Z_{p\pi^+} > Z_{p\pi^-}$ and $Z_{pK^+} > Z_{pK^-}$ can be seen. The former is the consequence of the conservation of the positive charge of the incoming proton. Pions are produced in processes such as

$$p + A \to p + A' + n\pi^+ + n\pi^- + m\pi^0 \tag{2.15}$$

and the corresponding charge exchange reaction

$$p + A \to n + A' + (n+1)\pi^+ + n\pi^- + m\pi^0 \ , \tag{2.16}$$

where n and m denote the number of produced charged and neutral pions respectively and A' is the remnant of the target nucleus. At the first glance, above formulae seem to suggest $Z_{p\pi^+} \approx Z_{p\pi^-}$ for large multiplicities. However, the larger the amount of produced particles the smaller is their average energy fraction x and due to the steep primary spectrum these slow particles are suppressed by the factor $x^{\gamma-2}$ in the integrand of equation (2.14).
Conservation of the strangeness and baryon quantum numbers S and B are responsible for the difference between the kaon Z-factors. Whereas a positive kaon ($B = 0$, $S = 1$) can be produced together with a hyperon ($B = 0$, $S = -1$), the production of a negative kaon requires at least one associated baryon and an additional strange meson.

As the shower develops through the atmosphere, the particle fluxes attenuate with the slant depth X due to the loss of energy in processes like $a + A \to na + X$. The flux regeneration implied in this formula is taken into account by replacing the interaction length λ_a with the 'attenuation length' Λ_a, given by

$$\Lambda_a = \frac{\lambda_a}{1 - Z_{aa}} \tag{2.17}$$

Numerical values [64] for Λ_a are 120 gcm^{-2} for nucleons and 160 and 180 gcm^{-2} for pions and kaons respectively.

Meson decay:

The muon and neutrino production via the processes (2.1) and (2.2) occur, if the mesons have enough time to decay before they interact in the atmosphere. Their decay length in units of slant depth X reads as

$$d_i = \frac{E\,X\,\cos\theta}{\varepsilon_i} \tag{2.18}$$

where the index i denotes the particle type and E is the particle energy. The factor $\cos\theta$ takes into account, that due to geometrical considerations the distance to traverse a depth X is enlarged for inclined zenith angles θ with respect to the vertical direction. At atmospheric heights where the first interactions of the primary particle take place, i.e. $X \approx \lambda$, above the 'critical energy' ε_i, interaction processes dominate, whereas for $E \ll \varepsilon_i$ almost all mesons decay before they interact. The critical energy is given by

$$\varepsilon_i = \frac{m_i\,h_0}{x_{\text{dec}}}\,. \tag{2.19}$$

Here m_i denotes the meson mass, h_0 is the atmospheric scale height from equation (2.5) and x_{dec} is related to the particle lifetime τ_i via $x_{\text{dec}} = c\tau_i$. Numerical values for a scale height of 6.4 km are $\varepsilon_\pi = 115$ GeV and $\varepsilon_K = 850$ GeV.

Due to momentum and energy conservation the decay products of a meson have fixed energies and momenta in the rest frame of the decaying meson. As a consequence of the small difference between the muon and pion mass, the muon carries most of the energy in the $\pi \to \mu\,\nu$ decay ($\langle E_\mu\rangle/E_\pi = 0.79$ in the laboratory frame). On the other hand the kaon mass is much larger than the muon mass and therefore the muon and neutrino share about the same amount of energy in the $K \to \mu\,\nu$ decay. This is the reason why despite the small Z_{pK} factors, kaons are an important source of atmospheric muon neutrinos.

Energy loss and decay of muons:

Both the energy loss and decay of muons are usually neglected in the analytic flux calculations. However, as in this work the muon spectrum will be measured down to energies of 20 GeV, the two effects are important and it is instructive to estimate their influence on the muon spectrum.
For this purpose, both the mean muon production height as well as the mean production slant depth need to known. In the low energy limit ($E_i \ll \varepsilon_i$), where the interaction and regeneration of the muons' parent mesons can be neglected, the production spectrum of muons in the atmosphere reads as [64]

$$\frac{d\,\Phi_\mu}{dX} \propto e^{-X/\Lambda_N} \tag{2.20}$$

i.e. the muons are created at a mean slant depth of

$$\langle X \rangle = \Lambda_N \ . \tag{2.21}$$

Correspondingly, for the isothermal atmosphere (2.5) the height dependence reads as

$$\frac{d\,\Phi_\mu}{dh} \propto X(h)/\cos\theta \cdot e^{-X/(\Lambda_N \cos\theta)} \tag{2.22}$$

and the mean muon production height as function of zenith angle is

$$\langle h \rangle = \left[\widehat{\gamma} + \log\left(\frac{X_0}{\Lambda_N \cos\theta}\right)\right] \cdot h_0 \ , \tag{2.23}$$

with the Euler constant $\widehat{\gamma} = 0.5772\ldots$ The mean muon production height is thus about 19 km in the vertical direction and 23 km for zenith angles of 60^o.

Neglecting the energy loss along its path, the probability for a muon with energy E to reach the detector height h_d without decaying is

$$P_\mu(E) = e^{-m_\mu/(E\cos\theta)\,(\langle h\rangle - h_d)/x_\mu} \tag{2.24}$$

with the mean muon decay length of $x_\mu = 659$ m.
This decay constitutes a second source of muon neutrinos via

$$\mu^+ \to e^+ \nu_e \bar{\nu}_\mu \tag{2.25}$$

and

$$\mu^- \to e^- \bar{\nu}_e \nu_\mu \ . \tag{2.26}$$

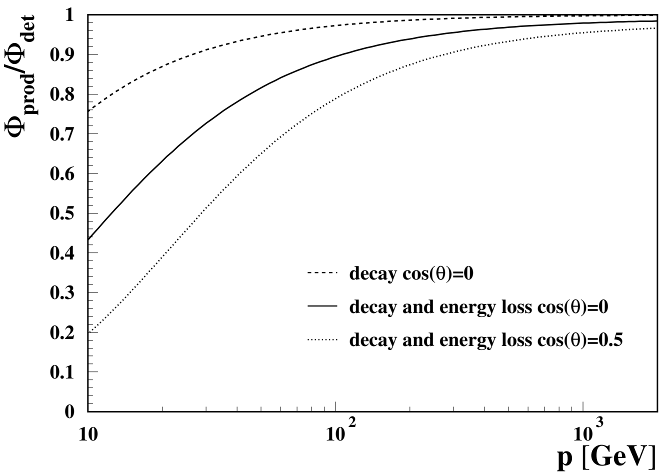

Fig. 2.3: *The ratio of the muon spectrum at production height and detector level.*

The analytic approximations for the spectrum of neutrinos from this decay are more complicated than in the case of the meson decay because of the three particles involved in the final state and the fact, that the polarization of the muon in the meson rest frame needs to be taken into account [28]. However, above 10 GeV the muon decay contributes less than 1% to the overall muon neutrino flux [105] and can be neglected.

Muons are known to suffer energy loss due to ionization and radiative processes of the form

$$\frac{dE}{dX} = a(E) + b(E) \cdot E \,. \tag{2.27}$$

The ionization and radiative coefficients a and b vary only logarithmically with energy. A fit to the energy loss tables in [74] yields $a = 2.82 \cdot 10^{-3}\,\mathrm{GeV/gcm^{-2}}$ and $b = 3.34 \cdot 10^{-6}/\mathrm{gcm^{-2}}$. Integrating the above formula over X, the following relation between the muon energy $\mathcal{E}$ at the observed detector depth X_d and the original energy E at production height $\langle X \rangle$ is obtained:

$$E = \left(\mathcal{E} + \frac{a}{b}\right) e^{b(\langle X \rangle - X_d/cos\theta)} - \frac{a}{b} \,. \tag{2.28}$$

Since $dE/d\mathcal{E} = 1$ for reasonably small detector depths X_d, the two effects can be easily incorporated into the analytic muon spectrum at production height given below by replacing

$$\Phi_\mu(E) \to \Phi_\mu(\mathcal{E}) = P_\mu(E(\mathcal{E})) \cdot \Phi_\mu(E(\mathcal{E})) \,. \tag{2.29}$$

The ratio of the muon spectrum at production height Φ_{prod} to detector level spectrum Φ_{det} is shown in figure 2.3 for two zenith angles. As can be seen, decay and energy loss constitute an important correction to the muon spectrum up to the highest energies. Due to the longer path length the effect gets larger with the zenith angle of the muon.

Analytic approximation of the muon and neutrino flux:

The analytic approximation [44,64] of the muon and neutrino flux at production height can be written as a sum of over the pion and kaon contribution for each lepton $j = \mu, \nu$:

$$\Phi_j(E) = (n_0 + p_0) \cdot E^{-\gamma} \left[\sum_{i=\pi,K} \frac{A_{ij}}{1 + \cos(\theta) E / B_{ij}} \right], \tag{2.30}$$

At very low energies, almost all mesons interact before they decay, and the muon flux and neutrino fluxes have the same spectral index as the primary spectrum. The total normalization with respect to the primary flux is given by the A_{ij} factors:

$$A_{ij} = \frac{R_i \cdot Z_{Ni}}{\gamma(1 - Z_{NN})} \begin{cases} \dfrac{1 - r_i^{\gamma}}{1 - r_i}, & j = \mu \\ (1 - r_i)^{\gamma - 1}, & j = \nu \end{cases} \tag{2.31}$$

Symbols not explained so far are the branching ratios R_i for the decay $i \to \mu\nu$ and the kinematic factors for the meson decay $r_i = (m_\mu / m_i)^2$.
At very high energies, meson decay becomes rare and the lepton spectra steepen one power. The energy of transition between the low and high energy domain is given by

$$B_{ij} = \frac{\gamma \, \varepsilon_i}{(\gamma + 1)} \frac{\Lambda_i \ln(\Lambda_i / \Lambda_N)}{\Lambda_i - \Lambda_N} \begin{cases} \dfrac{1 - r_i^{\gamma+1}}{1 - r_i^{\gamma}}, & j = \mu \\ 1 - r_i, & j = \nu \end{cases} \tag{2.32}$$

Using the numerical values from [64] for primary spectrum, the Z-factors and the attenuation lengths, the following expressions are obtained:

$$\Phi_\mu = \frac{0.14}{\mathrm{cm^2\,s\,sr\,GeV}} (E/\mathrm{GeV})^{-2.7} \left[\frac{1}{1 + \frac{E \cos\theta}{110 \text{ GeV}}} + \frac{0.054}{1 + \frac{E \cos\theta}{760 \text{ GeV}}} \right] \tag{2.33}$$

and

$$\Phi_\nu = \frac{0.018}{\mathrm{cm^2\,s\,sr\,GeV}} (E/\mathrm{GeV})^{-2.7} \left[\frac{1}{1 + \frac{E \cos\theta}{40 \text{ GeV}}} + \frac{0.37}{1 + \frac{E \cos\theta}{720 \text{ GeV}}} \right]. \tag{2.34}$$

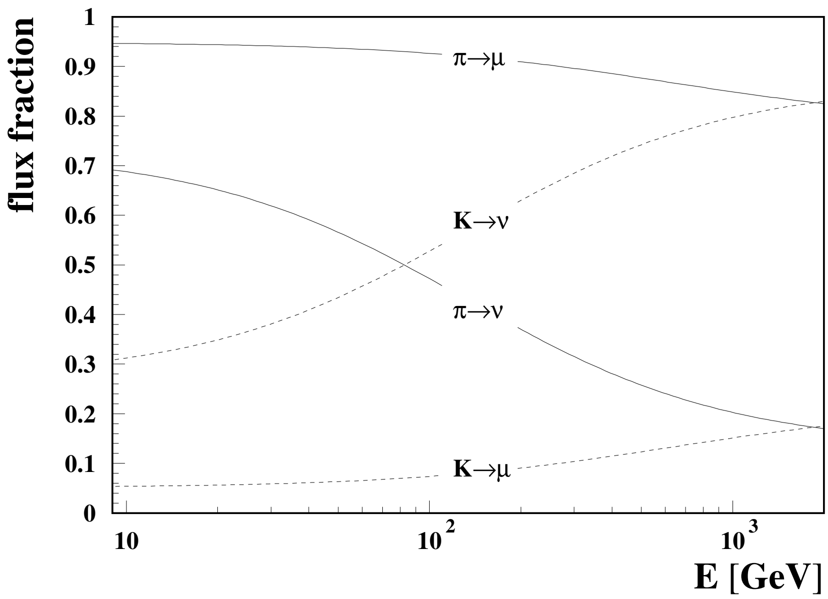

Fig. 2.4: *Relative atmospheric muon and neutrino flux fraction for parent pions and kaons.*

From these formulae and the above considerations, the following conclusions can be drawn:

- The muon flux provides a crucial test for the understanding of hadronic interactions in the atmosphere and the knowledge on the incoming flux of primary nucleons. Given the large uncertainties of these models as exemplified in table 2.1, a good knowledge of the muon flux can help to tune the parameters of air shower simulations.

- There is a close relation between atmospheric muons and neutrinos. The fluxes of the two are determined by the same hadronic interaction parameters. Both are directly proportional to primary flux and nucleon attenuation

$$\Phi_{\mu/\nu} \propto \frac{(n_0 + p_0)}{(1 - Z_{NN})} E^{-\gamma} , \tag{2.35}$$

  i. e. the systematic uncertainties of the neutrino flux related to this parameters can be diminished by a precise knowledge of the atmospheric muon flux.

- However, due to kinematic reasons the correlation between muon and neutrino fluxes is reduced. The kaon contribution to the neutrino flux is much larger than for muons. This is displayed in figure 2.4, where the fractional origin of the neutrino and muon fluxes according to equations (2.33) and (2.34) is shown. Asymptotically, the ν_K flux reaches 87% and the μ_K flux 21%. Consequently, predictions of the neutrino flux will be much more affected by the large systematic error of the Z_{pK} factor.

- The muon charge ratio, which is the ratio of positive to negative muons, is expected to be > 1 because of the positive charge excess on top of the atmosphere. Moreover, the large ratio of Z_{pK^+}/Z_{pK^-} is expected to cause a rise of the muon charge ratio with energy, because of the larger fraction of muons from kaons at large energy. The muon spectrum as a function of charge and energy can thus be used to determine or constrain these factors.

2.4 Experimental status

The muon flux and its dependence on the charge and momentum have been measured many times up to now with various experimental techniques. In the following it will be concentrated on direct ground level measurements. Whereas measurements in the atmosphere performed in balloon flights have the advantage of being able to determine the development of the air shower, their momentum range is limited due to the short exposures possible. Deep underground measurements can reach large momenta due to the shielding of the matter overburden, but they can infer the momentum dependence of the flux only indirectly by the changing threshold energy with the zenith angle.

Conceptually, direct measurements can be subdivided in absolute and relative measurements. The former correct the measured particle rates at the detector to an absolute flux and the latter only measure the momentum dependence of the muon flux. All previous direct vertical measurements, as collected in [79], are displayed in figure 2.5. For the purpose of illustration, in this figure the relative measurements were all renormalized to the same reference spectrum, namely the flux average given in [79]. Moreover, only data points with a precision of better than 20% are shown.

As can be seen, most of the experiments measured in the region below 100 GeV, above this value only a few data points are available with large statistical uncertainties. Furthermore, the scattering of the data points around the mean value is much larger as it would be expected from their statistical error indicating the presence of additional systematic errors not accounted for in the analysis. Excluding some of the worst data sets, a total systematic normalization uncertainty of 7% is estimated in [79]. Due to the small lever arm of the low energy measurement, and systematic differences

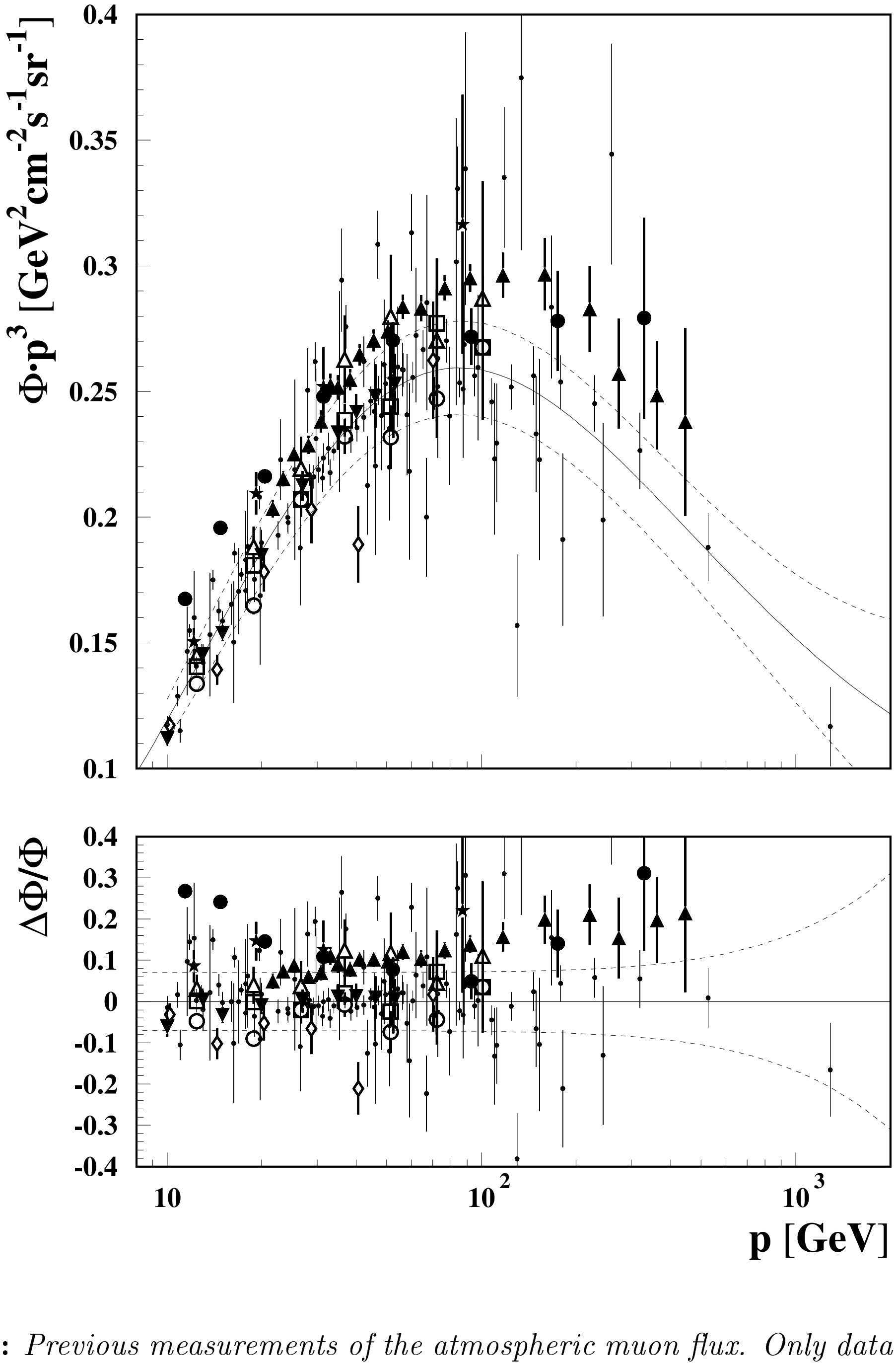

Fig. 2.5: *Previous measurements of the atmospheric muon flux. Only data points with a relative precision of better than 20% are shown. Measurements providing an absolute normalization are $\bullet$: Kiel75 [16], $\blacktriangledown$: AHM71 [31], $\blacktriangle$: MARS75 [22], $\star$: AHM79 [67], $\diamond$: MASS93 [52] and $\circ$, $\square$, $\triangle$: CAPRICE94/97/98 [38, 92]. Small black dots denote experiments, which measured only the relative momentum dependence of the muon flux (see [79] and references therein). The solid line shows the world average fit from [79] with its estimated error (dashed lines). The lower figure displays the relative difference of each experiment to this average.*

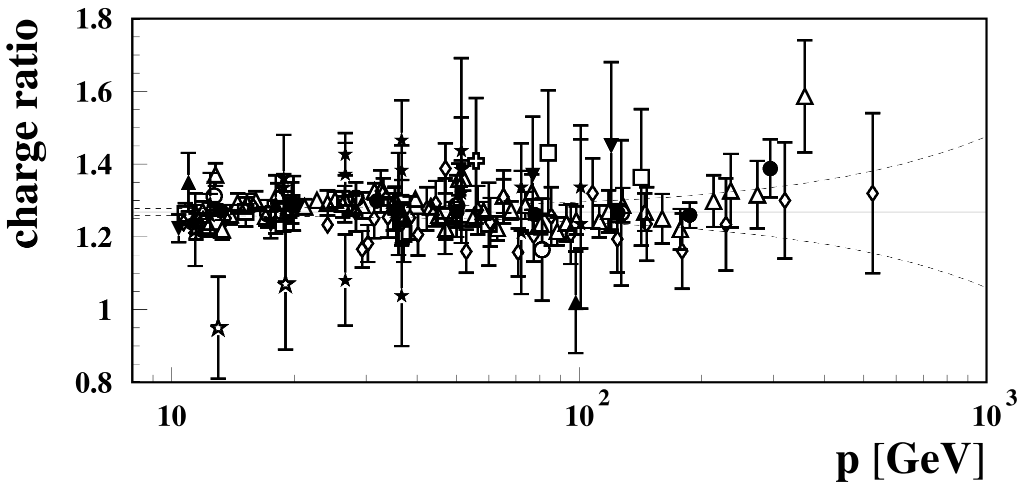

Fig. 2.6: *Previous measurements of the atmospheric muon charge ratio (see [79] and references therein). Only data points with a relative precision better of than 20% are shown. The solid line shows the world average fit from [79] with its estimated error (dashed lines).*

in the measured relative momentum dependence, the overall estimated uncertainty reaches 31% at 2000 GeV.
The existing charge ratio data are displayed in figure 2.6. As in case of the muon flux, not many experiments have data points above 100 GeV.

Given the current experimental status, the following objectives of the measurement described in this thesis can be stated:

- a precise overall absolute normalization to resolve the systematic uncertainties of previous low energy measurements.
- the determination of the spectrum at high energies to close the gap between direct and indirect measurements and to be able to constrain the parameters of atmospheric air shower calculations over a wide energy range.
- the measurement of the high energy muon charge ratio, to be able to constrain the contribution of kaons to the overall muon flux.

Chapter 3

L3+C - EXPERIMENTAL SETUP

3.1 Overview

The L3+C detector [7, 23] is a device to measure the momentum, charge and angle of muons created in air showers. In addition it provides an estimate of the energy of the related primary cosmic ray particle, by sampling the overall number of charged air shower particles at ground level.
It is located at the European Center for Nuclear Research (CERN) near Geneva in Switzerland and consists of an underground muon detector, which is covered by about 30 m molasse overburden and an air shower array at the surface (see figure 3.1). Both detectors are triggered independently and have a separate data acquisition (DAQ). A correlation between the two data streams is achieved by assigning each trigger a precise time stamp, given by a common Global Positioning System (GPS) timing.
The muon detector uses the precision muon drift chambers of the L3 experiment [6], which is one of the four multi purpose detectors at the Large Electron Positron Collider (LEP). For the purpose of measuring atmospheric muons, additional readout electronics and a scintillator array to measure the arrival times of the muons have been installed. An illustration of the L3 detector can be seen in Figure 3.2: Within a large magnetic volume of 1000 m^3 at 0.5 T, several subdetectors are arranged cylindrically around the LEP beam line and the roof of the magnet is covered with approximately 200 m^2 of scintillator tiles. L3+C uses only the scintillators and the sixteen sets of muon chambers. The L3 electromagnetic and hadronic calorimeters and the vertex detectors close to the interaction point are not read out and act therefore as a passive absorber in the middle of the detector.
Due to its shallow depth and its excellent muon momentum resolution, the L3+C muon detector is able to measure atmospheric muons over a wide momentum range spanning from 20 GeV, given by the threshold of the molasse shielding, to 2 TeV, which is the

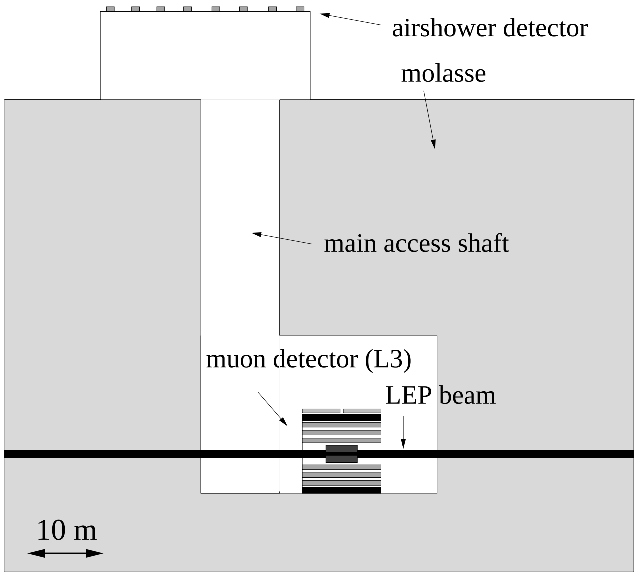

Fig. 3.1: *Schematic view of the L3+C experimental setup.*

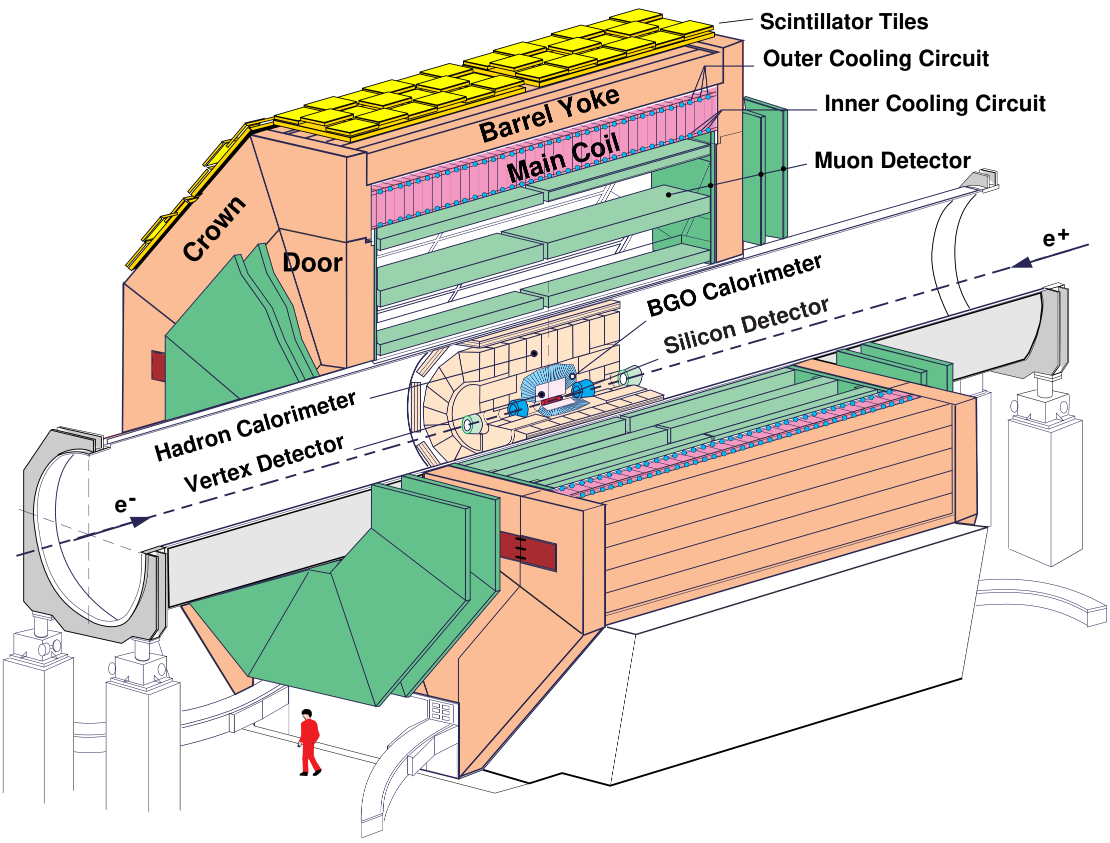

Fig. 3.2: *A perspective view of the L3 detector including the muon chambers and additional scintillators on top of the magnet.*

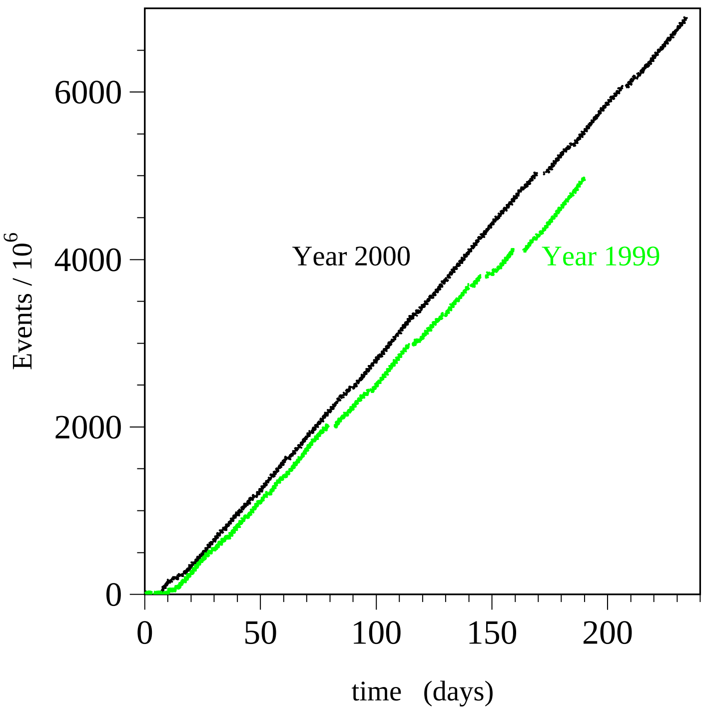

Fig. 3.3: *Collected muon triggers within the two years of data taking of L3+C.*

limit due to the detector resolution and the available statistics. After a short testrun in 1998, L3+C started data taking with the muon detector in May 1999 and continued up to November 2000. Within that period about twelve billion muon triggers have been recorded at an average trigger rate of about 450 Hz. Figure 3.3 shows the number of collected events as a function of time for the two years. The slightly better data taking performance in 2000 is due to improvements of the online system after the experience of the first year of data taking.

The air shower array samples the electromagnetic and muonic particle densities of a shower over an area of $30 \cdot 54$ m^2: Fifty plastic scintillator detectors, each $50 \cdot 100$ cm^2 in area, record the arrival time and energy deposit of the particles, from which the shower core position, direction and primary energy can be estimated. The array became operational in 2000 and about 33 million air shower triggers have been collected, out of which 28% were coincident with a muon trigger. Since this array is not used in the muon momentum measurement, it is not described in detail here and the reader is referred to [7, 139] for a more extensive discussion of its properties.

In the following two coordinate systems will be referred to: The local L3 system, which has its origin in the center of the L3 detector and the surface coordinate system. By convention, the x-axis of the L3 system is pointing towards the center of the LEP ring and the y-axis along the vertical direction towards the surface. The z-axis is along the LEP beam line, which is inclined by about 0.8^o degrees with respect to the horizontal surface. The surface system is 44.8 meter above the center of L3 at a longitude of $6^o01'17''$ E and a latitude of $46^o15'06''$ N. Particle directions are described by their zenith angle θ with respect to the vertical direction and the azimuth angle ϕ with respect to north. The surface is 449 m above sea level. Due to its underground location, the muon detector is shielded by about 7000 gcm^{-2} of molasse overburden.

3.2 Muon chambers

The L3 muon detector [94–97] is arranged in sixteen sets of muon chambers, called octants. On each side of the interaction point of the electron beams, eight of these octants are installed cylindrically around the LEP beam line (see figure 3.2). The octants on the +z side of the L3 coordinate system are referred to as “master” and on the -z side as “slave”. They are numbered counter-clockwise in the xy-plane starting at “3 o'clock” (master: 8-16, slave: 0-7).
An octant consists of three layers of drift chambers measuring the muon track coordinates in the xy-plane perpendicular to the magnetic field. Due to the precision of these devices, they are called P-chambers. The inner- and outermost P-chambers are surrounded by two Z-chambers each, which measure the track coordinates in the yz-plane parallel to the magnetic field.

The L3 muon detector is used to count atmospheric muons and to determine their direction and momentum. The latter is possible, since the Lorentz force acting on the muons inside the magnetic field bends its trajectories to a circle in the xy-plane. With at least three position measurements along the track, the circle radius can be determined which is related to the particle momentum in that plane by

$$p_{xy} = 0.3\,\mathrm{GeV} \cdot q \cdot B/\mathrm{T} \cdot R/\mathrm{m}, \tag{3.1}$$

where R is the circle radius, B is the (constant) magnetic field perpendicular to the track and q is the particle charge. With the additional measurement in the yz-plane, the total momentum can be calculated via

$$p_{\mathrm{tot}} = p_{xy} \cdot \sqrt{1 + \left(\frac{dz}{dy}\right)^2}\,, \tag{3.2}$$

with $\frac{dz}{dy}$ being the track slope in this plane. The accuracy of the momentum determination is of course depending on the resolution of the position measurement. Moreover it is proportional to the magnetic field strength and depends quadratically on the lever arm, over which the track is being measured. L3 reaches an accuracy of about 50 μm for the position measurement within one chamber. The muon spectrometer provides a huge lever arm within a magnetic field of 0.5 Tesla: $B \cdot L^2 = 4.2$ Tm^2 inside one octant and 59.4 Tm^2 over the whole detector. That is why it is considered as a unique precision spectrometer.

3.2.1 P-chambers

The layout of the P-chambers within one octant can be seen in figure 3.4. The three layers are labeled according to their distance to the vertex as inner (MI), middle (MM) and outer (MO) muon chamber. They are filled with a mixture of 61.5% Argon and 38.5% Ethane gas. Argon is the active gas that can be ionized by the muons, whereas Ethane acts as a so called quencher, which is necessary to absorb secondary photons. Each chamber is subdivided into drift cells, which are 10 cm in width. At the edge of a cell cathode mesh wires are installed, in the middle an alternating series of anode sense wires and field shaping wires is placed. A muon that traverses a cell ionizes the chamber gas along its path, and the produced electrons drift towards the sense wires, where the total charge is amplified by the avalanche effect in the rapidly increasing electric field close to the wires. Given the knowledge of the arrival time t_0 of the muon at the chamber, the track coordinates can be reconstructed measuring the arrival time t_e of the drift electrons at the sense wire:

$$x = x_{\text{wire}} + f_x(v_{\text{drift}}, t_e - t_0, dx/dy) \tag{3.3}$$

and

$$y = y_{\text{wire}} + f_y(v_{\text{drift}}, t_e - t_0, dx/dy), \tag{3.4}$$

where v_{drift} denotes the drift velocity of about 48 μm/ns, x/y_{wire} are the wire positions, dx/dy is the track slope and $f_{x/y}$ is the cell map function, which describes the electron drift lines. It is displayed in figure 3.5. Due to the Lorentz force the electron drift paths are bent from the horizontal direction by an angle of approximately 18°. It should be noted, that the drift time measurement contains no information on which side of the sense wire the muon passed the cell. This ambiguity can only be resolved by combining position measurements from several chambers. Similarly, the track slope has to be determined iteratively within the track reconstruction.
To decrease the error on the position measurement inside one chamber, the muon track

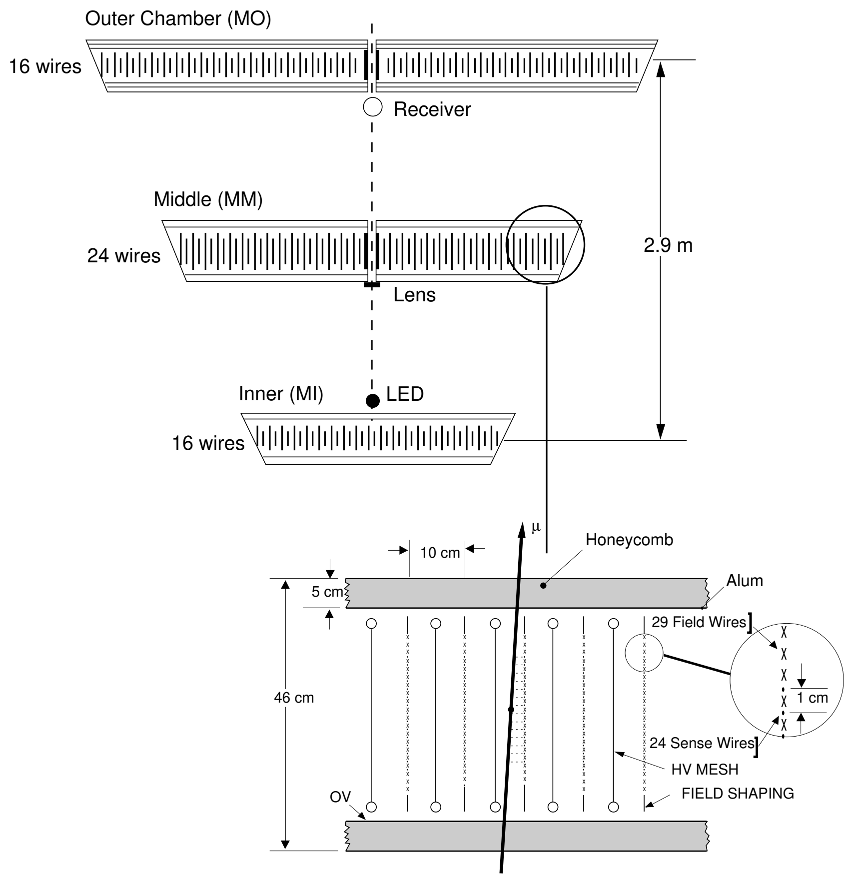

Fig. 3.4: *Schematic view of one octant and the P cells.*

is measured several times along its path through the cell. The number of wires per chamber were chosen to be 16 wires in the MI/MO chambers and 24 wires in the MM chamber. This setup is close to the optimal configuration [66], which minimizes the error on the momentum measurement.

Each octant contains optical systems for the monitoring of the relative alignment of the p-chambers, called RASNIKs [54]. In figure 3.4 the vertical alignment monitoring system (VAS) can be seen: At each end of the octant a light emitting diode (LED) is placed on top of the MI chamber. Its light is passing a lense at the MM plane and the image is measured at the MO plane by analyzing the imbalance of the voltage output of a four quadrant photodiode. The same system is installed along the z-direction at the two edges of each chamber to measure the displacements perpendicular to the wire planes. Since the two outer P-layers are physically divided into two parts, each octant contains nine horizontal alignment systems (HAS).

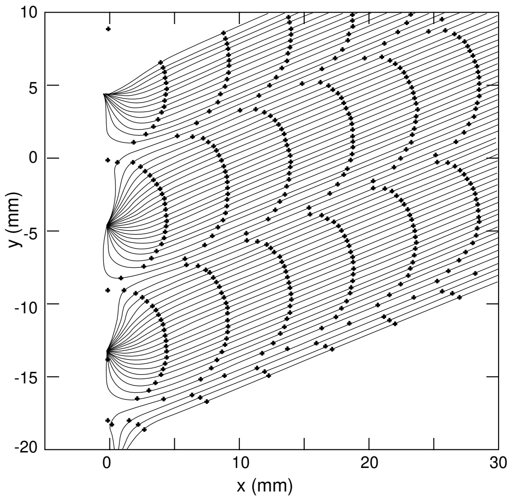

Fig. 3.5: *Electron driftlines within a P-cell. The lines are inclined due to the magnetic field. Black crosses denote points of equal drift times.*

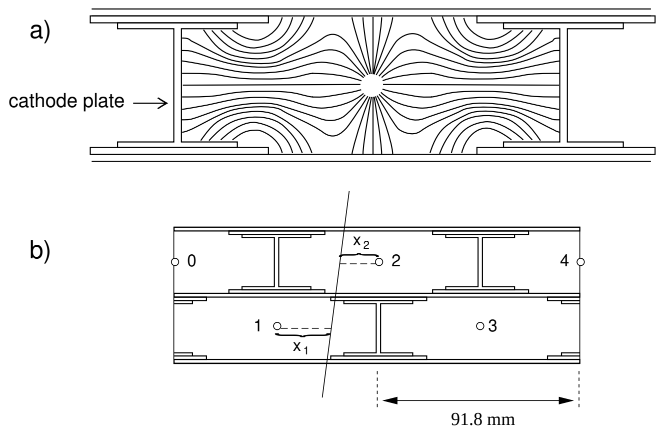

Fig. 3.6: *The electron driftlines within a Z-cell (a) and the layout of a Z-chamber (b)*

3.2.2 Z-chambers

The Z-chambers consist of two layers of drift cells that are shifted by one half cell with respect to each other to resolve left-right ambiguities (see figure 3.6). They are filled with a gas mixture of 91.5% Argon and 8.5% Methane. Each cell contains one signal anode wire and a two aluminum cathode plates. If a muon passes both the MO and MI chamber the position of the track is measured eight times. The resolution of one cell is about 1 mm and the drift velocity is 27 µm/ns.

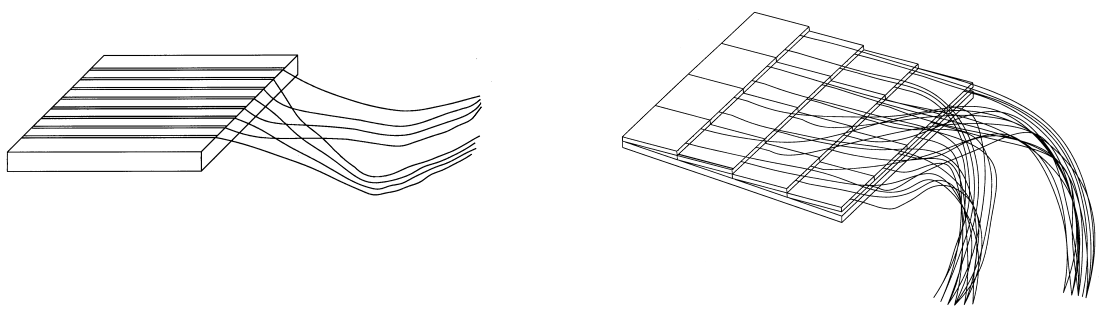

Fig. 3.7: *The layout of a scintillator cassette. Left: A scintillator tile with two groups of wavelength shifting fibers. Right: An assembled cassette consisting of 16 tiles.*

3.3 t_0-detector

As seen in section 3.2.1, the position measurement of the muon track inside the drift chambers requires the knowledge of the arrival time t_0 of the muon. In contrast to L3, where the arrival time is given by the LEP beam crossing, atmospheric muons can reach the detector at any time. Therefore an additional detector was added to the L3 setup: The so called t_0-detector [24] is a 202 m^2 scintillator array covering the roof of the magnet of L3. It consists of 33 modules, each of $2 \cdot 3$ m^2 area, which are composed of six quadratic cassettes, and one $2 \cdot 2$ m^2 module made from four cassettes. The cassettes contain 16 plastic scintillator tiles, which are read out by eight wavelength shifting fibers each (see figures 3.7 and 3.8). If a charged particle traverses a tile, the produced light is collected by the fibers and guided in two bundles to two photomultipliers. Assuring that each bundle is of the same length, in that way a large area can be read out by a small number of photomultipliers with precise timing. The actual number of tiles per photomultiplier is only limited by the size of the photomultipliers' photocathode. In L3+C one photomultiplier reads out 96 tiles corresponding to 6 m^2 scintillator area. The average time resolution, which is achieved, is 1.8 ns.
The main disadvantage compared to commonly used techniques is the small light yield. Only a small fraction of the produced light is guided to the photomultipliers via the fibers. Therefore the photomultipliers have to be operated at high gain and low threshold. The resulting high noise level is suppressed by requiring coincident signals from two photomultipliers, which are connected to the same tile.

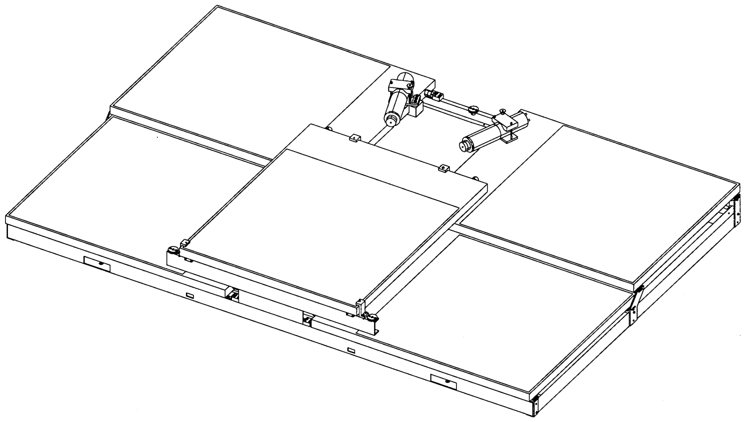

Fig. 3.8: *Full size 6m² module with two photomultipliers.*

3.4 Readout electronics and trigger system

In order to run in parallel with the L3 LEP data taking and to be able to trigger in between the beam collisions, additional electronics were installed for the study of atmospheric muons. Figure 3.9 shows a simplified version of the L3+C readout and trigger chain. After passing a discriminator, the digital signals from the muon chambers are split into two data streams by the so called CPCs (Cosmic Personality Cards) [72]. One stream is directly passed to the L3 readout system, whereas the other is further processed by measuring the signal times with TDCs (Time to Digital Converters) [49] located inside the CPCs. In total 96 wires can be read out by one CPC.
The P-chamber signals are stretched to the maximum drift time within one P-cell (1.2 μs) and a "majority signal" is send to the trigger whenever the number of coincident hits exceeds a programmable threshold. Since one CPC is connected to six MI/MO or four MM cells, this summarized signal can be used to indicate a muon hit within one chamber. The threshold was set to eight hits in 1999 and then decreased to seven hits for the 2000 data to account for cell crossing tracks within the MI/MO cells.
The scintillator signals are discriminated inside the L3CD [102] units and in case of a coincident signal from two photomultipliers of one module, these two triggers are passed to a special CPC card (the scintillator CPC), where again TDCs digitize the signal times. As in case of the muon chamber signals, only the times, but not the pulse height of the signals is measured. To indicate the presence of at least one scintillator

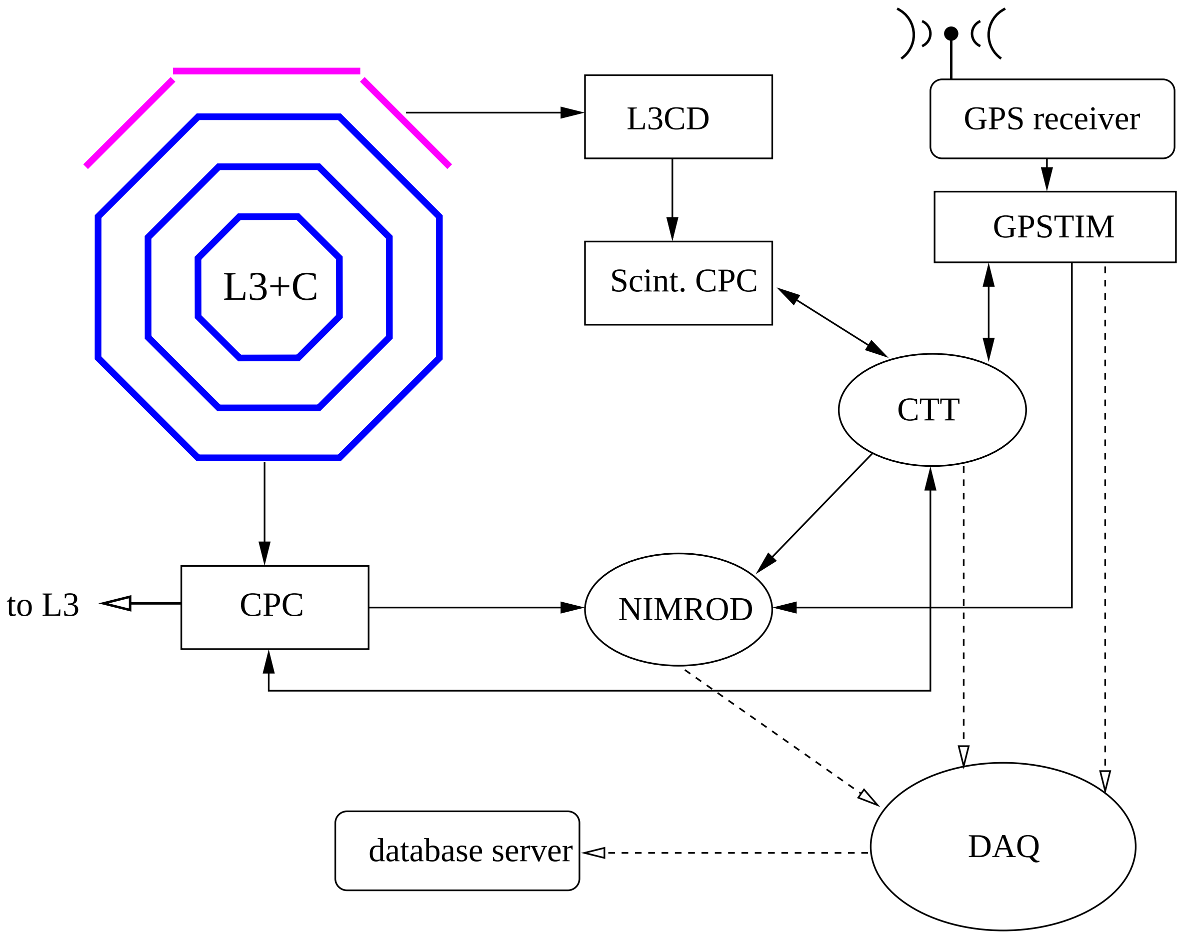

Fig. 3.9: *Simplified L3+C readout scheme.*

hit, the scintillator CPC sends a logical OR of all coincident signals to the trigger.

The decision, whether the event is useful for physics analysis is taken by the CTT (Cosmics Trigger and Timing) module [135]. It receives the majority signals from the P-chamber CPCs and the ORed scintillator signals, out of which the trigger classes listed in table 3.1 are formed:

'Golden' events: Class 1 identifies muons with a precise timing and a fully contained track within one octant.

Octant crossing events: Although L3 provides only alignment information on the chambers within one octant, a considerable increase of the L3+C acceptance may be possible by reconstructing tracks, which pass through several octants. These events are labeled as class 5, 6, 7 and 8.

Efficiency classes: To study the trigger, chamber and scintillator efficiencies, also events without a scintillator hit or less than three hit chambers within one octant are triggered (classes 3, 4, 5, 6, 7, 8 and 9).
Special triggers: Further trigger classes are introduced for special analyses: Class 2 identifies horizontal muons, which are candidates for neutrino induced events, since the L3 detector is shielded by about 24 km of earth from this direction. A search for exotic events, i. e. decays of heavy charged particles [47], is possible by recording triggers fulfilling class 10, 11 and 12 requirements.

Class	Description
1	Three chambers in any octant **AND** a scintillator hit.
2	Three chambers in octant 0 or 4 **AND NO** scintillator hit.
3	Three chambers in octant 1, 2 or 3 **AND NO** scintillator hit.
4	Three chambers in octant 5, 6 or 7 **AND NO** scintillator hit.
5	Three singlets in adjacent octants **AND** a scintillator hit.
6	Two times two chambers **AND** a scintillator hit.
7	Two chambers and two singlets **AND** a scintillator hit.
8	Two chambers and a singlet **AND** a scintillator hit.
9	Two chambers **AND** a scintillator hit.
10	Three chambers and at least one other chamber **AND NO** scintillator requirement.
11	Five chambers (no scintillator requirement).
12	Six or more chambers (no scintillator requirement).

Tab. 3.1: *The twelve CTT trigger classes.*

The event timing is provided by the GPSTIM module [101], which reads out the absolute time from the GPS (Global Positioning System) receiver. Given the exact absolute event time, L3+C is able to search for astronomical cosmic ray point sources and coincidences with other detectors [25]. Moreover the GPSTIM module hosts a 1Hz clock and a 10 MHz live-time counter, which are started at the beginning of a data taking run. Both can be used to evaluate the dead time of the experiment (see chapter 5.3.1).

The event building is done by the NIMROD modules [71, 73], which combine the data from up to 16 CPCs into a single output block.

The data from the trigger, GPSTIM module and the NIMRODs are collected by the data acquisition system (DAQ) [116], which is also responsible for sending information on the run conditions to the data base.

Finally, an event is written to disk, which contains the TDC counts of the drift chambers and the scintillators, the majority signals, trigger classes and the time stamp and live-time information from the GPSTIM module. A typical L3+C event has a size of 1 kB. Therefore the detector produces a data stream of about 500 kB/s, which is well within the maximum data rate of 1 MB/s the DAQ system is able to handle.

Chapter 4

L3+C EVENT RECONSTRUCTION AND SIMULATION

The L3+C event reconstruction from raw TDC measurements to a muon momentum and direction as well as the simulation concept will be explained in this chapter. For a more vivid description, it will often be referred to an example event, which is shown in the figures on the next two pages. In figure 4.1 the graphical display of a fully reconstructed muon track in the magnetic bending plane can be seen, as well as zoomed images of the parts of the P-chambers the muon went through. Figure 4.2 shows the same event in the plane along the LEP beam axis, and a zoomed image of one Z-chamber layer. Several features of a L3+C event, which have to be accounted for in the reconstruction, can be seen:

- **Track hits and ambiguities:** Since the recorded drift times of the P and Z-chambers do not tell, from which side the electrons were approaching the sense wires, at the beginning of the reconstruction, both mirror images of the hit position must be taken into account (see dashed lines in figures 4.1(a-c,e-g) and small crosses in figure 4.2(b)). These ambiguities can only to be resolved by combining the track information from different chambers.

- **Noise hits:** The reconstruction has to cope with signals, which do not originate from a muon, but either from secondary produced particles, or random detector noise: A low energetic track can be seen in the uppermost P-chamber (see figure 4.1(a)), which is presumably a delta ray electron, which was struck off an atom in the massive magnet structure surrounding the muon chambers.
  Beyond that, two scintillator modules recorded a hit, one of which must be due to random photomultiplier noise.

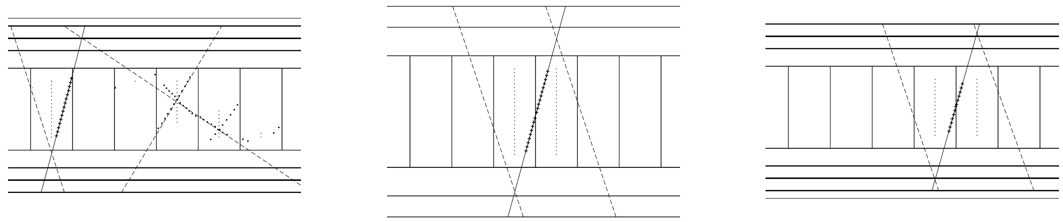

(a) MO/octant 2 (b) MM/octant 2 (c) MI/octant 2

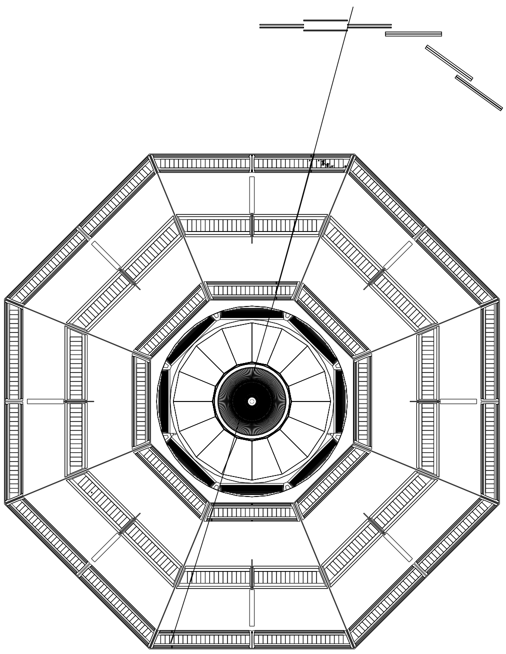

(d) Full view in the xy plane

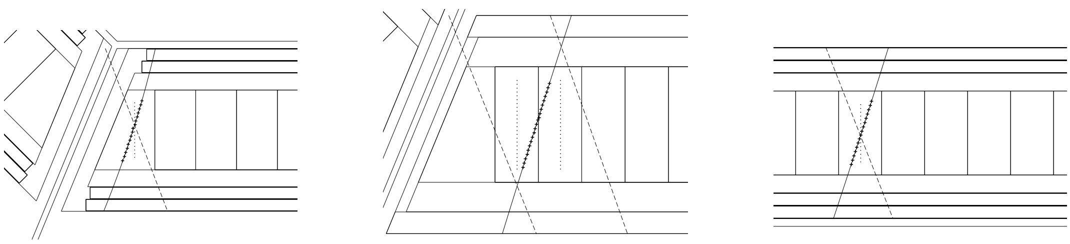

(e) MI/octant 6 (f) MM/octant 6 (g) MO/octant 6

Fig. 4.1: *A reconstructed muon event in the xy-plane: The event contains two scintillator modules with a time signal. Subfigures a-c/e-g are zoomed images of the muon chamber regions with hits. The solid lines denote the fitted track/segments. Dashed lines denote unused segment ambiguities.*

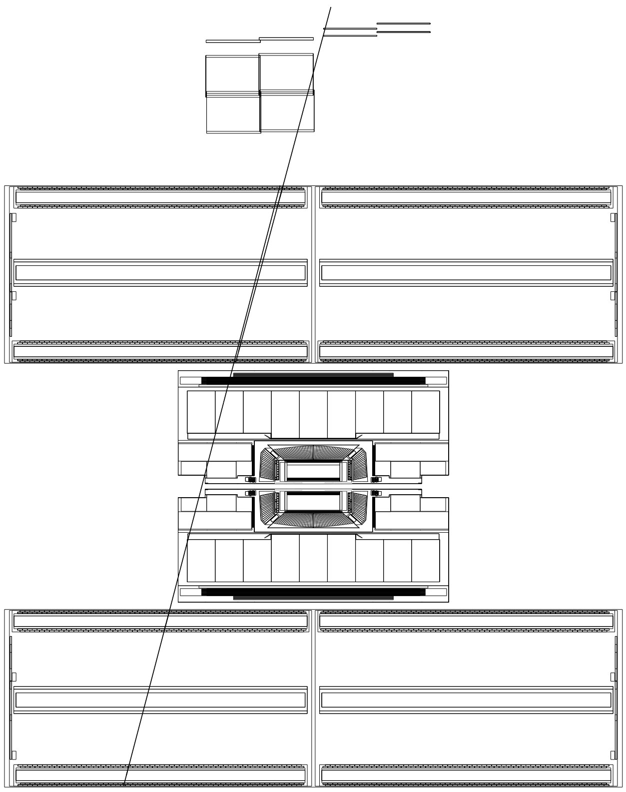

(a) Full view in the yz plane

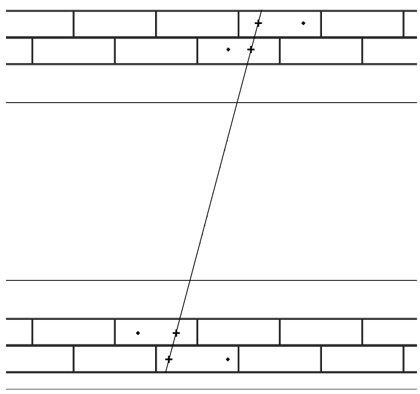

(b) II/octant 2

Fig. 4.2: *A reconstructed muon event in the yz-plane. Subfigure b shows the zoomed view of the II chamber in octant 2 together with the fitted Z-segment*

- **Energy loss inside the detector:** The displayed muon traverses all chambers of two octants. This kind of event is especially useful for the muon spectrum analysis, since the muon track can be measured two times (almost) independently in two different sub detectors. Due to the large number of hits over a long path length, the track parameters can be determined very precisely. On the other hand, for such an event topology, the probability that the muon traverses the L3 inner detectors is rather large. As mentioned in the previous chapter, these detector parts are not read out by L3+C, therefore the reconstruction program has to account for the energy loss and multiple scattering within these detectors. In the example, the muon passes about 2100 g/cm^2 matter, corresponding to about 4 GeV energy loss. At maximum about 3500 g/cm^2 are possible.

- **Multi muons:** Additional problems arise due to the possibility of more than one muon per event. Since the muons of such a multi-muon event usually originate from the same shower, they have parallel directions when entering the detector. However, they can diverge if one of the muons is of sufficiently low energy. So, a priori the reconstruction should not rely on the assumption of single track events.

4.1 Reconstruction algorithm

The reconstruction of an event is organized in the following steps:

4.1.1 Preselection

At least three coordinate measurements are needed for a reconstruction of the tracks' circle parameters in the magnetic bending plane and a good measurement of the arrival time t_0 is essential for the calculation of the drift times inside the muon chambers. Therefore, right after the reading in of the complete event, a preselection based on the CTT trigger classes is imposed. To speed up the reconstruction time, all events not labeled as 'class 1', i. e. having less than three hit chambers within any octant or no scintillator hit, are skipped.
Furthermore, only scintillator hits are selected, for which the time difference between the two photomultiplier measurements is less than 15 ns. In this way random coincidences and t_0 measurements of poor quality due to large time slewing are deselected.

4.1.2 Pattern recognition

If the event is pre-selected, all TDC times are corrected for the relevant time offsets introduced by different read out cable lengths and internal delays of the electronics.
If more than one scintillator hit is present, the coordinates of the muon chamber cells with hits are used to form a rough track, which is extrapolated to the scintillator plane to select the correct scintillator module geometrically. The measured t_0 time of this module is then subtracted from the TDC times of the muon chambers to obtain drift distances according to equations (3.3) and (3.4).

For further processing, the numerous hits within a given muon chamber are condensed into a single object called segment, which is basically the mean coordinate of the track inside the chamber and the track direction at that point. In the xy plane, all possible combinations of hit-pairs of a chamber are connected by a line, and the resulting angles and distances of closest approach to the local cell origin are accumulated in a two dimensional matrix. Despite the helicoidal trajectory of the muon in the magnetic bending plane, this linear approximation is justified, since even low energetic muons show almost no deviation from a straight line* over the small thickness of one P-chamber compared to the matrix spacing of 6.7 mm/10^o. As a positive side effect, very low energetic particles, like the delta-electron in figure 4.1(a), are not properly recognized.
Hereafter, the matrix is scanned for peaks exceeding five hits to make up a segment candidate. This is then fitted with a fast circle-fit algorithm [90] and good quality combinations are kept for further processing.
In the yz-plane, the number of hits inside an octant can be eight at maximum, corresponding to the number of Z-layers. The track model in this projection is a straight line, since the muons within the energy region of interest are not curling inside the detector. All hit combinations with more than two hits inside the outer/inner Z-chambers are fitted with a line to form a Z-segment and are later combined to form a Z-track. Ambiguities are resolved by selecting the combinations with the best fit-χ^2 and the largest number of hits. An example of a Z-segment can be seen in figure 4.2(b).

4.1.3 Sub-track finding

After the pattern recognition phase, the P-segments are combined with the Z-tracks to form a three dimensional sub-track within one octant: The hits of all possible P-

*For instance, a 5 GeV muon deviates 200 μm from a straight line within the MM chamber.

segment combinations are fitted with a circle, connected to a Z-track and extrapolated back to the scintillator planes, to check the scintillator hit preselection. Each track candidate is subsequently refitted taking into account

- the new t_0 time, if the selected scintillator hit differs from the first guess,
- the time of flight from the scintillator to the muon chambers,
- the alignment corrections according to the L3 alignment monitoring system,
- the bending of the P-chamber sense wires due to the gravitational force of 100 μm at maximum and
- the time of pulse propagation of the P-chamber signals along the z-direction from the point the muon passed the chamber to the read out electronics.

The latter four points are the only weak connections between the two track projections in the xy- and yz-plane. Ambiguous sub-tracks, i. e. track candidates sharing one or more segments, are rejected on bases of the best reduced circle fit [90] χ^2 and the maximum number P-segments. However, due to the weak connection of the circle fit to the track direction in the yz-plane, candidates differing by less than 30% in the fit-χ^2 are kept until the final track matching described below.

This octant based procedure evolved [111] from the L3 muon chamber code and the main reason to also adopt the octant confinement constraint for L3+C was, that the relative octant alignment is not measured by the L3 alignment monitors. This geometrical limitation considerably diminishes the L3+C acceptance: Other than muons originating from LEP beam collisions, which are confined within one octant, atmospheric muons can traverse up to four octants.
As it turned out, the octant to octant alignment can be determined from the L3+C data itself (see section 5.2.2), and the current L3+C software development focuses on an algorithm capable to reconstruct all event topologies [103, 123].

4.1.4 Sub-track matching

Because of the possibility that more than one muon of the same shower is crossing the detector, successfully fitted sub-tracks in different octants do not necessarily belong to the same muon. Besides, remaining ambiguities from the sub-track pattern recognition need to be resolved. All possible combinations of high quality upper and lower sub-tracks take part in the global track momentum fit described in the next section. To reduce computation time only sub-tracks with a circle fit χ^2/ndf smaller than 10 are considered. The unambiguous combinations with the best momentum fit χ^2 according to equation (4.8) are selected as real muon tracks. The remaining sub-tracks are matched on basis of the matching χ^2:

$$\chi^2_m = (\mathbf{a} - \mathbf{b})^T(\mathbf{A} + \mathbf{B})^{-1}(\mathbf{a} - \mathbf{b}) \ , \tag{4.1}$$

where $\mathbf{a}$ and $\mathbf{b}$ are the two sub-track parameter vectors and $\mathbf{A}$ and $\mathbf{B}$ denote their covariance matrices using the average track parameter errors estimated in [117].

4.2 Momentum measurement

The basic principle of the L3+C momentum determination is the sagitta measurement s: The sagitta is the deviation of the trajectory of a charged particle inside a magnetic field from a straight line as sketched in figure 4.3. Under the assumption, that this deviation is small in comparison to the track length L and that the magnetic field is perpendicular to the particle trajectory, s can be related to the radius R of the muon trajectory, and equation (3.1) reads as

$$p_{xy} = 0.3\ q\ B/\mathrm{T}\ \frac{L^2/\mathrm{m}^2}{8s/\mathrm{m}}\ \mathrm{GeV}, \tag{4.2}$$

where again B is the magnetic field and q the charge of the particle with momentum p. For the L3+C setup the sagitta measured inside one octant is given by

$$s_s = 0.157\ \mathrm{m\ GeV} \cdot \frac{1}{q \cdot p_{xy}}, \tag{4.3}$$

and using the whole track length over two facing octants the sagitta reads as

$$s_d = 2.21\ \mathrm{m\ GeV} \cdot \frac{1}{q \cdot p_{xy}}. \tag{4.4}$$

As can be seen in figure 4.3 the sagitta inside one octant can be directly calculated from the segment coordinates s_{1-3}:

$$s_s = s_2 - \frac{s_1 + s_3}{2}\ . \tag{4.5}$$

These equations are helpful for a qualitative understanding of the momentum measurement and its errors, but they assume a perfect helicoidal trajectory of the muon inside

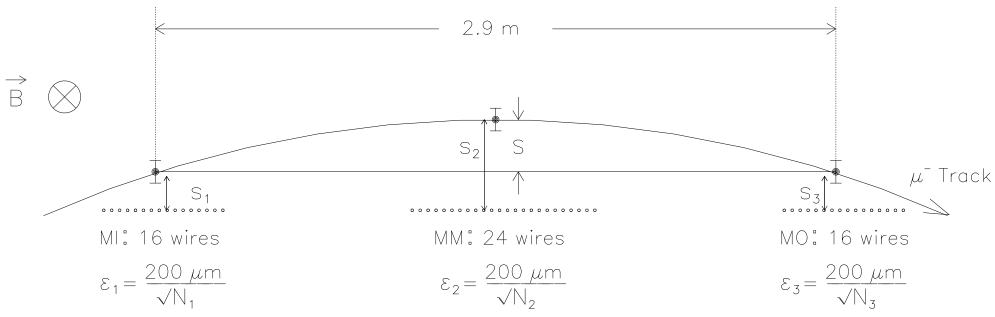

Fig. 4.3: *Explanation of the sagitta: A muon track passing the three chambers of an octant at points s_{1-3}, deviates from a straight line by the sagitta s.*

the magnetic field. In reality, the situation is more complicated: Firstly, the L3 magnetic field strength is not constant over the full detector volume, but varies from 0.47 to 0.51 T. Secondly, the material of the various L3 subdetectors causes energy losses of the muon, leading to a subsequent increase of the radius of the muon trajectory. Likewise, multiple scattering deviates the particle path from an ideal helix. This is accounted for by using the `GEANE` [85] package for the final muon track fit. Being based on the `GEANT` [42] program, it is able to track charged particles through inhomogeneous magnetic fields and due to the coupling to the L3+C detector simulation, it can predict the average energy loss due to ionization and radiative losses for a given muon trajectory. So, for a muon at a plane y^j with the inverse charged momentum $(q/p)^j$, intercept coordinates x^j and z^j and local slopes $\alpha^j = (dx/dy)^j$ and $\beta^j = (dz/dy)^j$, it can predict the track parameters

$$\hat{\mathbf{b}}^i(\mathbf{b^j}) = ((\hat{q}/\hat{p})^i, \hat{x}^i, \hat{z}^i, \hat{\alpha}^i, \hat{\beta}^i) \tag{4.6}$$

at a plane y^i. Due to the stochastic nature of the energy loss and multiple scattering, the true trajectory can not be predicted for a single event, therefore $\hat{\mathbf{b}}$ denotes the *average* trajectory, around which the true parameters $\mathbf{b}$ are distributed with the covariance

$$W^i_{kl} = \langle(\hat{b}^i_k - b^i_k)(\hat{b}^i_l - b^i_l)\rangle\ . \tag{4.7}$$

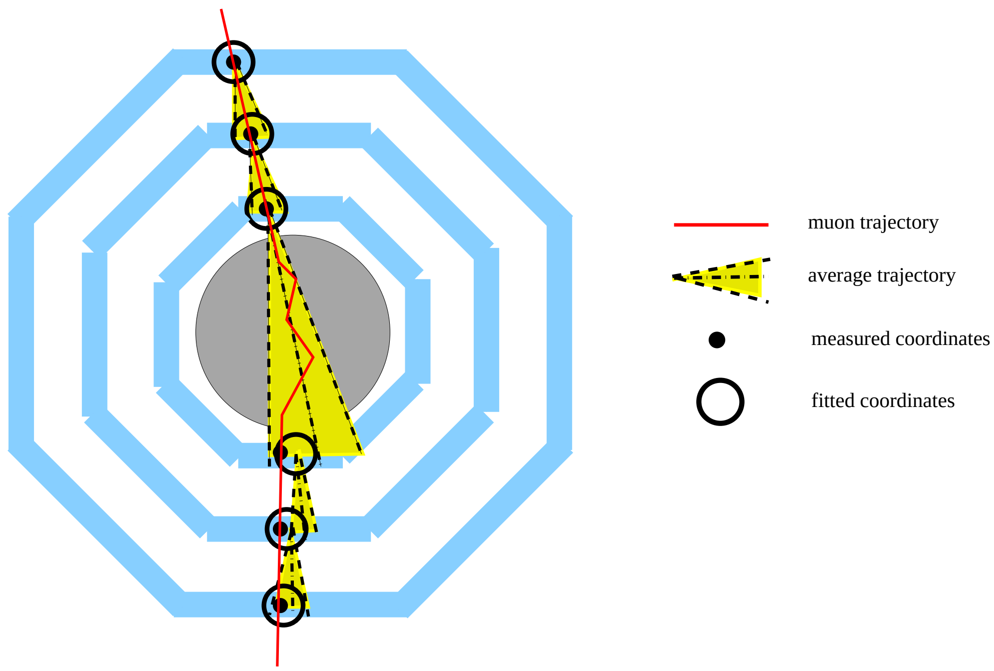

Fig. 4.4: *Illustration of the double octant fit. The resulting fitted coordinates are a compromise between the measurement and the* `GEANE` *prediction.*

In addition to the track prediction, `GEANE` also provides an estimate of this covariance, based on a Gaussian approximation of the fluctuations. Especially for the energy loss, this turns out to be a rather crude model, since the fluctuations are known to follow a Landau distribution.

Using these `GEANE` abilities together with a precise knowledge of the magnetic field strength as function of position [41], the parameters of the muon track can be estimated as illustrated in figure 4.4:

For each chamber, the true track parameters $\mathbf{x}^i$ are fitted as a compromise between the measured and predicted average values by minimizing

$$\chi^2 = (\mathbf{m}^1 - \mathbf{x}^1)^T (\mathbf{V}^1)^{-1} (\mathbf{m}^1 - \mathbf{x}^1) + \sum_{i=2}^{N} \left[(\mathbf{m}^i - \mathbf{x}^i)^T (\mathbf{V}^i)^{-1} (\mathbf{m}^i - \mathbf{x}^i) + (\hat{\mathbf{b}}^i - \mathbf{x}^i)^T (\mathbf{W}^i)^{-1} (\hat{\mathbf{b}}^i - \mathbf{x}^i) \right] . \qquad (4.8)$$

Here $\mathbf{m}^i$ denote the experimental measurements and $\hat{\mathbf{b}}^i$ are the `GEANE` predictions of the track parameters at chamber i given the initial values $\mathbf{x}^{i-1}$ with their corresponding covariance matrix $\mathbf{W}^i$. The total number of available planes N is either three or six, depending on the fit strategy (see below). The covariance matrix $\mathbf{V}^i$ contains the

measurement errors from the segment fit. Track parameters, which are not measured by construction like q/p and z in the MM chamber, or due to dead detector parts, get assigned an infinite error, corresponding to a weight of zero in the inverse covariance matrix. The minimization of equation (4.8) follows the method described in [84] and needs usually not more than three iterations until it converges.
Using this procedure, the L3+C muon reconstruction follows two strategies to determine the muon momentum and direction:

(a) Single octant fit

Inside one octant of the L3 muon spectrometer, energy loss and multiple scattering are of minor importance, since it is essentially matter free (the detector gas and the chamber material amount to approximately 7 gcm^{-2}). In addition, the relative alignment of the chambers is known from the alignment monitoring system. If a muon traverses all three chambers of two different octants, like the example event of figure 4.1, two almost independent measurements of the same track are available. These are back-tracked to a common reference plane, chosen as the inner surface of the upper part of the magnet, where a comparison of the two measurements can be used to determine the momentum resolution (see next chapter). Finally, their weighted average

$$\mathbf{c} = (\mathbf{A}^{-1} + \mathbf{B}^{-1})^{-1}(\mathbf{A}^{-1}\mathbf{a} + \mathbf{B}^{-1}\mathbf{b}) \tag{4.9}$$

can be calculated. Here **a** and **b** denote the individual track measurements in the different octants and **A** and **B** are the covariance matrices of the single octant fit propagated to the plane of combination.

(b) Double octant fit

So far only a small part of the available lever arm of the muon track was used for determining the track curvature. For sub-tracks with equal covariances, the weighted average (4.9) improves the track parameter resolution only by a factor of $\sqrt{2}$. By fitting the measurements of all six traversed chambers at the same time, denoted as 'double octant fit' in the following, the minimum possible resolution of the L3 muon chamber setup can be achieved. In case of an optimum [66] muon chamber configuration, an improvement of the momentum resolution proportional to the square of the projected

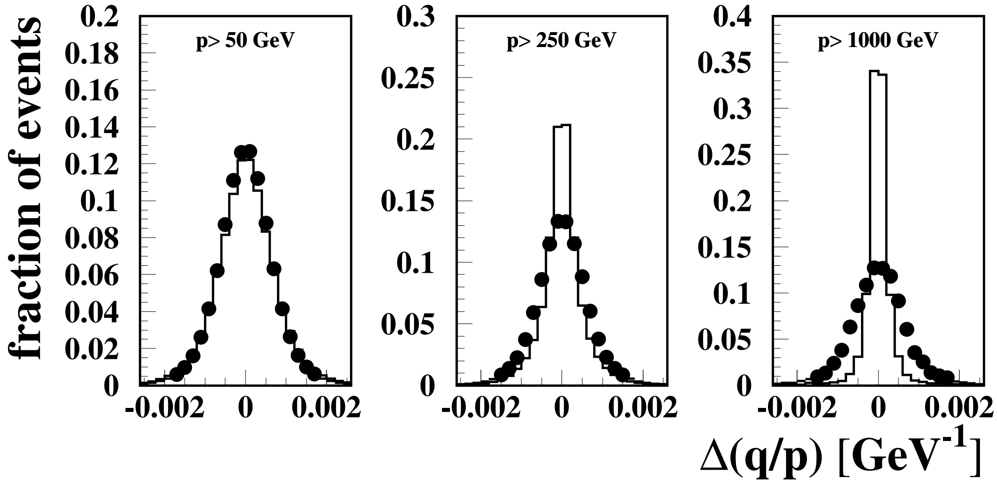

Fig. 4.5: *Comparison of the momentum resolution of simulated muons for different energy thresholds. The dots are the resolution of the weighted average obtained from the single octant fit according to equation (4.9), the solid histogram is the result of the full detector double octant fit.*

track lengths could be achieved:

$$\left(\frac{\sigma_{\text{single}}}{\sigma_{\text{double}}}\right)^{\text{opt}} = \frac{L^2_{\text{single}}/\sqrt{2}}{L^2_{\text{double}}} = \frac{1}{9.9} \tag{4.10}$$

Here L_{single} denotes the distance of 2.9 m between an MI and an MO chamber within one octant, and L_{double} is the distance of 10.9 m between two MO chambers of two facing octants. The L3 muon chamber were however designed for the single octant measurement and correspondingly, the double octant configuration is not optimal. Nevertheless, a numerical evaluation with the ansatz from [66] leads to an expected improvement of the momentum resolution, which is still close to optimum value:

$$\left(\frac{\sigma_{\text{single}}}{\sigma_{\text{double}}}\right)^{\text{L3}} = \frac{1}{8.5} \ . \tag{4.11}$$

This idealized approach neglects the influence of multiple scattering and the stochastic energy loss in the detector material in the middle of the L3 detector on the momentum resolution. Therefore, at low energies, where these processes gain importance, the momentum resolution improvement is expected to be much smaller.
Moreover, L3 does not monitor the relative alignment of different octants. The calibration of this alignment offsets will be discussed in section 5.2.2.

Figure 4.5 shows a comparison of the momentum resolution of the two fitting algorithms using the full L3+C MC simulation*. The difference of the reconstructed and generated inverse charged momentum is shown, which is proportional to the sagitta difference and expected to be Gaussian in the absence of multiple scattering. For all the three momentum thresholds, both methods reproduce the generated momentum on average, thus it can be concluded, that `GEANE` provides a bias-free estimate of the energy loss inside the detector. Secondly, the double octant fit shows the same performance as the single octant fit at low energies, but results in a much better momentum resolution for high energetic muons. A more quantitative estimate of the corresponding resolutions and scale uncertainties will be given in section 5.2.3.

4.3 Detector simulation

As any other modern particle physics experiment, L3+C needs a precise detector simulation to interpret its measurements. It is needed to evaluate the geometrical acceptance of the used apparatus as well as its response to the signal which should be measured.

Figure 4.6(b) illustrates the flow of the L3+C simulation chain: The fast muon generator `l3cgen` [78] is used to generate single atmospheric muons on a horizontal surface around the L3 detector. It contains the parameterization of the momentum and zenith angle distribution of atmospheric muons as obtained using the output of a detailed shower simulation running the `CORSIKA` program [80] together with the interaction models `VENUS` [138] and `GEISHA` [60] and a primary proton spectrum falling proportional $E^{-2.7}$.

The simulated phase space is chosen from muon momenta between 5 GeV and 10 TeV and a zenith angle from 0 to 66 degrees. For efficiency reasons, the generator surface was chosen to be zenith angle dependent:

$$S(\cos\theta) = (a_x + b_x \cdot \cos\theta + c_x \cdot \cos^2\theta)(a_z + b_z \cdot \cos\theta + c_z \cdot \cos^2\theta) \; , \qquad (4.12)$$

with coefficients a_i, b_i and c_i listed in table 4.1. These parameters were determined in [118] by demanding, that less than 0.2% of the tracks, which are reconstructed after the detector simulation, are generated outside this surface. For the tight geometrical constraints applied in the track selection of this analysis (see section 6.2), the generator area is thus large enough for a precise evaluation of the detector acceptance.

*Note: The MC contains no chamber or octant mis-alignment. The momentum smearing explained in the next chapter is already applied here.

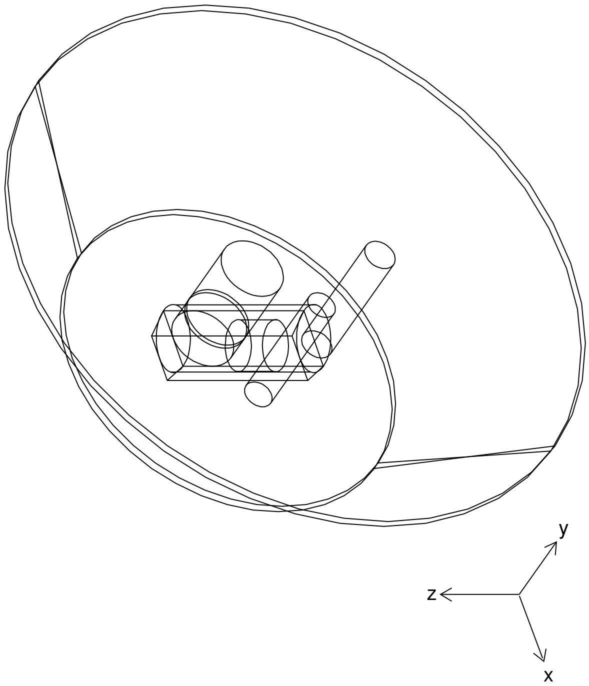

(a) *The simulation of the L3+C surroundings.*

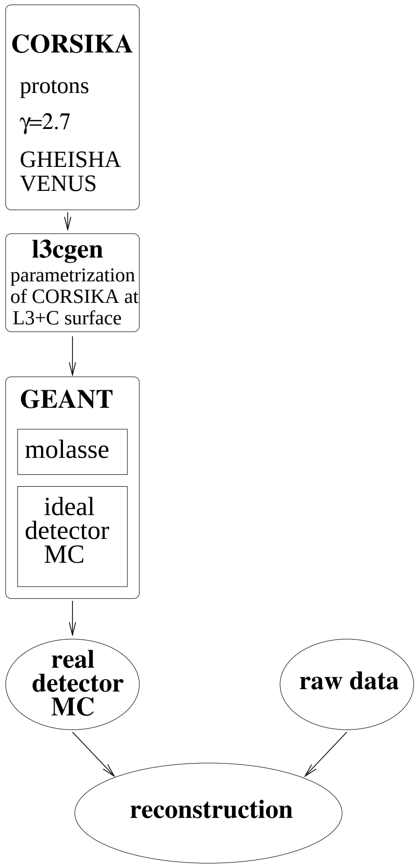

(b) *Flow chart of the L3+C simulation chain.*

Fig. 4.6: *The L3+C muon simulation.*

	a [m]	**b** [m]	**c** [m]
x	51.02	-79.56	38.76
z	56.48	-65.31	25.25

Tab. 4.1: *The `l3cgen` generator surface coefficients*

From the generator surface at detector level, the generated muons are geometrically extrapolated back to the surface above L3+C and passed to the `GEANT`* simulation of the molasse overburden and the ideal detector. For this part of the simulation, the scintillator array on top of the L3 magnet and the geometry of the access shafts and detector hall were added to the existing detailed L3 code [91, 111]. The `GEANT` simulation therefore includes the energy loss and multiple scattering of a muon on its way through the molasse to the detector, and the generation of scintillator signals and muon chamber hits as well as accompanying production of delta electrons close to and within the detector. Figure 4.6(a) shows the model used for the simulation of the L3+C surroundings consisting of a molasse cone containing three access shafts and the main L3 experimental hall. The implementation of the various L3 subdetectors is visible in the event scan pictures at the beginning of this chapter.

After the ideal detector simulation, the imperfectnesses of the real detector are applied:

- The scintillator t_0 times are smeared according to the time resolution of the photomultipliers (see [91]).
- The mean scintillator noise, as measured by the L3CD monitoring system, is added.
- The simulated drift times in the muon detector are smeared according to the measured P- and Z-chamber single wire resolution (see section 5.2.3).
- Hits in dead P- and Z-chamber cells (see section 5.2.1) are not used.

The simulated scintillator and drift chamber TDC times are then passed to the reconstruction program and processed exactly the same way as the raw data.

4.4 Performance of the algorithms

The efficiency of the reconstruction algorithm can be studied comparing the number of class 1 (i. e. potentially triplet) events to the number of reconstructed events. In 1999, on average 88.0% of all class 1 events are reconstructed, the corresponding number for the year 2000 is 84.4%.

*The L3+C `GEANT` version is based on `v3.14` extended with the high energy muon interaction code from [39].

source		**1999**	**2000**
SCNT	scintillator noise	0.024	0.030
	Δt_{PM}	0.022	0.023
	SCNT TDC ε	0.007	0.006
MUCH	momentum too low	0.014	0.014
	bad cells	0.011	0.005
	no Z-track	0.006	0.005
	event loss	0.026	0.071
	misc.	0.008	0.009
total inefficiency		0.118	0.163

Tab. 4.2: *Classification of the reconstruction losses according to various sources for the two data taking periods as observed in two data taking runs recorded in 1999 and 2000.*

To understand these numbers, for each data taking year one run with $\varepsilon_{\mathrm{run}}^{\mathrm{rec}} \approx \langle \varepsilon^{\mathrm{rec}} \rangle$ was carefully studied to break down the inefficiency into its various sources as shown in table 4.2:

- During the scintillator hit filtering process, about 5% of the tracks are deselected, because either the time difference Δt_{PM} between the two photomultiplier measurements of the same scintillator signal is too large or they are considered as a random coincidence of a muon chamber signal and a scintillator noise hit.

- For further 0.7%, the trigger registered a scintillator hit, but no time measurement is present from the TDCs.

- The single octant momentum fit fails for 1.4% of the data, because the track energy is too low.

- About 1% of the events are not reconstructed, as some of the muon chamber hits, which caused the trigger, are inside a drift cell considered as bad (see section 5.2.1).

- As the trigger does not check the number of hits in the Z-chambers, some of the events can not be reconstructed, because no Z-track can be derived if less than two hits were recorded.

- Furthermore, a large fraction of events is lost due to an error in the program, which inhibits the reconstruction of the full event. The total amount of events lost due to this flaw depends on the number of Z-hits, which are deselected in the reconstruction, because they were recorded in a 'bad' Z-cell (see next chapter). This event loss is therefore different for data and MC and the two data taking periods. As a reprocessing of the full data and MC set with a revised version of the algorithm was considered unfeasible, the event loss factors were determined from a small re-reconstruction with high precision. Due to the randomness of the event loss occurrence, no dependence on the muon momentum, direction or any other variable is observed. The obtained factors for data and MC read as follows:

		1999	**2000**
data		0.9689±0.0001	0.9202±0.0001
MC	5-20 GeV	0.8544±0.0009	0.8400±0.0009
MC	20-50 GeV	0.8680±0.0002	0.8568±0.0002
MC	50-100 GeV	0.8709±0.0002	0.8588±0.0002
MC	100-200 GeV	0.8699±0.0002	0.8574±0.0002
MC	200-500 GeV	0.8696±0.0002	0.8563±0.0002
MC	500-1000 GeV	0.8677±0.0003	0.8528±0.0003
MC	1000-10000 GeV	0.8649±0.0004	0.8483±0.0004
MC	20-10000 GeV	0.8688±0.0003	0.8568±0.0003

Tab. 4.3: *Event loss factors for data and MC for the two data taking years.*

In this analysis, only events reconstructed with the double octant fit are used because of their good momentum resolution. Since the fit does not always converge, an inefficiency is introduced by this selection, which must be accounted for in the detector acceptance calculation. As shown in figure 4.7, the fit efficiency varies with momentum and the amount of matter density X traversed by the track. No such variation is observed in the original detector simulation (not shown), where the efficiency is close to one independent of momentum and X. The behavior at high momenta can be explained by the fact, that in the measurement errors $\mathbf{V}^i$ in equation (4.8) neither alignment nor calibration uncertainties are considered. Whereas at low momenta or large traversed

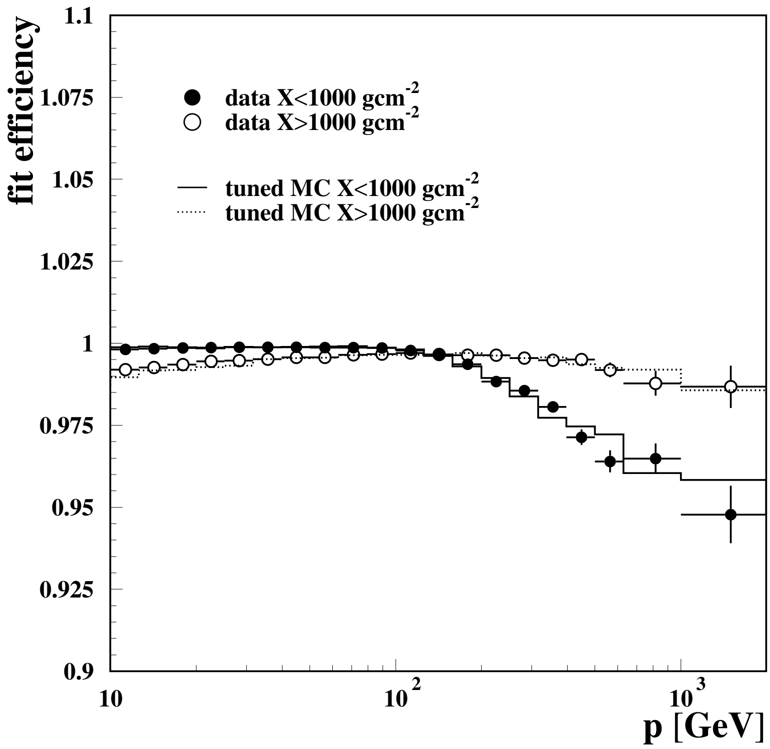

Fig. 4.7: *Double octant fit efficiency as a function of momentum for two different matter densities X traversed by the track.*

matter densities the total error is dominated by the track propagation errors $\mathbf{W}^i$, at high energies, these additional uncertainties lead to a bad fitting χ^2 on which bases the convergence of the fit is judged. The very small drop of the efficiency at low momentum and large X is not fully understood.

During the analysis, the observed data inefficiency is taken into account by applying the parameterized fit inefficiency to the simulation as indicated in figure 4.7.

Chapter 5

L3+C - DETECTOR PERFORMANCE

For the measurement of the muon flux, the precise knowledge of the detector performance is of major importance. Inefficiencies of the various subdetector components have to be corrected for and the effect of the finite momentum resolution of the detector on the measured momentum distribution needs to be taken into account as well as a possible systematic bias in the momentum scale due to the detector misalignment. Therefore, before the actual muon flux measurement could be done, detailed detector studies were needed, which are described in this chapter.

5.1 Scintillators

For the determination of the efficiency of the scintillator system, special trigger classes were forseen, which allow the recording of events fulfilling the usual P-chamber requirements, but without a signal from the scintillators (see table 3.1). The efficiency of the full scintillator system can then be calculated via

$$\varepsilon_{\mathrm{SCNT}} = \frac{N_{\mathrm{T}_0}}{N_{\not{\mathrm{T}}_0} + N_{\mathrm{T}_0}}\,, \qquad (5.1)$$

where N_{T_0} and $N_{\not{\mathrm{T}}_0}$ are the number of triggered events with and without a scintillator hit respectively.

This definition of the efficiency has the drawback of being composed of the intrinsic detector efficiency and the array geometry, as muons passing through gaps between the scintillator cassettes will of course not produce a signal. This drawback is overcome by a dedicated reconstruction algorithm [131], which is able to reconstruct muon tracks without making use of the scintillator t_0 information needed for calculating the drift times (3.3) in the standard procedure. This is possible for about 42% of the events, for which the muon track crosses at least one wire plane. In such cases the arrival time

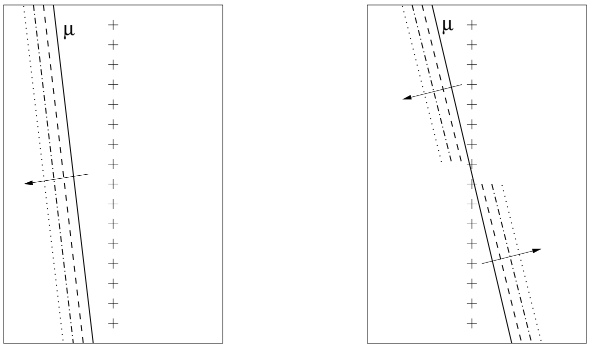

Fig. 5.1: *Illustration of the wire plane crossing principle. Crosses denote the sense wires, lines are parts of the track segment and the arrows indicate the shift of the reconstructed hit positions for $t'_0 > t_0$.*

can be deduced from the muon chamber signals themselves, as sketched in figure 5.1: For a segment without a wire plane crossing, different assumed arrival times t_0 just cause a parallel displacement of the segment, whereas in case of a wire plane crossing the actual arrival time of the muon can be adjusted by requiring a minimal offset between the segment parts left and right of the wire plane. Given the reconstructed momentum and direction of the muon inside the muon chambers, the track can then be extrapolated back to the scintillator planes. A measurement of the intrinsic scintillator efficiencies is then possible by selecting only events which passed a scintillator tile.
Almost six million events distributed over the two data taking years were selected for the efficiency analysis and re-reconstructed with this special algorithm. Figure 5.2 shows a map of the measured scintillator efficiency as a function of position on the scintillator array. The geometrical gaps in between the modules as well as the module structure itself (compare to figure 3.8) are clearly visible and inside the cassettes, the $25 \cdot 25$ cm^2 tiles depicted in figure 3.7 can be identified. The two photomultipliers attached on each module can be recognized as lengthy areas of low efficiency.
This large data set was used to measure the efficiency for each of the 202 cassettes c_i separately as a function of time t, the total array noise rate R_{tot} and photomultiplier quality cut Δt_{PM}:

$$\varepsilon_{\text{SCNT}} = f(c_i, t, R_{\text{tot}}, |\Delta t_{\text{PM}}|) \tag{5.2}$$

Photomultiplier quality cut

The distribution of the difference between the two time measurements of the same scintillator hit from the two read out photomultipliers attached to each module is shown in

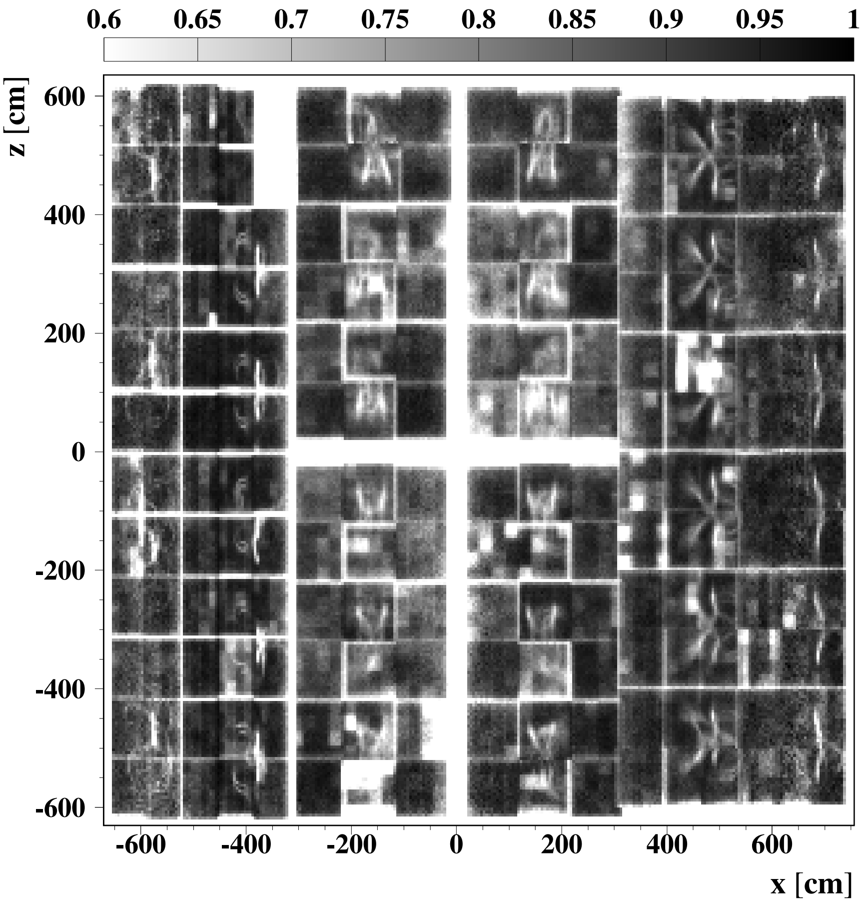

Fig. 5.2: *L3+C all year scintillator efficiency as a function of position on the scintillator array. A projection of the array on a horizontal plane above the magnet is shown. The gray-scale map indicates the efficiency value (efficiencies below 0.6 have been cut for better visibility and appear as white areas).*

figure 5.3(a). In the central region it is well described by a Gaussian distribution, from which a single photomultiplier time resolution of 1.8 ns can be derived. In addition, the distribution has long tails with a large Δt_{PM} indicating the presence of a large time slewing in at least one of the measurements. As it turns out, a cut on $|\Delta t_{\mathrm{PM}}|$ can be used to deselect muon tracks with a bad momentum resolution (see section 6.2). The corresponding event loss can be regarded as part of the scintillator inefficiency and was measured for each cassette separately. Figure 5.3(b) shows the behavior of the scintillator efficiency as a function of this cut averaged over all cassettes. As expected, the overall efficiency rises with a more loose constraint reaching about 0.97 asymptotically.

LEP induced noise

During quiet running conditions the full scintillator array registers a stable rate of scintillator hits of about 53 kHz, out of which most is due to thermal noise of the photomultipliers and low energy cosmic rays. When the LEP accelerator is running, and especially for unstable beam conditions, occurring for instance when filling or dumping the beam, the noise rate increases drastically, exceeding 180 kHz for about 20% of the collected data. Due to the small dead time of the L3CD units of around 0.3μs the event loss is expected to be about 0.2% for an array rate of 180 kHz. Figure 5.3(c) shows the measured rate dependence revealing a much larger influence of the noise rate on the efficiency. The discrepancy to the expected event loss indicates additional dead times or signal losses in the read out chain, which are not yet identified. An effective dead time τ_{eff} was introduced to describe the data via

$$\varepsilon = \varepsilon_0/(1 + \tau_{\text{eff}} R_{\text{tot}}) \ , \tag{5.3}$$

where R_{tot} denotes the array noise rate and ε_0 is the hypothetical efficiency at $R_{\text{tot}} = 0$. The fitted τ_{eff} values range from 0.27 to 0.56 μs depending on the data taking year and the scintillator module. This parameterization is indicated as a line in figure 5.3(c). A good description of the data is obtained up to a rate of $R_{\text{tot}} = 80$ kHz.
Due to the correlation between the module and array rate, a parameterization of the effective dead times as a function of the module rate fits the data equally well. The corresponding effective dead times range from 9.2 to 19 μs.

Time dependence

As any other detector material, plastic scintillators are subject to ageing processes. Firstly, there is the 'natural ageing' due to micro surface cracks and chemical reactions which deteriorate the scintillating capabilities of the tiles. Secondly, radiation damage has to be considered which may be caused by the synchrotron radiation impact from the LEP II high energy runs. Finally, cracks may occur in the light guiding fibers due to the mechanical stress of bending, worsening their transparency. Whereas natural ageing and radiation damage are expected to cause a continuous decreasing of the efficiency, these cracks can cause a sudden drop of the efficiency.
Most of the analyzed cassettes show a small decrease of the efficiency ranging from 0.5 to 3% in the time interval from the middle of 1999 to the end of 2000. A good description of the data is obtained by fitting a piecewise linear time dependence for each cassette inside four time periods (data taking 1999, winter shutdown 1999/2000,

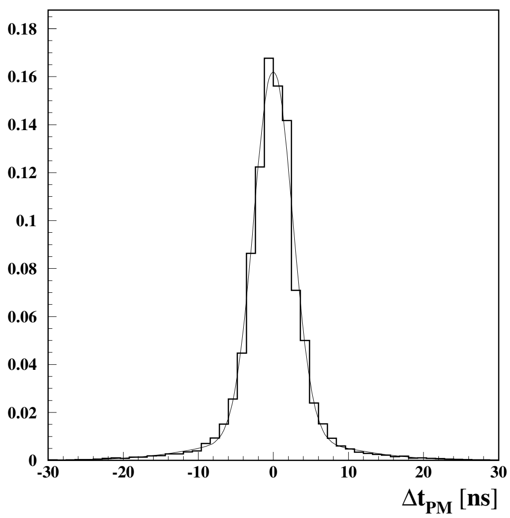

(a) *Distribution of the difference between the two photomultiplier time measurements. The line indicates a fit assuming a sum of two Gaussian distributions.*

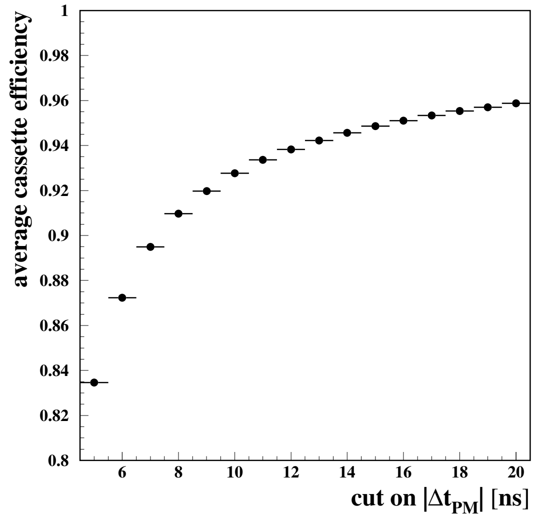

(b) *Relation of the average cassette efficiency on the cut on $|\Delta t_{PM}|$ (data from July 1999).*

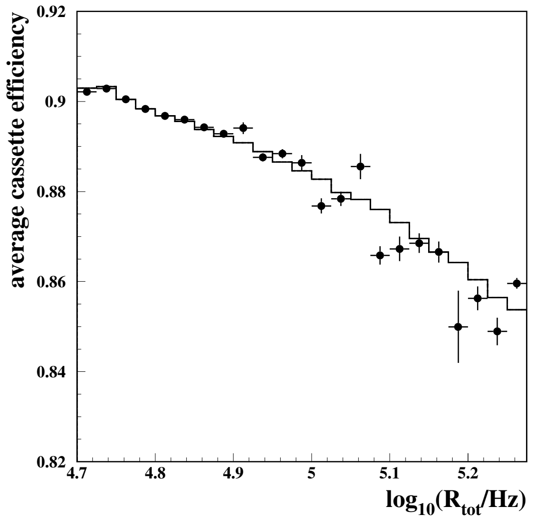

(c) *Noise dependence of the average scintillator efficiencies and its parameterization (October 1999 data, $|\Delta t_{PM}| \leq 8$ ns).*

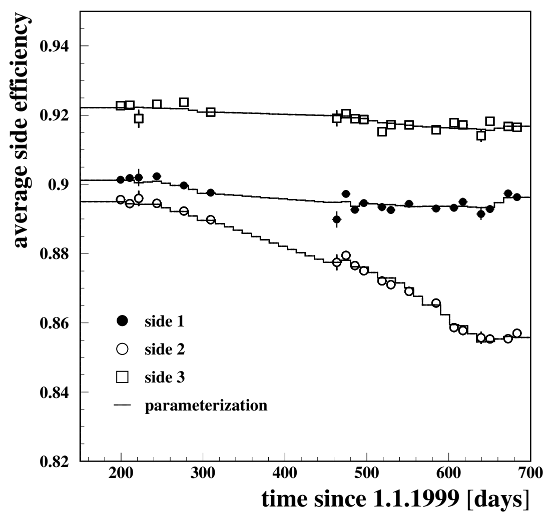

(d) *Time dependence of the average scintillator efficiencies and its parameterization ($|\Delta t_{PM}| \leq 8$ ns).*

Fig. 5.3: *Scintillator efficiency dependencies*

data taking 2000 and November 2000, when L3+C was running undisturbed after the final LEP shutdown). Five cassettes showed large efficiency drops of up to 30% within a few weeks which was accounted for by introducing a further subdivision of the fitting periods. Figure 5.3(d) shows the time dependence of scintillator cassette efficiencies averaged over the cassettes covering two muon chamber octants (the so called scintillator sides). Side 2 above octants 2 and 10 shows the strongest ageing, probably due to the fact that the used plastic tiles are 'second hand', whereas on side 1 and 3 new material was bought directly from the manufacturers. Also shown are the average parameterizations describing the data well over the full range.

Below, the systematic errors of the scintillator efficiency measurement are summarized. The systematics of the measurement method were studied varying the selection cuts applied to the analyzed events and a MC study, where the simulated efficiency was compared to the 'measured' one. A possible influence of the reconstruction algorithm was excluded in [133]. Finally, the root mean square of the difference between the measured and parameterized efficiencies is used as a measure of the accuracy of the time and noise dependence. In total a systematic error of 0.7% is estimated adding the individual contributions in quadrature.

error source	Δ_ε
cut variation	0.006
MC study	< 0.001
time dependence	0.002
reconstruction	< 0.002
noise dependence (R_{tot} <80 kHz)	0.002
total	0.007

5.2 Muon chambers

5.2.1 Efficiency

Three major sources of inefficiency of the muon chambers could be identified:

- **Dead cells:** Due to the mechanical tension acting on the muon chamber wires and ageing of the wire material, a sense or mesh wire may brake during the data taking. This usually short-circuits the high voltage supply of the cell and the complete cell needs to be disconnected until it may eventually be repaired during the winter shutdown of the LEP accelerator.

- **Bad cells:** These cells are not completely disconnected, but operated at lower voltages. As a consequence, their gain is lower and the electron drift path deviates from the standard cell map function resulting in a bad resolution [58] and a poor reconstruction efficiency [113].

- **TDC errors:** The TDCs used in L3+C to read out the muon chamber signals are known to lose data randomly as a consequence of a design failure [130]. One TDC reads out 32 neighboring signal wires, therefore a full segment may be lost.

The muon spectrum analysis uses tracks, which were reconstructed in six muon P-chamber layers and two times four Z-chamber layers. The corresponding track selection efficiency reads as

$$\varepsilon_{\text{track}} \approx \underbrace{\prod_{i=1}^{6} \varepsilon_i^{\text{P}}}_{\text{P}} \cdot \underbrace{\left(\sum_{i=4}^{8} B(i; 8; \langle \varepsilon^{\text{Z}} \rangle) \right)^2}_{\text{Z}} , \tag{5.4}$$

where B denotes the binomial distribution, $\langle \varepsilon^{\text{Z}} \rangle$ is the mean Z-chamber layer efficiency and ε_i^{P} stands for the efficiency of the ith P-chamber layer. As can be seen, especially the P-layer efficiency has a large impact on the track selection efficiency: If one cell along the muon track is disconnected, the track selection efficiency is zero.

The status of the muon chamber cells at the end of the data taking in 1999 and 2000 was studied the following way: A sub-track reconstructed inside one octant is extrapolated to the facing octant. At the intersections with the muon chamber planes, the absence of recorded hit positions indicates an inefficient ('bad') or disconnected ('dead') detector region. Using the data of one day in 1999, 107 out of the 1456 P-chamber

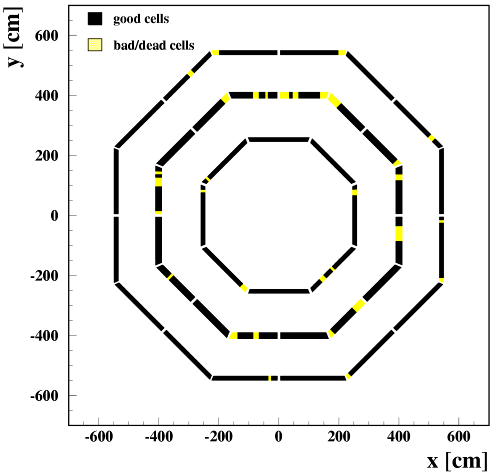

(a) *P-chamber master side*

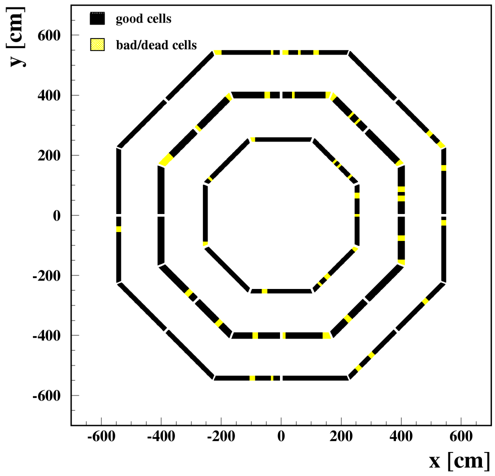

(b) *P-chamber slave side*

Fig. 5.4: *P-chamber cell status at the end of data taking.*

cells, and 570 out of the 11424 Z-chamber cells were found with an efficiency lower than 80%. The corresponding number of bad cells at the end of the year 2000 is 57 (P) and 731 (Z). A good correlation with the high voltage status database maintained by L3 was found, but the study revealed 25 P-cells and 197 Z-cells with low or zero efficiency not recorded there. Figure 5.4 displays the location of the bad P-cells at the end of data taking*. It is clear, that the numerous bad and dead detector areas considerably diminish the track selection efficiency given in equation (5.4). The corresponding event loss depends non-trivially on where and in which direction the muon enters the detector volume. Moreover, a momentum and charge dependence is expected, due to the bending of the muon track within the magnetic field. To be able to calculate the track selection efficiency as a function of zenith angle and muon momentum, hits from bad and dead cells are not used in the reconstruction of the muon tracks in data and MC. The measured cell status at the end of 1999 and 2000 was used for this purpose. This has the advantage, that only two periods of constant muon chamber acceptance are defined. On the other hand, as the detector status degrades with time in one data taking year, this simplification means a loss of data, since cells, which may have been working at the start of data taking are not used, if they turned out to be dead at the

*As not enough atmospheric muons pass the horizontal side octants, the status from the L3 database is used for these octants without a cross-check from the L3+C data.

octants	efficiency [%]	
	1999	2000
1 + 5	92.3	92.7
2 + 6	92.9	92.9
3 + 7	88.3	89.8
9 + 13	94.2	94.6
10+ 14	93.0	92.4
11+ 15	90.7	91.1

Tab. 5.1: *Estimated selection efficiency due to the TDC inefficiency for diagonal octant pairs.*

end of the year. The corresponding loss of selected high quality events amounts to only 3%, which is why the constant acceptance scheme was favored over a more complicated subdivision of data and MC in many time periods.
The average efficiency of the remaining cells at nominal high voltage was measured to be 98.7% in case of the P-chambers, and 91.7% for the Z-chambers. These residual signal losses can be explained by the TDC inefficiency mentioned above and are expected to vary from cell to cell and with time [130]. In contrast to the disconnected cells, they occur at random and are uncorrelated between the different drift layers. The corresponding track selection efficiencies according to equation (5.4) are estimated based on the individual chamber efficiencies and are listed in table 5.1 for diagonally facing octants and the two data taking years. The correction for this inefficiency will be discussed in section 6.3.1.

5.2.2 Alignment

The precision of the alignment of the muon chamber layers with respect to each other is one of the major limitations for this measurement. Its influence on the momentum determination can be illustrated recalling the sagitta measurement s inside a single octant sketched in figure 4.3. In case of non zero alignment shifts δ_{1-3} of the three drift chamber layers, the equation (4.5) for the calculation of sagitta inside one octant reads as

$$s = s_2 + \delta_2 - \frac{s_1 + \delta_1 + s_3 + \delta_3}{2} \equiv s + \delta_s \ , \tag{5.5}$$

where δ_s is the effective sagitta shift. It leads to a systematically biased reconstructed muon momentum. The momentum shift is different for positive and negative momenta,

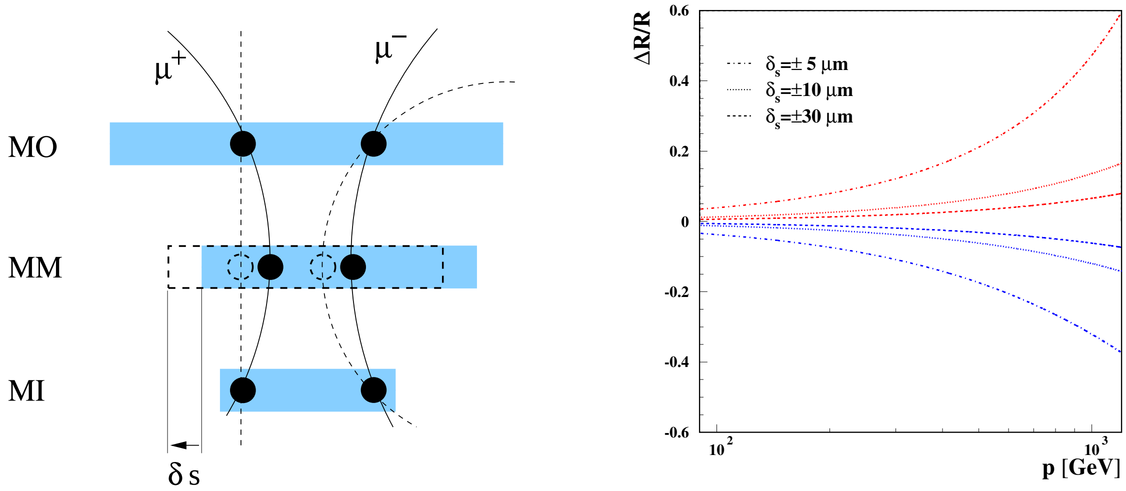

(a) *The reconstructed muon trajectories (dashed) in case of an unknown alignment shift δ_s in comparison to the true muon paths (solid).*

(b) *Relative change of the measured charge ratio measured inside one octant for three different misalignments.*

Fig. 5.5: *Illustration of the effect of a misalignment of the middle P-chamber on the reconstructed momentum and the charge ratio.*

as illustrated in figure 5.5(a) for a shift of the middle P-chamber layer.
For a power law flux of positive and negative muons

$$\Phi(p) = (c_+ \cdot p^{-3} + c_- \cdot p^{-3}) , \qquad (5.6)$$

it is shown in [132], that a misalignment δ_s leads to a measured flux

$$\Phi(p) = c_+ \left(p^{-3} + \frac{\delta_s}{a}\, p^{-2} \right) + c_- \left(p^{-3} - \frac{\delta_s}{a}\, p^{-2} \right) \qquad (5.7)$$

and charge ratio of

$$R(p) = \frac{c_+}{c_-} \cdot \frac{p^{-3} + \frac{\delta_s}{a}\, p^{-2}}{p^{-3} - \frac{\delta_s}{a}\, p^{-2}}. \qquad (5.8)$$

Here a denotes the detector constant needed to convert the sagitta to a momentum. It is 0.157 m GeV inside one octant and 2.21 m GeV for the full detector (see equations (4.3) and (4.4)). In case the amount of positive and negative muons is almost the same ($c_+ \approx c_-$), a misalignment has only little effect on the total muon flux, as the correction terms in equation (5.7) cancel out. The charge ratio however is very sensitive to the

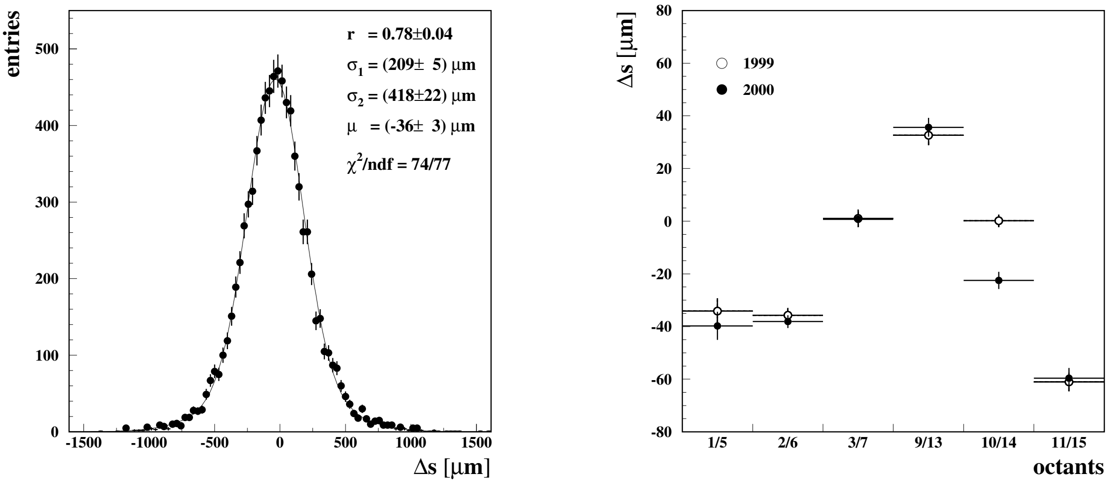

(a) *Sagitta difference Δs between octant 2 and 6 in 1999 at a momentum of 100 GeV.*

(b) *Sagitta differences Δs between diagonally facing octants in 1999 and 2000.*

Fig. 5.6: *Estimation of the internal octant misalignment.*

alignment. Figure 5.5(b) displays the relative difference between the true and measured charge ratio according to equation (5.8) for the single octant momentum fit and three rather modest misalignments.
After these considerations it is clear that the detector alignment plays a significant role in the overall systematics of this analysis. As the muon flux does not exactly follow equation (5.6), the actual systematic effects will be discussed in section 6.4.1. In the following the determination of the alignment parameters and their uncertainties will be described.

Internal octant alignment

As mentioned in section 3.2.1, each octant is equipped with an optical alignment system. The system was designed to align the chambers such that the effective sagitta error stays below 30 μm [6]. This can be cross-checked by measuring the mean difference Δs of the sagitta measurements of the same muon in two octants:

$$\Delta s = \left\langle (s_1 + \delta_s^1) - (s_2 + \Delta_s^{\mathrm{loss}} + \delta_s^2) \right\rangle = \delta_s^1 - \delta_s^2 \; , \tag{5.9}$$

where the index 1/2 denotes the upper and lower octant respectively. The lower sagitta measurement s_2 is corrected for the average energy loss in the inner detectors according to the GEANE prediction Δ_s^{loss}. An example for this measurement is shown in figure 5.6(a), where the sagitta difference distribution for the octants 2 and 6 in 1999 is shown. It was fitted with the sum of two Gaussian distributions yielding $\Delta s = -36 \pm 3\mu m$. The fitted sagitta differences for all diagonal octant pairs are displayed in figure 5.6. They are within ±60 µm as expected from the L3 design value.

Relative octant alignment

The L3 muon chamber system was designed to measure the momentum of muons originating from the LEP accelerator. Above 3 GeV, these muons are confined in one octant, therefore no relative alignment of the octants is needed in this case. This is of course different for the double octant fit explained in the previous chapter, where the track of an atmospheric muon is fitted using the reconstructed hit positions from two octants.
Due to the lack of external information on the relative octant alignment, the parameters were determined from the data itself. For this purpose, the coordinates x, z and the directions λ, ϕ of the reconstructed single octant tracks were compared at their intersection with the vertex plane as sketched in figure 5.7. To match both the coordinates and directions, one octant is shifted and rotated such that the intercepts of the tracks agree with each other on average. This is achieved by minimizing

$$\chi^2_{ij} = \sum_{\text{events}} \left(\sum_{\xi = x,z,\lambda,\phi} \frac{[\xi_i - \xi'_j(\mathbf{t_{ij}}, \mathbf{E_{ij}})]^2}{2\sigma^2_\xi} \right) \tag{5.10}$$

for each combination of octants i and j from the upper and lower hemisphere. Here $\mathbf{t}$ denotes the translation vector

$$\mathbf{t} = (\Delta x, \Delta y, \Delta z) \tag{5.11}$$

and $\mathbf{E}$ is the Euler rotation matrix.

$$\mathbf{E} = \mathbf{E}(\alpha, \beta, \gamma) \tag{5.12}$$

depending on three rotation angles α (rotation around the original y-axis), β (rotation around the new z-axis) and γ (rotation around the new y-axis). As it turned out, β is close to zero, which is why α and γ are not independent and γ needs to be forced to zero to obtain stable fits. Due to the multiple scattering in the L3 inner detectors, the errors σ_ξ depend on the muon momentum and the amount of matter traversed by the track.

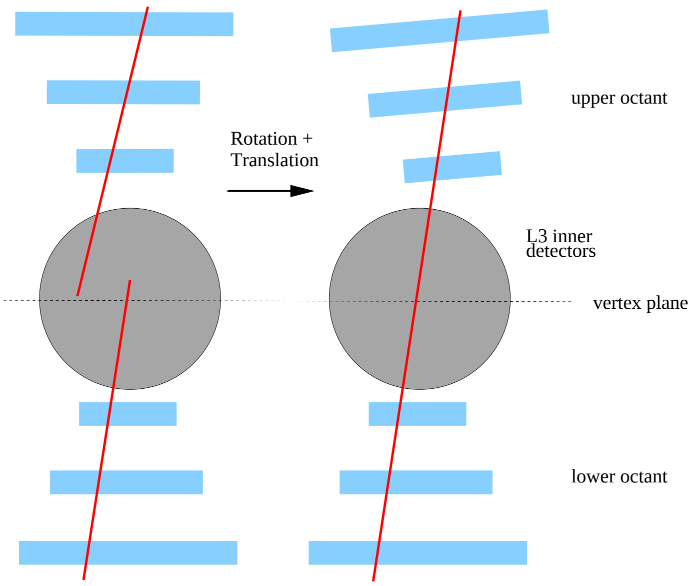

Fig. 5.7: *Illustration of the determination of the relative octant alignment from the single octant muon tracks (denoted by straight lines).*

For each data run, a full set of alignment parameters was determined using the data recorded within ±12 hours around the data taking time. The obtained translation constants range from -6 to 6 mm and the measured rotation angles are within ±1 mrad. As a consequence of the careful design of the mechanical properties of the octant stands supporting the chambers, the alignment parameters were found to vary only little within the two data taking years. The observed changes are below 1 mm for the translation constants and smaller than 0.2 mrad in case of the rotation angles.
The determination of the alignment parameters was repeated for different detector parts and at different momenta. The latter may reveal systematic errors due to the inhomogeneous magnetic field and energy loss, whereas the influence of the internal octant alignment due to a torsion or shear of the chamber layers could be different for different detector parts.
Figure 5.8(a) shows a typical example of this study: Only a small variation of the translation constant with the momentum is found, but a large systematic effect is observed when selecting muons at different vertex plane intercept positions. The investigation of all octant combinations leads to a systematic uncertainty on the translation parameters of $\sigma_{x,y,z} \leq 1$ mm and $\sigma_{\alpha,\beta} \leq 0.1$ mrad for the rotation angles. To obtain the corresponding effective sagitta uncertainty δ_s the simulated detector was accordingly misaligned in a MC study, including also an internal shift of the middle P-chambers

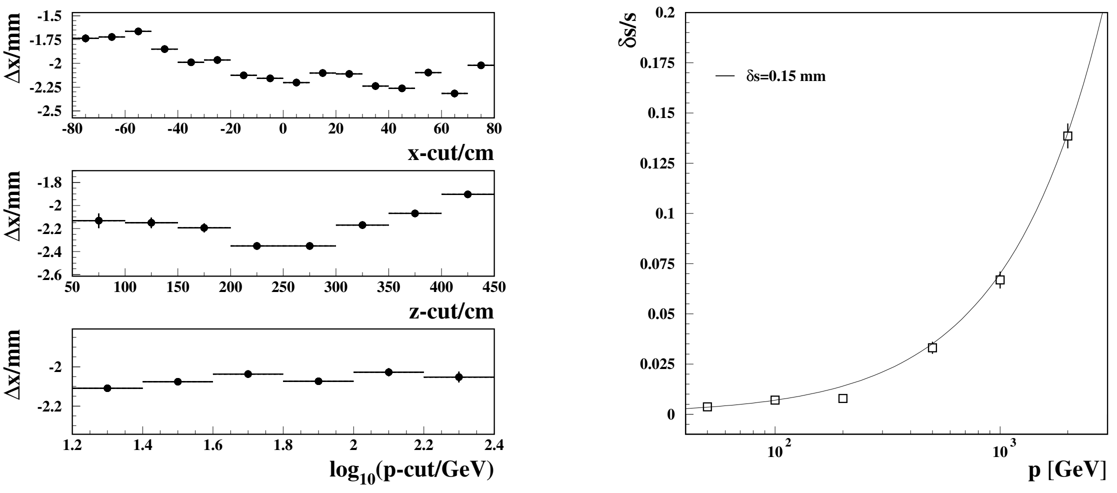

(a) *Variation of the translation constant Δx for different detector regions and momenta (octants 10 and 14).*

(b) *MC evaluation of the effective double octant sagitta uncertainty.*

Fig. 5.8: *Systematic error on the relative double octant alignment.*

of 30 µm. The simulated sagitta bias is shown in figure 5.8. It is dominated by the uncertainty in β and is well described by $\delta_s = 0.15\,\text{mm}$. Converting the single and double octant sagitta uncertainty to an inverse momentum uncertainty $\delta(1/p)$, which is independent of the lever arm used in the fit, the single octant uncertainty reads as

$$\delta(1/p)^{\text{so}} = 0.19\ \text{TeV}^{-1} \tag{5.13}$$

and for the double octant fit a value of

$$\delta(1/p)^{\text{do}} = 0.070\ \text{TeV}^{-1} \tag{5.14}$$

is estimated.

5.2.3 Momentum resolution

The L3+C detector does not directly measure the momentum of a muon, but the sagitta of a muon track, which is proportional to the charged inverse momentum as can be seen in equation (4.2). Hence the variable q/p and not p itself should follow an approximately Gaussian behavior and the momentum resolution due to the sagitta uncertainty is rising quadratically with the momentum:

$$\sigma_p^{\text{sag}} = \sigma(q/p) \cdot p^2 \ . \tag{5.15}$$

Another contribution to the momentum resolution is due to the multiple scattering in the detector material, which deviates the muon track form an ideal helix in the magnetic field. For homogeneously distributed material and a muon trajectory perpendicular to the magnetic field it is given by

$$\sigma_p^{\mathrm{ms}} = c_{\mathrm{ms}} \cdot p \, , \tag{5.16}$$

with

$$c_{\mathrm{ms}} \approx 0.053 \, \frac{1}{B/\mathrm{T}\; L/\mathrm{m}} \sqrt{\frac{L}{X_0}} \, , \tag{5.17}$$

where B denotes the magnetic field strength, L is the track length and X_0 is the radiation length of the detector material. The multiple scattering is an important effect muon tracks with a momentum below the critical value $p_{\mathrm{crit}} = c_{\mathrm{ms}}/\sigma(q/p)$. For the single octant fit $p_{\mathrm{crit}} \approx 10$ GeV. Due to the large amount of material in between the muon chamber octants, the multiple scattering is important for the double octant fit up to about 1 TeV.

At a given momentum interval $[p_i, p_i+\Delta]$, the number of measured events n_i will not be exactly the true number of events N_i, because due to the finite momentum resolution a certain fraction of events will 'migrate' to neighboring momentum intervals $[p_j, p_j+\Delta]$ with a probability $P_{ij}(\sigma_{p_i})$. On the other hand, events with true momentum p_j may be measured with momentum p_i, such that the total number of observed events is

$$n_i = N_i - \sum_j N_i \cdot P_{ij}(\sigma_{p_i}) + \sum_{j,j\neq i} N_j \cdot P_{ji}(\sigma_{p_j}) \, . \tag{5.18}$$

Due to the expected steepness of the atmospheric muon momentum spectrum, the number of events with $j < i$ is much larger than N_i, therefore more events migrate from lower momenta to higher ones and the observed muon spectrum flattens as σ_p increases.

This is illustrated in figure 5.9, where a MC study of the effect of the momentum resolution on the measured spectrum is shown. Anticipating the results of this section, simulated muons from the `l3cgen` generator (see section 4.3) were smeared according to the measured detector resolutions for various cases. As can be seen, the ratios of n_i/N_i are close to one at low momenta, where the relative momentum resolution is still small. However, at high energies the ratios range from 1.3 to 6.7 depending on the measuring technique used.

After these considerations, it should be clear, that the momentum resolution is one of the key detector parameters needed to measure the spectrum. Firstly, a good

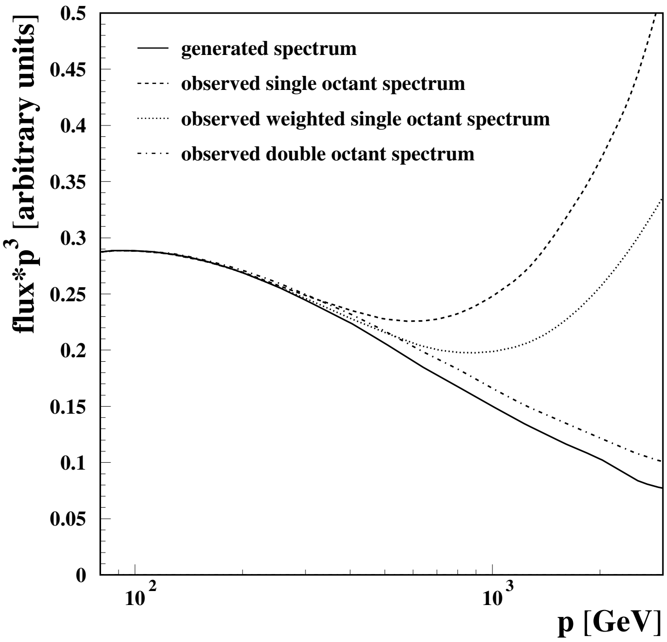

Fig. 5.9: *MC simulation of the resolution effect on the observed muon spectrum.*

momentum resolution is needed to keep the differences between the measured and true muon spectrum small, and secondly it must be well known, in order to be able to correct the residual differences.

In the following, the determination of the detector resolution will be described. The resolution of the single octant fit, which can be inferred from the data itself, will be used to tune the the detector simulation. Subsequently, the double octant resolution will be determined from the simulation, as it is not directly accessible from the data. All results of this section apply only to muon tracks of the quality selection described in chapter 6.

Single octant momentum resolution

For the evaluation of the single octant momentum resolution, the difference between the two curvature measurements of the same muon in two octants is investigated:

$$\Delta_{\mathrm{ul}} = [q/p]_{\mathrm{u}} - [q/p]_{\mathrm{l}} - \delta_{\mathrm{eloss}} \ , \tag{5.19}$$

where p_u and p_l denote the momentum measurements in the upper and lower octant respectively and δ_eloss denotes the `GEANE` correction for the energy loss of the muon from the upper to the lower detector hemisphere. Thus the expected variance of Δ_ul is given by

$$\mathrm{V}[\Delta_\mathrm{ul}] = 2 \cdot \mathrm{V}[q/p] + \mathrm{V}[\delta_\mathrm{eloss}] \tag{5.20}$$

assuming equal curvature resolutions in the upper and lower octant. Separating the variance V_ms due to the multiple scattering inside one octant from the detector related resolution σ_det, equation (5.20) can be rewritten as

$$\mathrm{V}[\Delta_\mathrm{ul}] = 2 \cdot \sigma^2_\mathrm{det} + 2 \cdot \mathrm{V}_\mathrm{ms} + \mathrm{V}[\delta_\mathrm{eloss}] \,. \tag{5.21}$$

Both V_ms and $\mathrm{V}[\delta_\mathrm{eloss}]$ were evaluated using the L3+C detector simulation leading to

$$\mathrm{V}_\mathrm{ms} = \left(0.011 \cdot p^{-1}\right)^2 \tag{5.22}$$

and

$$\mathrm{V}[\delta_\mathrm{eloss}] = \left(0.015 \cdot p^{-1}\right)^2 \tag{5.23}$$

The following factors could be identified to contribute to the detector resolution:

(a) Chamber resolution:

Given the equations (4.3) and (4.5) for the calculation of the sagitta of the muon track from the segment positions, the corresponding resolution reads as

$$\begin{aligned} \sigma^2_\mathrm{cham} \cdot a^2 &= \sigma^2_{s2} + \frac{\sigma^2_{s1} + \sigma^2_{s3}}{4} \\ &= \sigma^2_\mathrm{swr} \cdot \left(\frac{1}{N_2} + \frac{1}{4 \cdot N_1} + \frac{1}{4 \cdot N_3} \right) \\ &\equiv \sigma^2_\mathrm{swr} \cdot f_\mathrm{hit} \,, \end{aligned} \tag{5.24}$$

where σ^2_swr is the positional resolution of a single sense wire, N_i denotes the number of used hits in chamber i and $a = 0.157$ m GeV is the constant relating the sagitta and the inverse momentum. In the last line the hit resolution function f_hit is introduced. Its nominal value is $f_\mathrm{nom} = 1/24 + 1/(4 \cdot 16) + 1/(4 \cdot 16) = 0.0729$ in case each segment uses exactly all hits of one cell in each of the three chambers. Due to the disconnected P-cells, on average a slightly worse value of 0.0788 is observed. The overall distributions of the ratio $f_\mathrm{hit}/f_\mathrm{nom}$ for data and MC are shown in figure 5.10(a).

The single wire resolution is estimated from the difference of the hit positions at (x, y) to the segment circle fit c:

$$r = \frac{N}{N - N_\mathrm{df}} \left(x - c(y)\right) \,, \tag{5.25}$$

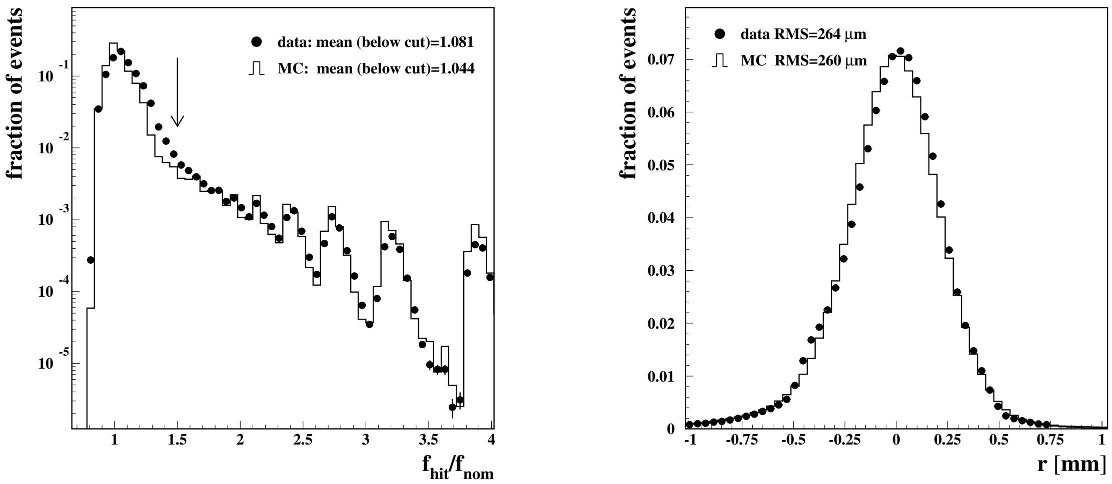

(a) *Ratio of the hit resolution function to its nominal value for data and MC. The arrow indicates the cut applied in the data selection (see section 6.2).*

(b) *Segment fit hit residual distribution for data and MC.*

Fig. 5.10: *Detector parameters determining the chamber resolution.*

where N denotes the number of hits used in the fit and $N_{\mathrm{df}} = 3$ is the number of degrees of freedom of the fit. The overall residual distribution is shown in figure 5.10(b) for data and MC. The latter was simulated using a parameterization of the single wire resolution as a function of distance and angle with respect to sense wire plane [117]. For this analysis, also the tails of the distribution were simulated leading to a good overall agreement between data and MC. Using the observed RMS of 264 μm, the contribution of the chamber resolution to the single octant momentum resolution is

$$\sigma_{\mathrm{cham}} = 0.472\ \mathrm{TeV}^{-1}\,, \tag{5.26}$$

which is reproduced by the MC within 3%.

(b) Scintillator time resolution:

The resolution of the timing provided by the scintillators enters the measurement of the track position via equation (3.3). A deviation Δt from the true arrival time t_0 leads to a correlated shift of $\Delta x = \, ^{+}_{(-)} v_{\mathrm{drift}}\, \Delta t$ for all sense wire hits right (left) of the sense plane. As mentioned above, the intrinsic time resolution of the scintillators amounts to 1.8 ns. The related average effect on the curvature resolution was extracted from

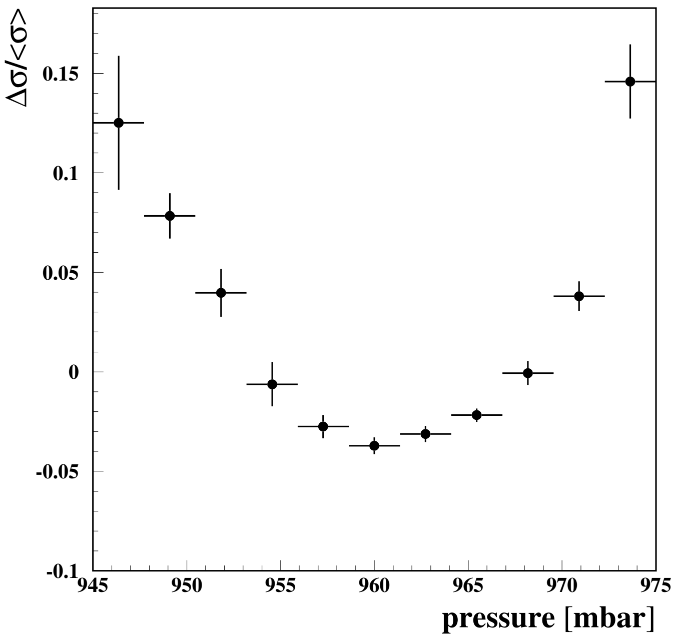

Fig. 5.11: *Relative change of the curvature resolution with respect to the atmospheric pressure.*

the data in [117] and amounts to

$$\sigma_{\mathrm{t0}} = (0.57 \pm 0.06)\ \mathrm{TeV}^{-1}\ . \tag{5.27}$$

The corresponding number derived from the detector simulation is (0.61 ± 0.01) TeV^{-1} and agrees well with the measured value within its statistical error.

(c) Calibration uncertainties:

In addition to the known single wire and scintillator timing resolution, several calibration uncertainties may contribute to the momentum resolution: The uncertainty of the alignment of the chambers and sense wires is expected to contribute $\sigma_{\mathrm{al}} \leq 0.15$ TeV^{-1} to the total resolution [58]. According to [41], the point to point uncertainty of the magnetic field is ≤ 0.002 T. Using the relation between the P-chamber drift velocity and the magnetic field given in [115] this corresponds to $\sigma_{\mathrm{B}} \leq 0.07$ TeV^{-1}. The uncertainty of the drift velocity calibration itself is estimated by comparing the L3+C value [140] to the one obtained by L3 with another method, which leads to $\Delta v \leq 0.1\ \mu\mathrm{ms}^{-1}$ or a resolution uncertainty of $\sigma_{\mathrm{v}} \leq 0.23$ TeV^{-1}.

The gas pressure inside the muon chambers is assumed to be constant in the reconstruc-

tion, whereas it varies more than 1% due to the change of the atmospheric pressure over the year. As can be seen in figure 5.11, this significantly worsens the resolution, because the change of drift properties of the gas is not accounted for. The comparison of the resolution at the minimum to the overall resolution leads to an additional error of $\sigma_{\rm gas} = 0.24$ TeV^{-1}.
Finally, the time offsets of muon chamber signals due to the time of propagation along the read out cables are determined within 0.5 ns [108] corresponding to $\sigma_{\rm t0cal} \leq 0.19$ TeV^{-1}.
Adding all these uncertainties in quadrature, the contribution of the known calibration uncertainties to the curvature resolution can be estimated to be

$$\sigma_{\rm sys} \leq 0.42 \text{ TeV}^{-1} . \tag{5.28}$$

The measured curvature difference can be well described by the sum of two Gaussian distributions G:

$$f(x) = A\,[r\,G(x,\mu,\sigma_1) + (1-r)\,G(x,\mu,\sigma_2)] , \tag{5.29}$$

where A denotes the normalization constant, σ_1 and σ_2 denote the width of the two Gaussian distributions, r is the fraction of events participating in the first Gaussian distribution and $x = (q/p_1 - q/p_2)/\sqrt{2}$. The factor $\sqrt{2}$ is applied to extract the single octant contribution $\sigma_{\rm det}$ from equation (5.21).
An example of the measured curvature difference is shown in figure 5.12 for energies of 100 GeV. The momentum dependence of the parameters A, σ_1 and σ_2 is displayed on the left side of figure 5.13. As can be seen, the default MC does not reproduce the observed data distribution. This could be expected, because no calibration uncertainties affect the simulated muon chambers. The existence of the second Gaussian contribution is however also predicted by the simulation, therefore it seems plausible, that it is caused by poorly reconstructed tracks.
At high energies, where the multiple scattering and energy loss are negligible, a single octant resolution of

$$\sigma_{\rm det,1} = (0.916 \pm 0.007)\,\text{TeV}^{-1} \tag{5.30}$$

is measured for 69% of the events and

$$\sigma_{\rm det,2} = (1.80 \pm 0.02)\,\text{TeV}^{-1} \tag{5.31}$$

for the remaining 31% of the events.
Comparing $\sigma_{\rm det,1}$ to the maximum expected total error of

$$\begin{aligned} \sigma_{\rm exp} &= \sigma_{\rm cham} \oplus \sigma_{\rm t0} \oplus \sigma_{\rm al} \oplus \sigma_{\rm B} \oplus \sigma_{\rm v} \oplus \sigma_{\rm t0cal} \oplus \sigma_{\rm gas} \\ &= 0.85 \text{ TeV}^{-1} , \end{aligned} \tag{5.32}$$

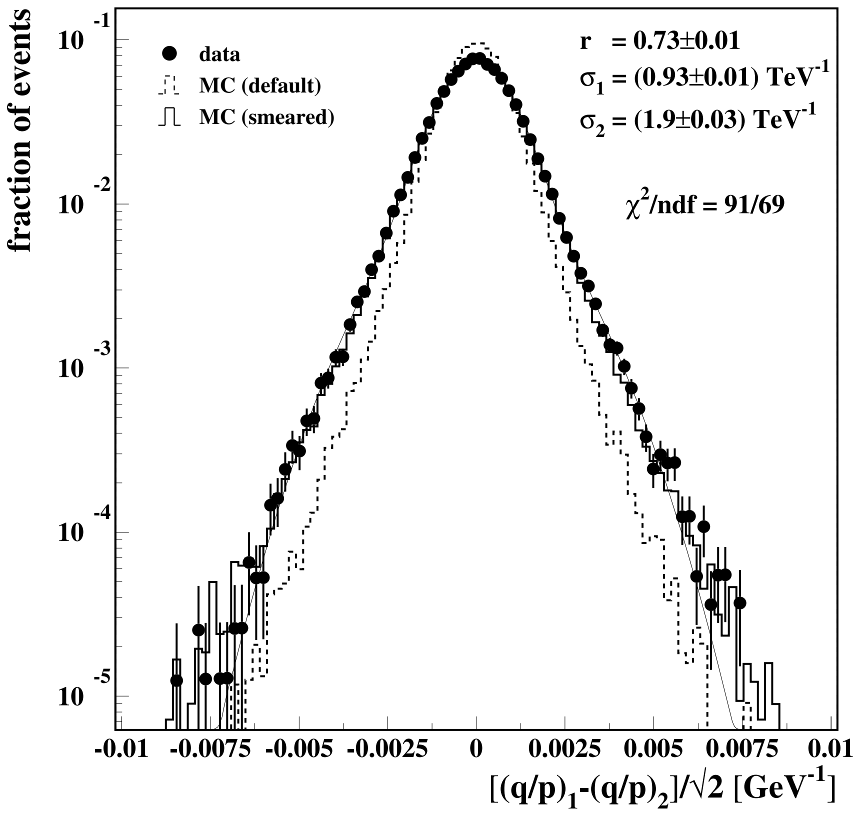

Fig. 5.12: *Example of the curvature difference at 100 GeV. The line denotes a fit with two Gaussian distributions according to equation 5.29.*

an additional unknown systematic contribution of 0.34 TeV^{-1} can be stated.
In order to adjust the MC to the data, the reconstructed simulated momenta are smeared via

$$\left(\frac{q}{p}\right)_{\mathrm{smear}} = \left(\frac{q}{p}\right)_{\mathrm{gen}} - \left[\left(\frac{q}{p}\right)_{\mathrm{gen}} - \left(\frac{q}{p}\right)_{\mathrm{rec}}\right] \cdot c_s \ , \tag{5.33}$$

where c_s denotes the smearing factor

$$c_s^2 = \frac{(\sigma_{\mathrm{det},1}^{\mathrm{data}})^2 + \mathrm{V}[\delta_{\mathrm{eloss}}] + \mathrm{V}_{\mathrm{ms}}}{(\sigma_{\mathrm{det},1}^{\mathrm{MC}})^2 + \mathrm{V}[\delta_{\mathrm{eloss}}] + \mathrm{V}_{\mathrm{ms}}} \ . \tag{5.34}$$

$\mathrm{V}[\delta_{\mathrm{eloss}}]$ needs to be set to zero for the upper octant. At high energies $c_s = 1.251$. As can be seen in figure 5.12, after this procedure, the data distribution is nicely reproduced by the MC.

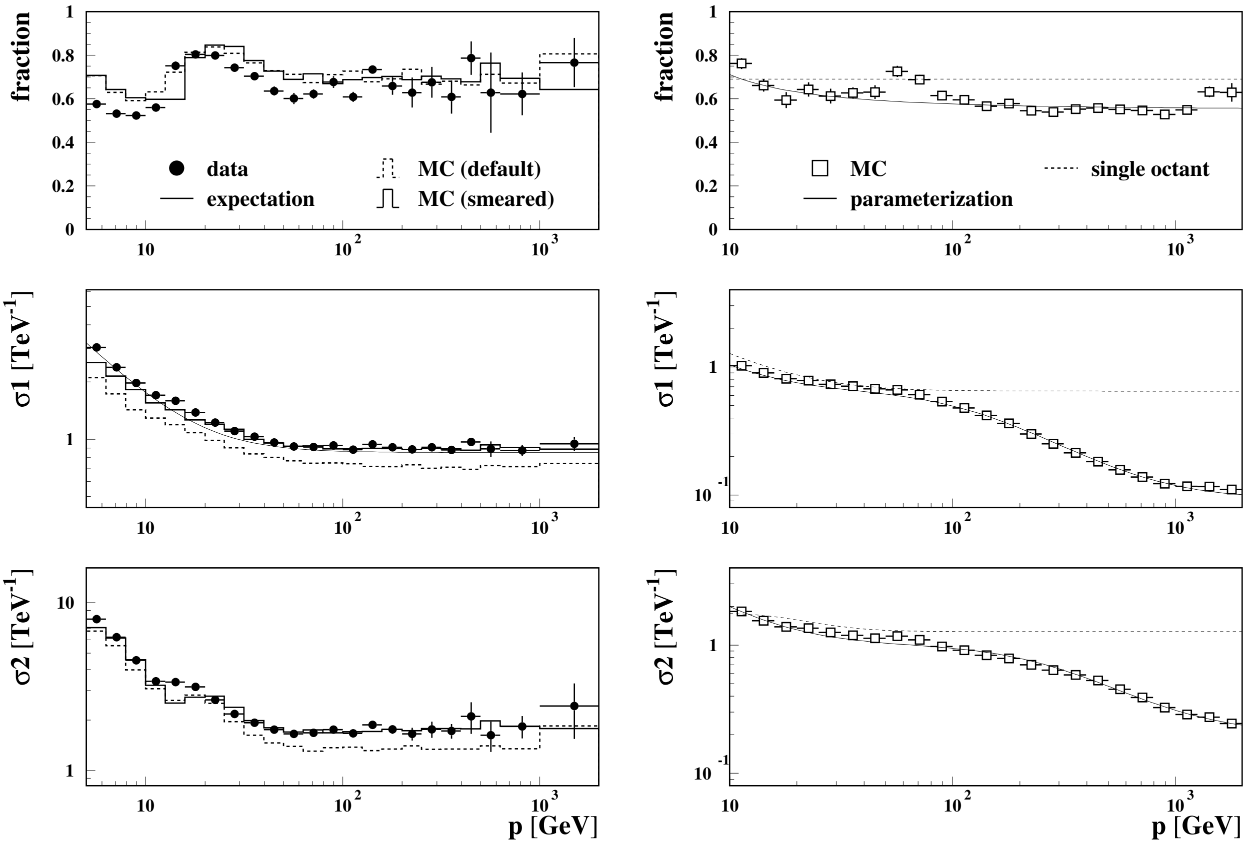

(a) *Single octant fit.*

(b) *Double octant fit.*

Fig. 5.13: *Parameters of the fit of the momentum resolution with a sum of two Gaussian distributions as a function of momentum. For comparison, a parameterization of the single octant parameters (dashed line) is superimposed to the double octant fit histograms on the right panel.*

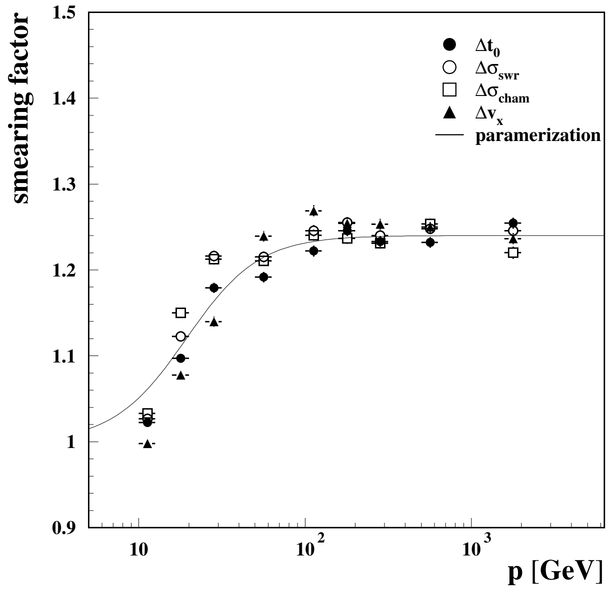

Fig. 5.14: *MC double octant smearing factors for different calibration uncertainties.*

Double octant momentum resolution

The double octant resolution can not be inferred directly from the data, therefore it is determined with the detector MC. As seen in the previous section, the simulation fails to predict the absolute curvature resolution, but can be adjusted easily with a smearing factor, since the overall shape of the MC resolution agrees well with the data. A priori it is not clear, whether the calibration uncertainties influence the double octant fit in the same way as in the single octant case. For instance, the single octant fit has zero degrees of freedom, whereas the double octant fit has up to five, which may average out some of the position measurement errors.
This was checked by introducing the following additional errors to the simulation:

- a timing offset between the chambers and the scintillators of 2.8 ns,
- an enlarged single wire resolution of $\sigma'_{\mathrm{swr}} = 1.23 \cdot \sigma_{\mathrm{swr}}$,
- a chamber-wise positional error of 50 μm and
- a drift time bias of $\Delta v_x = 0.2\,\mu\mathrm{ms}^{-1}$.

The values are chosen such that the resulting single octant resolution is close to the one observed in the data. The obtained smearing factors are shown in figure 5.14 along

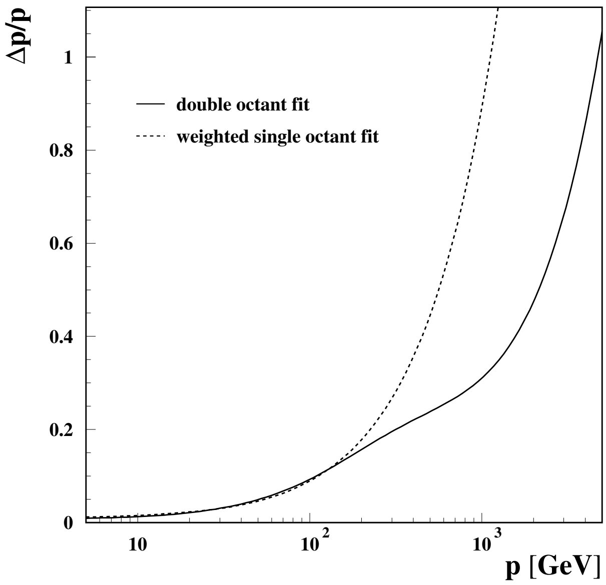

Fig. 5.15: *Relative momentum resolution as a function of momentum for the two fitting methods.*

with a parameterization. Due to the differences between these factors and the residuals with respect to the parameterization a systematic error of 8% on the double octant inverse momentum resolution is assumed.
As in the single octant case, the distributions are fitted according to equation (5.29) and the results are presented in figure 5.13(b). For comparison, the resolution of the weighted average of two octant measurements

$$\sigma_{\mathrm{w}}^{\mathrm{so}} = (1/V_u + 1/V_l)^{-\frac{1}{2}} \tag{5.35}$$

is also shown. As can be seen, a significant improvement of the momentum resolution is achieved at high momenta. At low momenta, the resolutions approach each other, because the measurements from the lower octant do not contribute to the fit in both cases due to the uncertainty of the energy loss and multiple scattering in the L3 inner detector and the support tube. Defining the effective resolution as

$$\sigma_{\mathrm{eff}} = (r \cdot \sigma_1^2 + (1-r) \cdot \sigma_2^2)^{\frac{1}{2}} \ , \tag{5.36}$$

the relative momentum resolution $\Delta p/p = \sigma_{\mathrm{eff}} \cdot p$ is shown in figure 5.15.

The performance of a spectrometer is often quantified by its 'maximum detectable momentum' MDM, i. e. the momentum, where the relative momentum resolution is 100%. The L3+C MDM is 1.1 TeV for the weighted single octant fit and (4.7±0.4) TeV for the double octant fit.

5.3 Trigger and data acquisition system

5.3.1 Dead time

For the measurement of event rates, a precise knowledge of the time the L3+C readout system is busy processing data without being capable to accept events is necessary. This time is usually referred to as dead time t_{dead}. The observed event rate R_{obs} within a time span t is related to the true event rate R_{true} by

$$R_{\text{true}} = R_{\text{obs}} \frac{t}{t - t_{dead}} = R_{\text{obs}} \frac{t}{\tau} \tag{5.37}$$

where τ denotes the live-time $\tau = t - t_{dead}$.

The L3+C readout electronics provides two ways of measuring the live-time: First a 10 MHz counter is started at the start of each run. Whenever the trigger is disabled, because the event or TDC buffers are full, the 10 MHz counter is also stopped. Thus the live-time of a run can be inferred by the number of counts at the end of the run. Secondly, the CTT receives a trigger signal from the GPSTIM 1Hz clock, which causes a trigger no matter what signals were present in the muon chambers or scintillators. If the CTT is not disabled because data of preceeding events are processed, this (usually empty) event is recorded, and the number of 1Hz triggers on tape at the end of the run gives the live-time of the run in seconds. Figure 5.16 shows the live-time measured with the 10 MHz counter for all the runs of the 1999 and 2000 data taking period, which were used in this analysis. A slightly better performance in the year 2000 is observed. The small peak at around 99.6% is due to different trigger settings for some runs in 1999, which diminished the trigger rate from 450 to 200 Hz.

From the two independent ways of determining the live-time the systematic error of the live-time measurement can be estimated. The integrated live-time used in this analysis as measured with the 10 MHz counter is $\tau = 9626571 \pm 58$ s. The same number obtained with the 1Hz trigger reads as $\tau = 9628154 \pm 337$ s. The difference is

$$\Delta\tau = 1583 \pm 342 \text{ s} \,, \tag{5.38}$$

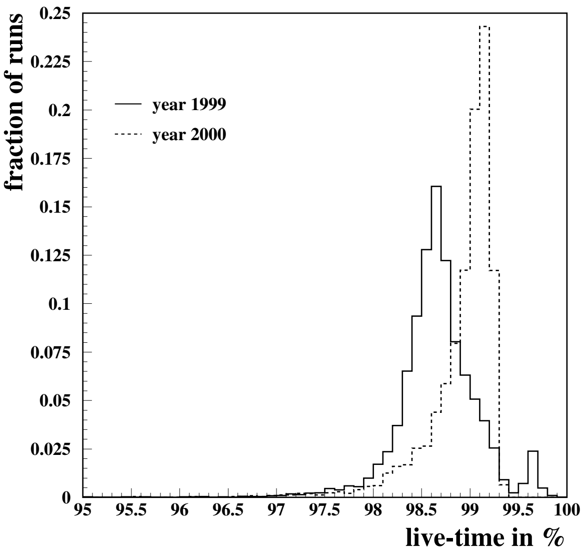

Fig. 5.16: *The live-time in percent for the 1999 and 2000 data taking periods.*

leading to a systematic uncertainty of

$$\frac{\Delta\tau}{\tau} \leq 0.0002 \text{ (95\% C.L.)} \ . \tag{5.39}$$

5.3.2 Scintillator trigger

The CTT module decides on the basis of an overlap in time between the muon chamber majority signals and the scintillator CPC signal, whether a scintillator hit is present in the event or not. The efficiency of this event classification is checked using reconstructed data from a special test production, where no trigger preselection on the data was imposed. Comparing the events with a good scintillator hit and a scintillator trigger with the total number of events with a good scintillator hit, the scintillator trigger efficiency was found to be

$$\varepsilon^{1999}_{\mathrm{SCNT,trig}} = 99.757 \pm 0.004\% \tag{5.40}$$

for the 1999 data taking period and

$$\varepsilon^{2000}_{\mathrm{SCNT,trig}} = 99.934 \pm 0.002\% \tag{5.41}$$

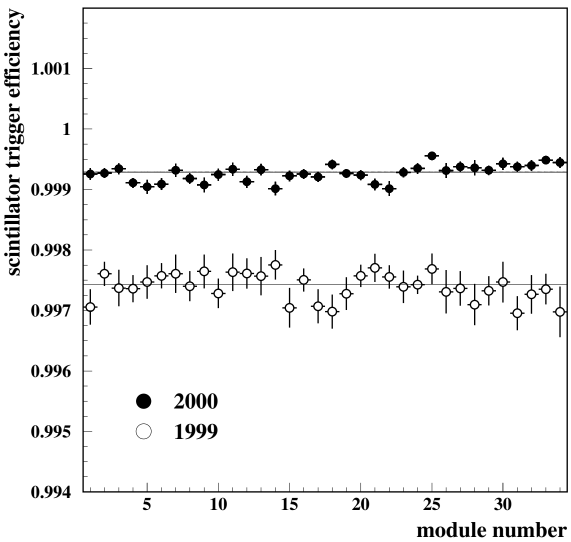

Fig. 5.17: *The scintillator trigger efficiency for the 1999 and the 2000 data taking period. The lines indicate the fitted average values.*

for the 2000 data taking period. Here a good scintillator hit is defined by a high quality reconstructed muon track, that could be extrapolated back to the scintillator module which t_0-time was used for calculating the muon chamber drift times.
Figure 5.17 shows the scintillator trigger efficiency as a function of the different scintillator modules. The module-to-module variation in 2000, where more statistics is available, deviates significantly from the fitted mean value. To account for this variation, an overall systematic error of 0.01% on the scintillator trigger efficiency is assigned.

5.3.3 Muon chamber trigger

Two effects may cause a loss of muon triggers due to the muon chamber trigger: Firstly, the majority threshold of eight (seven) hits per chamber in 1999 (2000) introduces an inefficiency for muon tracks with a low number of hits. Secondly, if a track passes the border of two CPCs, the track might not be triggered although it produced more hits than the majority threshold, but only a part of them is seen by each CPC. As the majority signals are present in the L3+C data output, the trigger efficiency can be measured for each P-chamber by comparing the trigger decision with the actual present P-chamber hits. Since for this analysis only the number of hits used in the muon track fit are of interest, the efficiency is determined versus the number of reconstructed hits.

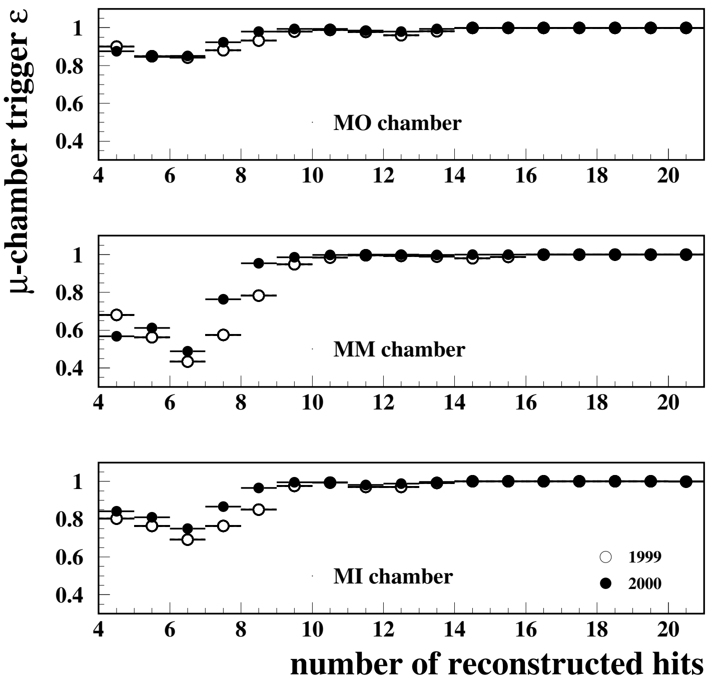

Fig. 5.18: *The muon chamber trigger efficiency for the different chambers in octant 3 versus the number of reconstructed hits.*

Figure 5.18 shows as an example the measured layer efficiencies for octant 3. The different thresholds for 1999/2000 data are clearly visible at the point the efficiency drops. The increase towards very small numbers of reconstructed hits is due to the fact, that problematic P-cells are not used in the reconstruction (see previous section), but can nevertheless trigger the CTT. The probability of triggering a muon which traverses only three P-chambers in an octant j as class 1 is

$$P(\text{class } 1|3 \text{ layers})_j = \prod_{i=1}^{3} \varepsilon_{ij}(n_{\text{hit},i}), \tag{5.42}$$

where $\varepsilon_{ij}(n_{\text{hit},i})$ is the measured layer efficiency in chamber i, and octant j given a number of $n_{\text{hit},i}$ reconstructed hits. If two octants a and b are traversed, there are two chances of being triggered, thus the probability increases to

$$P(\text{class } 1|2\cdot 3 \text{ layers}) = 1 - [1 - P(\text{class } 1|3 \text{ layers})_a][1 - P(\text{class } 1|3 \text{ layers})_b]\,. \tag{5.43}$$

The average P-chamber trigger efficiency relevant for the muons selected in this analysis (see section 6.2) is measured to be

$$\varepsilon_{\mathrm{Ptrig}} = 99.991 \pm 0.002\% \ . \tag{5.44}$$

by comparing the number of selected reconstructed class 1 triggers to the number of selected reconstructed triggers without a class 1 prerequisite. The average calculated efficiency according to equation (5.42) is $99.995 \pm 0.002\%$, which agrees well with the measured value. No significant variation of the measured trigger efficiency with momentum, zenith or azimuth angle is observed. Given the small difference to unity of $\varepsilon_{\mathrm{Ptrig}}$, no systematic uncertainty will be assigned to it.

Chapter 6

MEASUREMENT OF THE MUON FLUX

6.1 Method

6.1.1 Detector acceptance

In L3+C the rate of muons $\frac{N(\Delta p,\Delta\theta)}{\tau}$ within a given momentum and zenith angle interval (Δp, $\Delta\theta$) is measured. In order to be able to compare the measurement with other experiments and theoretical predictions, this counting rate has to be converted to a flux $\Phi(p,\theta)$. Neglecting the momentum resolution and the energy loss in the molasse overburden here, the counting rate and flux are related by (see for instance [127]):

$$\frac{N(\Delta p, \Delta\theta)}{\tau} = \int_{\Delta\Omega} d\omega \int_S d\vec{\sigma}\ \vec{r} \int_{\Delta p} dp\ \Phi(p,\theta)\ \varepsilon(p,\omega,\sigma)\ , \tag{6.1}$$

where τ denotes the livetime, $N(\Delta p, \Delta\theta)$ is the number of measured muons within the momentum and zenith bin of interest and $\Delta\Omega$ is the solid angle corresponding to $\Delta\theta$. The differential solid angle and the surface element are given by $d\omega = d\phi\ d\cos\theta$ and $d\vec{\sigma}$ respectively. S denotes an integration surface, which must be larger than the total area of L3+C, ε is the differential detector efficiency, $\vec{r}$ the unit vector in direction ω. The acceptance A allows to infer the muon flux from the counting rate by the simple relation

$$\Phi(\langle p\rangle, \langle\theta\rangle) = \frac{N(\Delta p, \Delta\theta)}{\tau}\frac{1}{\Delta p\ A}\ , \tag{6.2}$$

where $\langle p\rangle$ and $\langle\theta\rangle$ are the mean momentum and zenith angle within the flux-bin of interest. Obviously, the transition from (6.1) to (6.2) can not be done analytically in case of a complicated geometry as L3+C. Instead, a MC detector simulation with the known input flux

$$\Phi(\langle p\rangle, \langle\theta\rangle)_{MC} = \frac{N_{gen}(\Delta p, \Delta\theta)}{\tau}\cdot\frac{1}{\langle\cos\theta\rangle S\ \Delta\Omega\ \Delta p} \tag{6.3}$$

generated on the horizontal surface S within the solid angle $\Delta\Omega = 2\pi\Delta\cos\theta$ is used. After detector simulation (including the efficiencies) the acceptance can be calculated via

$$N(\Delta p, \Delta\theta)_{MC,\mathrm{reco}} = \tau\ \Delta p\ A \cdot \Phi(\langle p\rangle, \langle\theta\rangle)_{MC},$$
$$A = \frac{N(\Delta p, \Delta\theta)_{MC,\mathrm{reco}}}{N_{gen}(\Delta p, \Delta\theta)}\langle\cos\theta\rangle\ S\ \Delta\Omega\,. \tag{6.4}$$

As can be seen, the MC livetime drops out, therefore the result is independent of the assumed normalization. In L3+C, the generator surface S is zenith angle dependent for efficiency reasons (see equation (4.12)). This is taken into account by re-weighting each generated event with $w_1 = S_{\mathrm{max}}/S(\cos\theta)$, which allows to use the relation (6.3) as if a constant surface S_{max} was be used. S_{max} needs to chosen, such that $S_{\mathrm{max}} > S(\cos\theta)$ for all zenith angles.

Finally, the mean cosine of the zenith angle $\langle\cos\theta\rangle$, with which S is multiplied in equation (6.3) to convert the horizontal surface to a surface perpendicular to the direction of the solid angle bin, is obtained by assigning each generated event an additional weight $w_2 = 1/\cos(\theta_{gen})$.

Thus the acceptance factor derived from MC reads as

$$A = \frac{N(\Delta p, \Delta\theta)_{MC,\mathrm{reco}}}{\sum_i w_{1,i} \cdot w_{2,i}}\ S_{\mathrm{max}}\ \Delta\Omega\ , \tag{6.5}$$

where sum extends over all generated events within $\Delta p, \Delta\theta$.

6.1.2 Muon flux fit

So far, neither the momentum resolution, nor the energy loss in the molasse overburden have been accounted for. Due to the corresponding event migration, which was already mentioned in section 5.2.3, the relation between the number of events measured in L3+C and the muon surface spectrum at a given zenith angle bin according to equation (6.2), needs to be replaced by the matrix equation

$$\mathbf{n} = \tau \cdot \mathbf{E} \cdot \mathbf{R} \cdot \mathbf{A} \cdot \mathbf{m}\,. \tag{6.6}$$

Here $\mathbf{n}$ is the vector (histogram) of counted events n_i with measured curvatures between $[q/p_i, q/p_{i+1}]$, where q is the measured charge and p the measured momentum. The detector live-time is given by τ and $\mathbf{R}$ denotes the migration matrix, i. e. the probability of measuring a curvature q/p_i given a surface momentum p_j^s and a true charge p_j. $\mathbf{A}$ is the diagonal matrix of geometrical acceptances as a function of the surface momentum and $\mathbf{E}$ is the diagonal matrix of detector efficiencies as a function of momentum at detector level. The histogram $\mathbf{m}$ contains the true surface spectra of positive and negative muons integrated over the surface momentum bin:

$$m_i = \begin{cases} \int_{p_i}^{p_{i+1}} \Phi(p, q = -1)\, dp, & i \leq k \\ \int_{p_{i-k}}^{p_{i-k+1}} \Phi(p, q = +1)\, dp, & k < i \leq 2k \end{cases} \tag{6.7}$$

Here k denotes the number of considered surface momentum bins per muon charge. The complete detector matrix is given by $\mathbf{D} \equiv \mathbf{E} \cdot \mathbf{R} \cdot \mathbf{A}$ and will be discussed in detail in section 6.3.

The straightforward inversion of equation (6.6)

$$\widehat{\mathbf{m}} = \frac{1}{\tau}\, \mathbf{D^{-1} n} \tag{6.8}$$

is known to be problematic, because the statistical fluctuations of $\mathbf{n}$ together with the finite detector resolution $\mathbf{R}$ may lead to a solution vector $\widehat{\mathbf{m}}$ with large oscillations between neighboring bins. This is, because the non-zero off-diagonal elements in $\mathbf{R}$ introduce negative correlations between the bins of the solution $\widehat{\mathbf{m}}$. Nevertheless it can be shown, that the estimator $\widehat{\mathbf{m}}$ is unbiased and has the smallest possible variance among all unbiased estimators, i. e. $\widehat{\mathbf{m}}$ is the best possible solution (see for instance [50]).

The problem of the large negative correlations is usually overcome by modifying the initial unfolding equation (6.6): The variance of the solution is diminished by imposing an additional constraint to the data. This is done either by solving equation (6.6) iteratively starting from an initial guess $\mathbf{m}'$ and stopping the iteration, before the system has converged to $\widehat{\mathbf{m}}$ (cf. [51, 104]), or by extending the linear system (6.6) with additional regularization terms of type $\mathbf{Cm} = 0$ (cf. [35, 82, 129]).

Here the system (6.6) is regularized by imposing the constraint, that the true muon spectrum should be a power law function with a variable spectral index:

$$\Phi(p) = \Phi_0\; p^{\gamma}\,, \tag{6.9}$$

with

$$\gamma = a + b \cdot \log(p) + c \cdot \log(p)^2\ , \tag{6.10}$$

an ansatz which was used to describe the theoretical muon flux prediction of [45] and existing measurements in [79] where the above formula was rewritten to

$$\begin{aligned} \Phi(p, q = \pm 1) \;&=\; 10^{F(y, \mathbf{a}^{\pm})}\ \mathrm{m^{-2} sr^{-1} s^{-1} GeV^{-1}} \\ (y \;&=\; \log_{10}[p/\mathrm{GeV}])\,, \end{aligned} \tag{6.11}$$

with

$$
\begin{aligned}
F(y,\mathbf{a}^{\pm}) \quad = \quad & a_1^{\pm}\,\frac{1}{2}\,(y-2)(y-3)\;y \\
& -a_2^{\pm}\,\frac{1}{3}\,(y-1)(y-3)(2y-1) \\
& +a_3^{\pm}\,\frac{1}{6}\,(y-1)(y-2)\;y \\
& +a_4^{\pm}\,\frac{1}{3}\,(y-1)(y-2)(y-3)\;.
\end{aligned}
\tag{6.12}
$$

This mathematically equivalent form has the advantage, that the free parameters a_i have easy interpretations, namely the logarithm of the flux at 10 (a_1), 100 (a_2) and 1000 GeV (a_3) and the spectral index at 100 GeV (a_4). Correspondingly, the differences $a_k^+ - a_k^-$ are the logarithms of the charge ratio at 10, 100, and 1000 GeV for $k = 1-3$.

Equation (6.6) is thus replaced by the least square problem

$$
\chi^2 = \sum_{i=1}^{2d} \frac{[n_i - f_i(\mathbf{a}^{\pm})]^2}{\sigma_{n_i}^2 + \sigma_{f_i}^2(\mathbf{a}^{\pm})} = \min\;, \tag{6.13}
$$

where $2d$ is the total number of curvature bins at the detector level (d bins for each charge) and

$$
f_i(\mathbf{a}^{\pm}) = \tau\left[\left(\sum_{j=1}^{k} D_{ij}\int_{p_j}^{p_{j+1}}\Phi(p,\mathbf{a}^{-})\,dp\right) + \left(\sum_{j=k+1}^{2k} D_{ij}\int_{p_{j-k}}^{p_{j-k+1}}\Phi(p,\mathbf{a}^{+})\,dp\right)\right] \tag{6.14}
$$

is the convolution of integrated surface spectrum with the detector matrix. The sum extends over all k momentum bins of the positive *and* negative surface spectrum, because of the non zero probability for measuring the wrong muon charge in the detector.
The denominator in (6.13) is the quadratic sum of the statistical error σ_{n_i} and the error on f_i is due to the finite MC statistics available to calculate the detector matrix **D**. For the minimization of equation (6.13) the program `MINUIT` [87] was used.

Whereas this method is robust and efficiently combines the measured data into a few coefficients, it has two drawbacks:

- The actual experimental precision is obscured because of the constraint (6.9).

- Information, such as deviations of the data from the smooth function (6.9), is lost and without access to the raw detector distributions, no other flux model can be tested.

Therefore, the smooth function (6.11) is converted back to uncorrelated data points using a modified bin-by-bin procedure:
In the original bin-by-bin approach, detector effects are corrected for using the ratios of generated to selected MC events:

$$\widehat{m}_i \propto \frac{N^{MC}_{\text{gen}}(p_i)}{n^{MC}_{\text{sel}}(p_i)} n^{\text{data}}_{\text{sel}}(p_i)\,. \tag{6.15}$$

As it is shown in [50], this ansatz leads to a biased estimator $\widehat{m}_i$, if the underlying model distribution of the generated MC is not equal to the true distribution. Moreover, the usual error calculation

$$V[\widehat{m}_i] \propto \left(\frac{N^{MC}_{\text{gen}}(p_i)}{n^{MC}_{\text{sel}}(p_i)}\right)^2 n^{\text{data}}_{\text{sel}}(p_i) \tag{6.16}$$

does not take into account the loss of information introduced by the finite detector resolution.
To avoid these problems, the method is modified as follows:
In each bin of the measured histogram $\mathbf{n}$, the total number of entries n_j is regarded as being composed of events originating from different surface momentum bins m_i. For each surface bin i, a detector bin j can be found, where the number of reconstructed events $n(j|i) = \tau D_{ji} m_i$ is maximal (in the following labeled as 'signal' s_j). The other events in this particular bin, migrated to the bin from another surface momentum bin $l \neq i$ (denoted as background b_j):

$$\begin{aligned} n_j &= n(j|i) + \sum_{l=1}^{2k} n(j|l \neq i) \\ &\equiv s_j + b_j\,. \end{aligned} \tag{6.17}$$

Therefore an estimator for the muon flux $\widehat{m}_i$ can be constructed in the following way:

$$\widehat{m}_i = \frac{s_j}{D_{ji}\,\tau} = \frac{n_j - b_j}{D_{ji}\,\tau}\,. \tag{6.18}$$

The background is calculated similar to f_i in equation (6.14), but without adding the contribution of the surface bin i:

$$b_j = \tau\left[\left(\sum_{l\neq i} D_{jl}\int_{p_l}^{p_{l+1}} \Phi(p,\mathbf{a}^-)\,dp\right) + \left(\sum_{l\neq i}\int_{p_{l-k}}^{p_{l-k+1}} \Phi(p,\mathbf{a}^+)\,dp\right)\right] \tag{6.19}$$

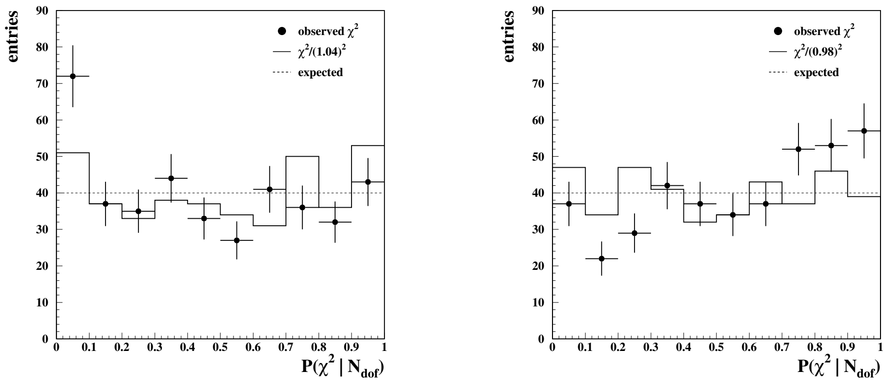

(a) *muon flux fit.* (b) *bin-by-bin method.*

Fig. 6.1: *Probability of the muon flux fit and bin-by-bin χ^2 for 400 simulated L3+C experiments. Black dots show the original distributions, solid histograms the χ^2 probabilities with rescaled errors and the dashed line the expected uniform distribution.*

The variance of $\widehat{m}_i$ is given by

$$V[\widehat{m}_i] = \frac{n_j}{(D_{ji}\tau)^2} + \sigma^2_{\mathrm{MC},i}\,, \tag{6.20}$$

where $\sigma^2_{\mathrm{MC},i}$ contains the statistical error on the detector matrix and the error on the fitting parameters $\mathbf{a}$ is neglected.

This analysis method is tested with 400 L3+C MC 'experiments': 400 muon 'data sets' are generated according to the function and parameters given in [79] and a live-time corresponding to one years' L3+C good run time. The surface spectra are convoluted with the L3+C detector matrix using a multinomial random generator. Similarly, 400 'MC sets' are generated according to the MC statistics available for this analysis and the `l3cgen` parameterization of the muon flux [78]. Thus 400 data distributions $\mathbf{n}$ and detector matrices $\mathbf{D}$ are available to investigate the mean outcome and variance of the analysis technique described above. The muon flux fit is checked by comparing the fit result $\widehat{\mathbf{a}}$ with the input parameters $\mathbf{a}$:

$$\chi^2 = (\widehat{\mathbf{a}} - \mathbf{a})^T\,\mathbf{V}[\widehat{\mathbf{a}}]^{-1}\,(\widehat{\mathbf{a}} - \mathbf{a}) \tag{6.21}$$

and the bin-by-bin method by comparing the generated spectrum with the calculated one:

$$\chi^2 = \sum \frac{(\widehat{m_i} - m_i^{\mathrm{gen}})^2}{V[\widehat{m}_i]}. \tag{6.22}$$

The probability distributions of these two χ^2's are shown in figure 6.1. Although the minimization of equation (6.13) is highly nonlinear (and thus the `MINUIT` ansatz of calculating the covariance matrix from the inverse of the Hesse-matrix is strictly speaking not correct) and the error estimation of (6.20) neglects the correlation of the parameters $\mathbf{a}$ and n_j, the flatness of the distributions is acceptable. The corresponding under- and overestimation of the fitting errors can be quantified by rescaling the errors

$$\widehat{\chi^2} = \chi^2 \frac{1}{c^2}, \tag{6.23}$$

until the distributions become flat within their statistical errors. This leads to $c = 1.04$ for the muon flux fit and $c = 0.98$ for the histograming. The estimated statistical errors are thus in very good agreement with the true errors within a few percent relative precision.

6.2 Data selection

The data selection can be subdivided into three categories: After a preselection of the data, based on the run quality and trigger decision, fiducial volume cuts are applied, which assure a good agreement between data and MC. Only high quality muon tracks are selected, in order to obtain a good momentum resolution. The subsequent efficiencies of the selections are listed in table 6.1 for data and MC. At low momenta, they are momentum dependent because due to the bending of the muon track in the magnetic field, different detector parts are passed for each momentum. Therefore the values above 80 GeV are shown, where the tracks are approximately straight lines and the momentum dependence starts flattening.
Also shown is their live-time weighted ratio

$$R = \frac{(\varepsilon_{\text{data}}/\varepsilon_{\text{MC}})_{1999} \cdot \tau_{1999} + (\varepsilon_{\text{data}}/\varepsilon_{\text{MC}})_{2000} \cdot \tau_{2000}}{\tau_{1999} + \tau_{2000}}, \tag{6.24}$$

which is a measure of the average agreement between the data and the simulation.

Data preselection

During the first two months of data taking, the scintillator detector was subject to many interventions aiming to improve the shielding of the photomultipliers from the L3 magnetic field. As a consequence both the time calibrations and efficiencies are unstable in this period, which is why only data taken after the 15th of July 1999 is

category	selection	type	data 1999	data 2000	MC 1999	MC 2000	R
pre-selection	SCNT change	r	0.635	1.000	-	-	-
	detector status	r	0.841	0.783	-	-	-
	LEP noise	r	0.840	0.416	-	-	-
	class 1	e	0.334	0.384	-	-	-
	reconstruction	e	0.880	0.844	-	-	-
	preselection total:		0.132	0.106			
fiducial volume cuts	TRIG thresh.	st	0.644	0.702	0.261	0.298	2.415
	shafts	t	0.802	0.802	0.803	0.803	0.999
	master/slave	st	0.944	0.942	0.942	0.941	1.002
	bad cells	st	0.776	0.716	0.765	0.705	1.015
	6P topo.	t	0.380	0.311	0.374	0.305	1.018
	SCNT match	t	0.921	0.918	0.951	0.952	0.967
	fiducial volume cuts total:		0.132	0.109	0.054	0.046	2.414
quality selection	SCNT Δt	t	0.959	0.955	(0.958)	(0.955)	1.001
	2·3 P segments	st	0.492	0.544	0.501	0.558	0.978
	ϕ_{loc}	st	0.631	0.640	0.635	0.643	0.995
	χ^2	st	0.893	0.890	0.949	0.949	0.940
	Z-hits	st	0.835	0.801	0.853	0.817	0.980
	P-hits	st	0.917	0.930	0.928	0.939	0.990
	double octant	t	0.995	0.995	0.994	0.994	1.001
	quality selection total:		0.203	0.220	0.227	0.248	0.890
	all selections:		0.0035	0.0025	0.012	0.011	

Tab. 6.1: *Efficiency of the applied selection cuts. The 'type' column states the object the selection is acting on: r=run, e=event, t=track, st=sub-track. The fiducial volume cut and quality selection efficiency are given for muons above 80 GeV. The last column lists the live-time weighted ratio of the data and MC efficiencies.*

used in this analysis.
While taking data, the status of the L3+C detector components has been continuously monitored and the corresponding informations were written into a database, on which bases the L3+C runs are classified as good or bad [98]. The main criteria are the stability of the high voltages of the scintillator photomultipliers and the muon chambers as well as nominal muon chamber discriminator and magnet current settings.
As shown in section 5.1, the scintillator noise, which is observed during the operation of the LEP accelerator, diminishes the efficiency of the L3+C scintillator array. Therefore, all runs with a total array rate larger than 80 kHz are not used in this analysis. As a consequence of the large background from LEP during its highest energy runs in 2000, the detector status and especially the scintillator noise were much worse in this year.
Further preselection criteria are a class 1 trigger decision, i. e. at least one triplet confined in an octant and a scintillator hit, and a fully reconstructed muon track. Due to the lower amount of disconnected P-chamber cells, a slightly larger fraction of the events was triggered as class 1 in the year 2000. The reconstruction efficiency was already discussed in section 4.4.

Fiducial volume cuts

- **trigger threshold:** No trigger simulation is implemented in the real detector MC, therefore it contains also events, which hit only two P chambers within one octant. These events are already deselected in the data by the class 1 preselection in the reconstruction or even earlier during the data taking by the trigger prescaling. To get comparable events in data and MC, a 'software class 1 trigger' is applied to the reconstructed muon chamber hits, by requiring three chambers in one octant with at least 8(7) reconstructed P-hits in 1999(2000). As expected this cut removes much more MC events. The observed efficiency ratio corresponds to the doublet fraction in the data of about 60%.

- **access shafts:** The three access shafts around the L3 cavern are known to be poorly described in the simulation [134], as there they are assumed to be empty. However, in reality they are filled with stairways or containers hosting the L3 readout electronics. During the reconstruction, an estimated traversed matter thickness X_{est} is assigned to each muon track, based on the `GEANE` backtracking through the `GEANT` model of the L3 surroundings. In the absence of access shafts, the traversed matter would read as

$$X' = \frac{X_0}{\cos\theta} + f(\theta) \; , \tag{6.25}$$

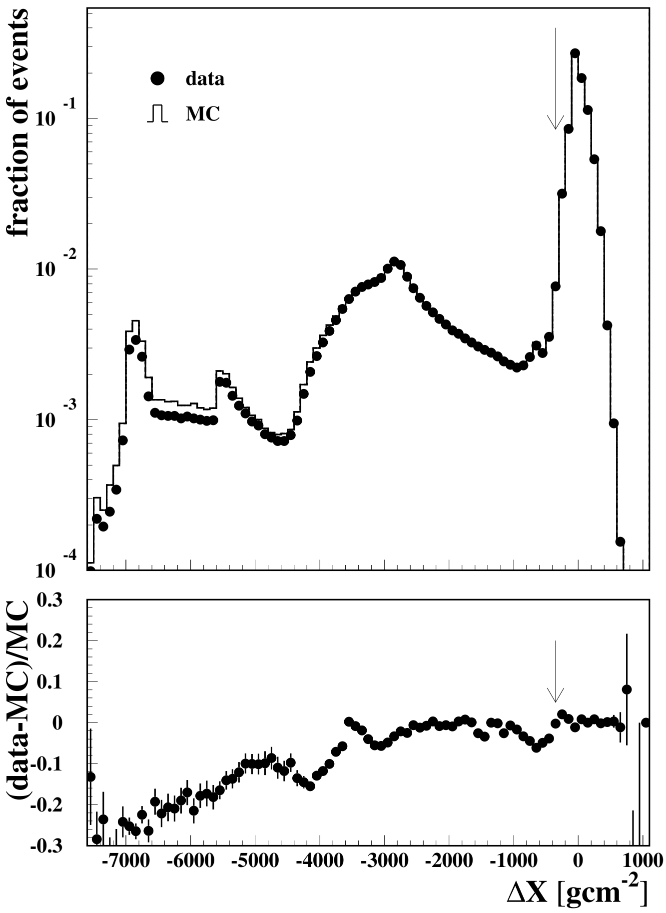

Fig. 6.2: *Access shaft deselection for muons with p>10GeV at the detector.*

where X_0 denotes the vertical matter thickness, and $f(\theta)$ is a correction due to the cylindrical shape of the L3 cavern similar to equation (6.45). The difference

$$\Delta X = X_{\mathrm{est}} - X' > -350\ \mathrm{g\,cm^{-2}} \tag{6.26}$$

is used to deselect muons, which entered the L3 cavern through the access shafts in order to avoid systematic effects at low energies due to the different total energy loss of muons in data and MC. The data and MC distributions for momenta above 10 GeV are shown in figure 6.2. As expected, more MC events are observed in the shaft regions at low ΔX due to the smaller energy loss. At higher energies, the energy loss is of less importance, therefore the cut reduces to a pure geometrical constraint and good agreement between data and the simulation is observed as can be seen in table 6.1.

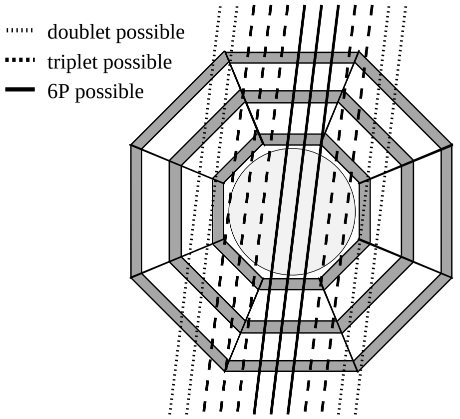

(a) *Illustration of the '6P' cut.*

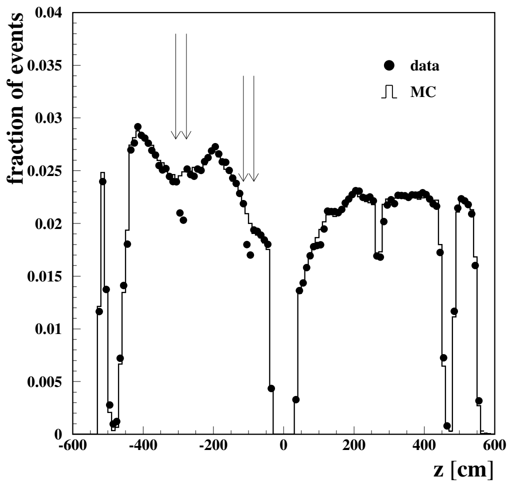

(b) *Example of the bad cell cuts for the inner Z-chambers in octants 5 and 13 in the year 2000.*

Fig. 6.3: *Muon chamber fiducial volume cuts.*

- **octant confinement (master/slave):** As mentioned earlier, the L3 muon chamber octants are divided into two independent "Master" and "Slave" sides along the LEP beam pipe. A sub-track constituted out of a segment on one side and two segments on the other side is rejected, because neither a hardware based alignment system nor offline calibration values are available for the relative alignment of these neighboring octants. Again, this cut is a purely geometrical constraint to the track, and consequently a good agreement of the related efficiencies in data and MC is observed.

- **bad cells:** In the muon chamber efficiency analysis, an 80% efficiency cut is used to classify the drift cells as good or bad (see section 5.2.1). For the spectrum analysis, the data and MC distributions of track intercepts at the chambers are re-scanned for each data taking year to apply a stronger cut of 90%. All sub-tracks, which pass such a low efficient region, are deselected. An example is shown in figure 6.3(b), where a good overall agreement between the data and MC can be seen with the exception of the regions at -300 and -100 cm, excluded by the cut. The gaps around $z = \pm$ 500 cm are due to disconnected Z-cells, which were already accounted for in the simulation. The additional excluded regions amount to 1.5% of the P-cells and 2.8% of the Z-cells in 1999 and 1.5% of the

P-cells and 5.6% of the Z-cells in 2000.
Moreover, tracks using P chamber cells at the outer edges of the layers are not selected, because the special geometry of these cells results in an electric field configuration different from the usual cells, which is however not taken into account in the time-to-distance function. An example of a side cell is shown in the reconstruction chapter in figure 4.1(e).
Only few low energetic muons pass the horizontal side octants and correspondingly the statistical errors of the chamber efficiencies and time calibration offsets are large for these octants. Therefore all sub-tracks within these octants are not used in this analysis.
By construction, this cut removes more MC than data events, because in contrast to the real detector the deselected regions are of perfect quality and 100% efficient in the simulation.

- **'6P' topology:** One of the major advantages of L3+C is the possibility of two redundant measurements of the same muon within the upper and lower detector hemisphere. As will be shown below, this allows to measure the selection efficiency in data and MC for each hemisphere and thus significantly reduces the systematic effects caused by differences between the real detector and its simulation. This on the other hand means, that only tracks can be used which are 'reachable' by the facing hemisphere. Figure 6.3(a) illustrates this constraint: Given a certain direction, most muons passing the detector have no geometrical chance for a good sub-track (dotted lines). Only a small fraction of the events (solid lines) out of the total number of class 1 triggers (dashed and dotted lines) have the possibility for a high quality sub-track in both hemispheres.
  The cut is applied based on a propagation of the reconstructed muon through the detector volume taking into account the track curvature and the energy loss in the inner detector. It removes a large amount of single triplet events, which are useless for the hemisphere efficiency analysis, but does not diminish the number of events with a double octant fit, which are finally used for the muon spectrum. The differences of about 2% between the data and the MC is due to the lower number of pure triplet tracks in the data sample before the cut, which is caused by the data P layer inefficiency explained in section 5.2.1. Given the average real detector layer efficiency of 0.987 a ratio of $R = 1.025$ would be expected, which is close to the actual observed ratio of 1.018.

- **scintillator match:** The extrapolation of the track back to the scintillator plane is demanded to intercept a scintillator cassette belonging to the module which

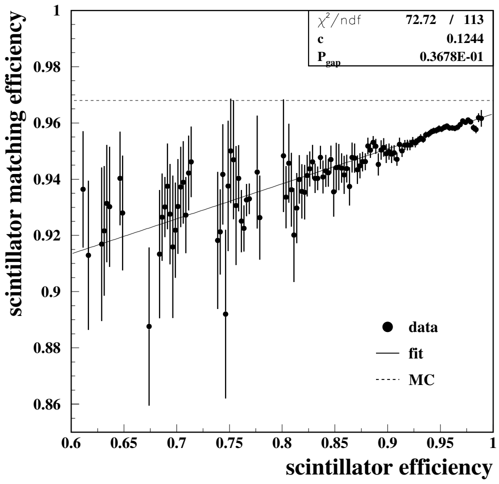

Fig. 6.4: *Scintillator matching efficiency vs. the scintillator cassette efficiency.*

registered the t_0 hit used to calculate the muon chamber drift times during the reconstruction. The cut is imposed to reject tracks with a random scintillator timing caused by the use of a scintillator noise hit. This may occur, if no 'real' t_0 hit is present in the data either because the muon entered the detector volume through one of the gaps in between the scintillator cassettes, or because no t_0 hit was registered in the array due to the inefficiency of the traversed cassette.
About 8% of all data events are removed by this cut. At this stage of the selection, when still a lot of poor quality tracks populate the sample, the cut also deselects tracks with falsely reconstructed directions. For tracks fulfilling all other selection criteria, the scintillator matching efficiency is 0.956 and 0.968 for data and MC respectively. A large fraction of the residual selection efficiency difference between data and MC is due to the scintillator cassette performance: Whereas in the simulation all cassettes are fully functional, the average efficiency of the real cassettes is about 95% after the photomultiplier time coincidence cut of 15 ns applied in the reconstruction. This is illustrated in figure 6.4, where the data scintillator matching efficiency as a function of the cassette efficiency is shown. The data was fitted with the function

$$\varepsilon_{\mathrm{SCNTmatch}} = 1 - [P_{\mathrm{gap}} + (1 - \varepsilon_{\mathrm{cass}}) \cdot c] \ , \tag{6.27}$$

where P_{gap} denotes the probability of reconstructing a muon entering through the gaps in between the scintillator cassettes and $c = P_{\mathrm{noise}} \cdot P_{\mathrm{rec}}$ is the product of the probabilities of the presence of a noise hit and the subsequent reconstruction and selection of the track. Comparing the fitted P_{gap} to the MC scintillator matching efficiency leads to an effective difference $R = 0.995$.

Quality cuts

The following quality cuts are applied to ensure a good momentum resolution:

- **Scintillator timing:** As already noted during the analysis of the L3+C scintillator system, the difference Δt between the two time measurements of the same scintillator hit is well described by a Gaussian distribution in the central region, but exhibits long tails with large time differences (see figure 5.3(a)). The correlation between this time difference and the momentum resolution normalized to its asymptotic value σ_0 at $\Delta t = 0$ is shown in figure 6.5(a). A cut is placed at

$$\Delta t < 8 \tag{6.28}$$

  to get rid of muon tracks using a photomultiplier hit with a large time slewing. As no long tails are simulated in the MC, no cut is placed there. The efficiency values shown in brackets in the MC columns in table 6.1 are the expectations according to the results of the scintillator performance analysis, which nicely agree with the observed data efficiency.

- **P segments:** Only tracks with six P segments are used for the muon spectrum analysis, as these tracks have the best momentum resolution. Due to the disconnected and bad P cells, about half of the data and MC are removed by this cut. Given the average real detector P layer efficiency of 0.987, a somewhat lower efficiency ratio R of 0.962 would be expected as actually observed for the additional* 3 P segments required by this cut.

- **Cell map validity:** The validity of the time-to-distance function of the P-cells is limited to angles $\phi_{\text{loc}} = 25^o$ with respect to the sense wire plane. Above this value the single wire resolution deteriorates, which is why a cut of

$$\phi_{\text{loc}} < 25^o \tag{6.29}$$

  is set. As can be seen by comparing the left and middle distributions in figure 6.6, events with a large ϕ_{loc} not only have a bad resolution, but also result in a biased inverse single octant momentum difference.

*The first 3 P segments are already selected with the trigger threshold cut.

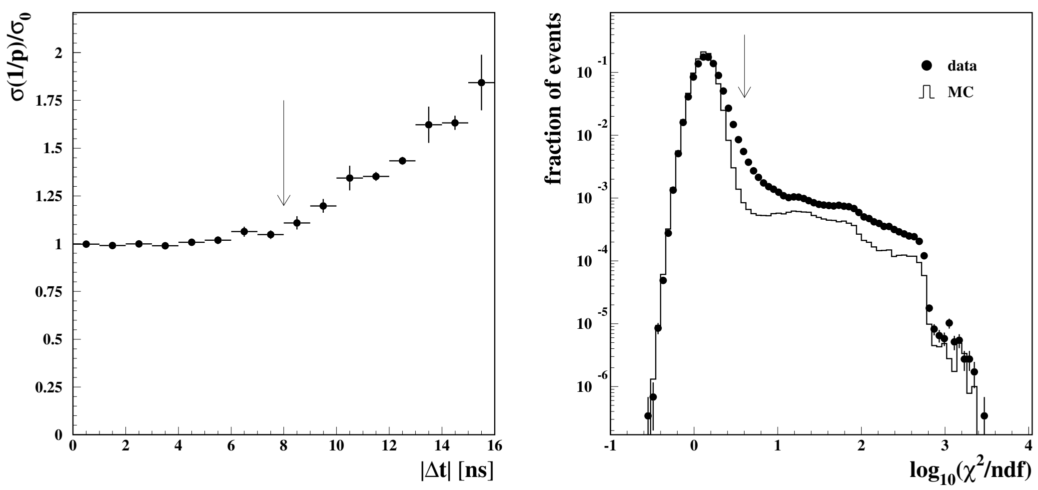

(a) *Dependence of the single octant momentum resolution above 100 GeV on the difference of the time measurements of the two scintillator photomultipliers.*

(b) *Distribution of the reduced circle fit χ^2 for data and MC above 100 GeV.*

Fig. 6.5: *Quality selection cuts.*

- **Circle fit χ^2:** The reduced χ^2 of the circular fit [90] to all P hits constituting muon a sub-track is used to identify tracks with a bad reconstruction. This variable is especially sensitive to falsely resolved hit ambiguities, which can not be detected in the `GEANE` track fit χ^2 defined in equation (4.8), because at this stage the individual sense wire measurements have already been combined into a single chamber coordinate. As shown in figure 6.5(b), both the data and the MC reduced χ^2 distributions have long tails, for which reason a logarithmic scale was chosen to display them. The somewhat worse data distribution may be addressed to the various chamber calibration uncertainties listed in section 5.2.3. A cut of

$$\chi^2/\mathrm{ndf} < 4 \tag{6.30}$$

is set to each sub-track, in order to reject mis-reconstructed tracks.

- **Z-hits:** For a well determined direction in the ZY-plane, each sub-track is required to have at least one segment with four used hits, or two segments with at least two used hits. Depending on how many Z-cells n_z are active along the track trajectory, the average real detector Z-layer efficiency of 0.917 is expected to introduce an additional data inefficiency ranging from 0.707^2 ($n_z = 2 \cdot 4$) to

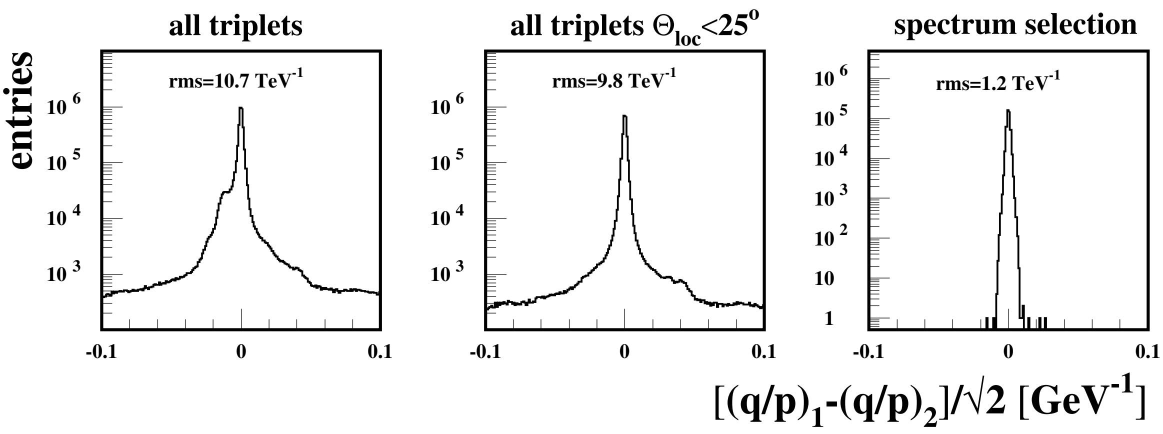

Fig. 6.6: *The single octant curvature difference above 100 GeV for different selections.*

almost 1 ($n_z = 2 \cdot 8$). The observed value of $R = 0.980$ is close to the 0.981 expected for $n_z = 2 \cdot 6$.

- **P-hits:** The accuracy of the position measurement in the P chambers, and thus the momentum resolution, is directly related to the number of used P-hits per segment, as shown in equation (5.25) for the single octant case. The hit resolution function f_{hit}, introduced in this formula, is used to deselect tracks with a low number of participating segment hits. For both sub-tracks it is required that

$$\frac{f_{\text{hit}}}{f_{\text{nom}}} \leq 1.5 \; , \tag{6.31}$$

where f_{nom} denotes the nominal hit resolution function for 16, 24 and 16 used hits in the MI, MM and MO chamber respectively. The distributions of $f_{\text{hit}}/f_{\text{nom}}$ for data and MC have already been shown in the detector performance chapter (figure 5.10(a)). The slightly worse values of the hit resolution ratio in the data can be related to dead sense wires and the single wire efficiency, which both are not simulated in the real detector MC.

- **Double octant fit:** For the selection finally used to derive the muon spectrum, a successful double octant fit is required. The corresponding efficiencies for data and MC given in table 6.1 are in good agreement at the chosen reference momentum of 80 GeV. Their momentum dependence and the needed MC tuning have been already explained in section 4.4.

$\cos\theta$	**data**	**MC**						
		5-20 GeV	20-50 GeV	50-100 GeV	0.1-0.2 TeV	0.2-0.5 TeV	0.5-1 TeV	1-10 TeV
<0.525	$1.2{\cdot}10^5$	0	$1.2{\cdot}10^3$	$6.4{\cdot}10^4$	$9.5{\cdot}10^4$	$9.7{\cdot}10^4$	$4.9{\cdot}10^4$	$9.2{\cdot}10^3$
0.525-0.600	$7.7{\cdot}10^5$	0	$2.9{\cdot}10^4$	$3.8{\cdot}10^5$	$4.5{\cdot}10^5$	$4.4{\cdot}10^5$	$2.1{\cdot}10^5$	$3.8{\cdot}10^4$
0.600-0.675	$1.5{\cdot}10^6$	1	$1.5{\cdot}10^5$	$6.0{\cdot}10^5$	$6.1{\cdot}10^5$	$5.8{\cdot}10^5$	$2.7{\cdot}10^5$	$4.7{\cdot}10^4$
0.675-0.750	$2.0{\cdot}10^6$	10	$3.0{\cdot}10^5$	$6.7{\cdot}10^5$	$6.8{\cdot}10^5$	$6.3{\cdot}10^5$	$2.8{\cdot}10^5$	$4.9{\cdot}10^4$
0.750-0.825	$2.4{\cdot}10^6$	30	$4.7{\cdot}10^5$	$5.6{\cdot}10^5$	$5.4{\cdot}10^5$	$4.9{\cdot}10^5$	$2.1{\cdot}10^5$	$3.6{\cdot}10^4$
0.825-0.900	$3.3{\cdot}10^6$	$2.6{\cdot}10^2$	$8.2{\cdot}10^5$	$5.4{\cdot}10^5$	$5.0{\cdot}10^5$	$4.4{\cdot}10^5$	$1.9{\cdot}10^5$	$3.1{\cdot}10^4$
0.900-0.938	$2.8{\cdot}10^6$	$2.0{\cdot}10^2$	$6.2{\cdot}10^5$	$6.2{\cdot}10^5$	$6.7{\cdot}10^5$	$5.9{\cdot}10^5$	$2.5{\cdot}10^5$	$4.0{\cdot}10^4$
0.938-0.975	$3.6{\cdot}10^6$	$8.9{\cdot}10^2$	$1.0{\cdot}10^6$	$5.5{\cdot}10^5$	$4.9{\cdot}10^5$	$4.2{\cdot}10^5$	$1.7{\cdot}10^5$	$2.8{\cdot}10^4$
0.975-1.000	$3.8{\cdot}10^6$	$2.2{\cdot}10^3$	$1.0{\cdot}10^6$	$6.8{\cdot}10^5$	$6.3{\cdot}10^5$	$5.3{\cdot}10^5$	$2.2{\cdot}10^5$	$3.5{\cdot}10^4$
total:	$2.0{\cdot}10^7$	$3.6{\cdot}10^3$	$4.4{\cdot}10^6$	$4.7{\cdot}10^6$	$4.7{\cdot}10^6$	$4.2{\cdot}10^6$	$1.9{\cdot}10^6$	$3.1{\cdot}10^5$
live-time [d]:	$1.1{\cdot}10^2$	1.8	29	79	$3.2{\cdot}10^2$	$1.2{\cdot}10^3$	$5.7{\cdot}10^3$	$5.2{\cdot}10^3$

Tab. 6.2: *Number of data and MC event used in this analysis.*

After all these selections, $2.0 \cdot 10^7$ events remain for the muon spectrum analysis. The number of events as a function of zenith angle bin and the corresponding selected MC events are listed in table 6.2. The gain in momentum resolution is illustrated in figure 6.6, where the inverse single octant momentum difference of all triplets (left) and of the finally selected events (right) is shown. As can be seen, the long tails of the raw sample are completely removed by the selection, and a resolution improvement of about a factor 10 is achieved.

6.3 Detector matrix

The detector matrix **D** in equation (6.8) describes the measurement process in between the observed data distribution at the detector level and the muons at surface above the L3 detector. It is composed of a migration matrix **R**, the acceptance matrix **A** and the detector efficiency matrix **E**. The major part of this analysis so far was dedicated to collect the relevant informations needed to construct **E** and **R**. Before combining them with the acceptance **A**, to form the actual detector matrix, only one further correction is needed, namely the hemisphere efficiencies, which take into account the differences between data and MC revealed in the previous section.

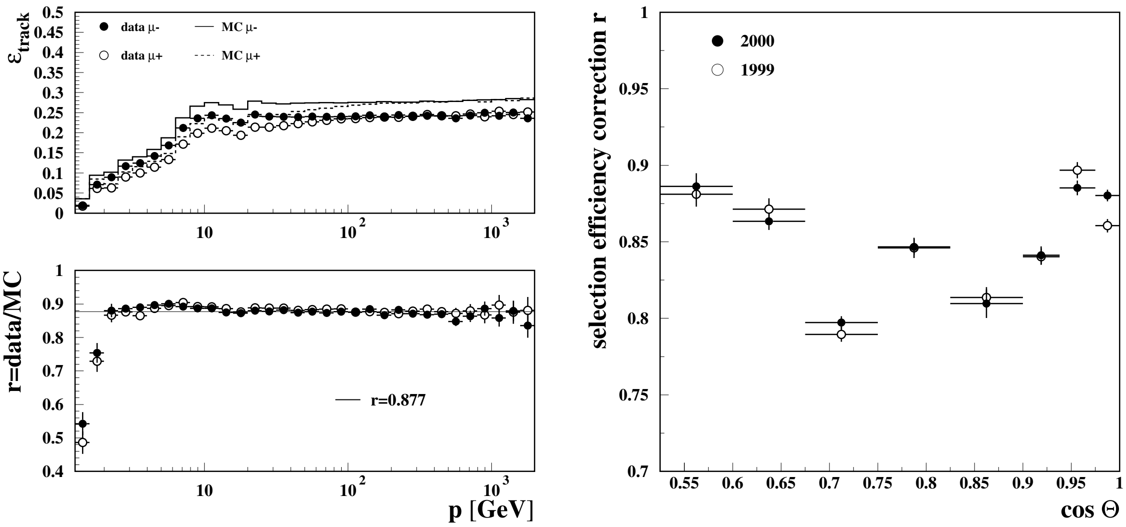

(a) *Hemisphere efficiencies in the year 2000 (averaged over all zenith angles).*

(b) *Asymptotic selection efficiency correction versus zenith angle for the two data taking years.*

Fig. 6.7: *Selection efficiency correction.*

6.3.1 Hemisphere efficiencies

Following the method proposed in [117], the independent measurements of the same muon in two detector hemispheres are used to measure the detection efficiency of each of the hemispheres separately: If a track in one detector half i satisfied all* above mentioned selection criteria, the presence of a selected track in the facing half j is checked. The hemisphere efficiency is then measured as a function of charge q, momentum p and zenith angle θ via

$$\begin{aligned} \varepsilon_j(q,p,\theta) &= P\,(\text{selected in j} \,|\, \text{selected in i}, q_i = q, p_i = p, \theta_i = \theta) \\ &= \frac{N(j\&i)}{N(i)}\,, \end{aligned} \tag{6.32}$$

where $N(j\&i)$ is the number of selected events in hemisphere j and i and $N(i)$ denotes the number of selected events in hemisphere i, regardless of the selection in hemisphere j. All selections, which act on a sub-track, labeled as type 'st' in table 6.1, can be considered as uncorrelated between the hemispheres and thus the full track

*Obviously, the double octant fit criterion can not be applied here.

efficiency reads as

$$\varepsilon_{\text{track}} = \varepsilon_i \cdot \varepsilon_j \ . \tag{6.33}$$

The ratio

$$r = \frac{\varepsilon_{\text{track}}^{\text{data}}}{\varepsilon_{\text{track}}^{\text{MC}}} \tag{6.34}$$

of the data and MC track selection efficiency is used to take into account the differences between the real detector and its simulation and will be referred to as the selection efficiency correction in the following. The year 2000 track efficiencies for data and MC as well as the corresponding ratio are shown in figure 6.7(a), averaged over all zenith angles. As can be seen, the ratio r exhibits an asymptotically flat behavior at high momenta, when the magnetic bending of the muon track becomes negligible and the tracks traverse the same detector regions. At low energies a charge dependence of the efficiencies is observed, because muons of different charges are bent into different detector parts. For each zenith angle bin alone, the available statistics are not sufficient for a determination of the selection efficiency correction up to the highest energies. Therefore the measured values are averaged above 80 GeV assuming the flat behavior observed on average.

The mean asymptotic selection efficiency correction amounts to 0.877 in 2000 and 0.897 in 1999. As can be seen in figure 6.7(b) it is not uniform with respect to the zenith angle of the muon track.

6.3.2 Migration matrix

The migration matrix **R** is calculated using the MC simulation of the L3+C mass overburden and the detector resolution. The latter had to be tuned to match the data as described in section 5.2.3. The matrix elements R_{ij} denote the probability for measuring a curvature q/p_i^{d} in the detector given a surface momentum and charge of qp_j^{s}. They are given by

$$R_{ij} = \frac{n(q/p_i^{\text{d}} \mid qp_j^{\text{s}})}{n(qp_j^{\text{s}})} \ , \tag{6.35}$$

where $n(q/p_i^{\text{d}} \mid qp_j^{\text{s}})$ is the number of selected events with measured curvature q/p_i^{d} and an original surface momentum qp_j^{s} and $n(qp_j^{\text{s}})$ is the total number of selected events with a surface momentum of qp_j^{s}. A graphical representation of the migration matrix of the vertical and most inclined zenith angle bin can be seen in figure 6.8. As expected, most of the probability is centered around the diagonal elements at high energies, whereas the most probable reconstructed momentum is lower than the surface momentum at

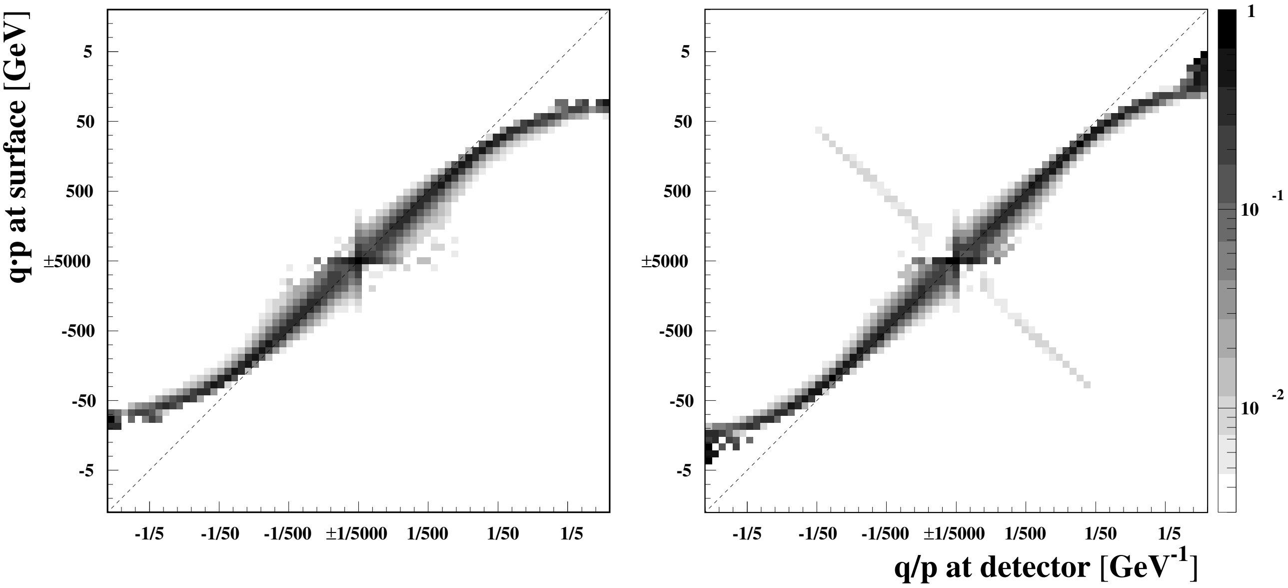

(a) $0.525 < \cos(\theta) < 0.600$ (b) $0.975 < \cos(\theta) < 1.000$

Fig. 6.8: *Migration matrices for the first and last zenith angle bin as derived from the simulation of the molasse overburden and detector resolution. The gray scale map indicates the migration probability. The dashed line is the expectation for the maximum probability in case of the absence of energy loss in the molasse. The bins labeled as* ±5000 *and* $\pm1/5000$ *contain all momenta up to* $\pm\infty$ *and curvatures down to 0.*

low energies due to the energy loss in the molasse. The entries perpendicular to the main diagonal in the vertical zenith angle matrix are due to muon tracks to which the wrong charge has been assigned during the reconstruction. This happens for special event topologies, where all six P segments of the muon track happen to be on one side of vertically aligned drift cells and the corresponding left-right ambiguity is incorrectly resolved. Given the arrangement of the L3 muon chamber octants, this occurs mainly for zenith angles around 0 and 45 degrees.

Above 5000 GeV only few MC events are left for the calculation of the migration probability. As these energies are anyway out of the range of this analysis, they are accumulated inside one 'overflow' bin for data and MC.

6.3.3 Effective acceptance

The full detector matrix $\mathbf{D} \equiv \mathbf{E} \cdot \mathbf{R} \cdot \mathbf{A}$ is calculated for each zenith angle bin under study via

$$D_{ij} = \varepsilon^{\mathrm{TRIG}} \, \varepsilon_i^{\mathrm{SCNT}} \, r_i \, R_{ij} \, \varepsilon_j^{\mathrm{loss}} \, A_j \; . \tag{6.36}$$

The migration matrix $\mathbf{R}$ and the selection efficiency correction r have been explained just above. The geometrical acceptance $\mathbf{A}$, which is depending on the surface momentum, was discussed at the beginning of this chapter. The trigger efficiency $\varepsilon^{\mathrm{TRIG}}$ is almost unity as shown in section 5.3.1. The scintillator efficiency is depending on time t and noise rate R. Moreover it is different for each individual scintillator cassette c, which introduces a geometrical and thus zenith angle dependence, and due to the bending of the muon in the magnetic field also a dependence on the muon charge and its momentum at the detector. The average scintillator efficiency as a function of these variables is determined by re-weighting all data events in detector bin i with the efficiency of the used cassettes and calculating the ratio to the unweighted number of events n_i:

$$\varepsilon_i^{\mathrm{SCNT}} = \frac{\displaystyle\sum_{\text{events}} \frac{1}{\varepsilon(c_k, t_k, R_k)}}{n_i} \; . \tag{6.37}$$

The event loss factors f listed in table 4.3, are incorporated via

$$\varepsilon_j^{\mathrm{loss}} = \frac{f_{\mathrm{MC},j}}{f_{\mathrm{data}}} \; . \tag{6.38}$$

The detector matrix as given in equation (6.36) is used in the muon flux fit. For illustration purpose and to be able to compare to other experiments, an effective acceptance as a function of the surface momentum is desirable. This can be constructed by summing over the columns of the detector matrix, such that the effective acceptance a_j states the overall geometrical factor for a muon in surface bin j for being detected and selected in any of the detector bins i. Multiplied with the live-time of the used data taking runs, the total exposure is obtained. It is shown in figure 6.9 for positive and negative muons as a function of surface momentum. As can be seen, it rapidly decreases at low energies, which is due to the momentum cutoff caused by the molasse overburden. Below 200 GeV, positive and negative muons have different acceptances, because the magnetic field bends their tracks into opposite directions and correspondingly different detector regions. At large momenta, the acceptance is approximately flat with a slight decrease because of a worse performance of the full detector fit and a more difficult reconstruction due to rising production of delta rays.

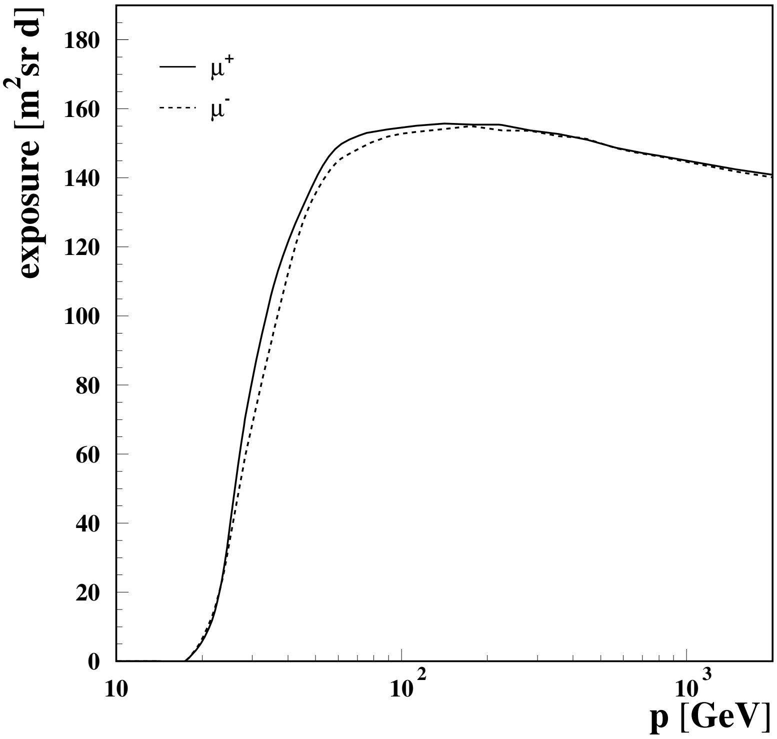

Fig. 6.9: Detector exposure as a function of surface momentum for positive and negative muons.

6.4 Systematic uncertainties

In the following the systematic uncertainties of the muon spectrum and the charge ratio will be estimated. They can be subdivided into momentum scale uncertainties δ_p and normalization uncertainties Δ_n. The latter may cause a systematic shift of the absolute flux independent of momentum. In case the bias normalization is different for the positive and negative muon flux, the charge ratio can also be affected. Due to the expected steepness of the muon spectrum

$$\Phi(p) \sim \; p^{-\gamma} \tag{6.39}$$

even a small bias in the momentum scale can introduce a considerable change to the flux and charge ratio measurement:

$$\Phi(p \pm \delta_p) \approx \Phi(p) \; \cdot \; \left(1 \mp \gamma \, \frac{\delta_p}{p}\right) \; . \tag{6.40}$$

Where appropriate, the estimated uncertainties will be cross-checked by investigating the difference of the muon flux and charge ratio between different independent subsamples. For this purpose, the zenith angle spectra were measured separately for

- the two data taking years 1999 and 2000 (Δ_y). This corresponds to different detector acceptances due to the time dependent scintillator efficiency and the different drift cell status in 1999 and 2000. Moreover, the different alignment and cell map calibrations for the two years can be checked.
- muon tracks reconstructed in 'master' or 'slave' part of the detector, i. e. a subdivision of the data sample along the z-axis of the detector (Δ_Z). Thus two completely independent subdetectors are used corresponding again to different acceptances and calibration constants.
- muons passing the inner L3 detectors and muons traversing the outer $\pm Z$ regions of the detector (Δ_{D}). In addition to the complementary detector regions used here, a different momentum resolution is expected for these subsamples due to the energy loss and multiple scattering in the inner detectors.

Assuming independent systematic errors for each subsample, the relative flux difference of muons of positive and negative charge should follow

$$\frac{\Delta\Phi}{\langle\Phi\rangle} \leq \left(2 \cdot \Delta_n^2 + \left[2 \cdot \frac{\Phi(p \pm \delta_p)}{\langle\Phi\rangle}\right]^2\right)^{\frac{1}{2}} . \tag{6.41}$$

The shifted spectra are obtained by changing the integral in equation (6.14) via

$$\int_{p_j}^{p_{j+1}} \Phi(p, \mathbf{a}^{\pm})\, dp \quad \longrightarrow \quad \int_{p_j+\delta_p}^{p_{j+1}+\delta_p} \Phi(p, \mathbf{a}^{\pm})\, dp \tag{6.42}$$

and repeating the muon flux fit for each momentum scale uncertainty δ_p.

6.4.1 Momentum scale uncertainties

The total momentum scale uncertainty is given by

$$\Delta p = \delta_B \oplus \delta_{\mathrm{al}} \oplus \delta_{\mathrm{eloss}} \oplus \delta_X \ , \tag{6.43}$$

with the magnetic field related uncertainty δ_B, the muon chamber alignment uncertainty δ_{al}, the theoretical energy loss uncertainty δ_{eloss} and the uncertainty due to the molasse thickness δ_X. Both the alignment and magnetic field uncertainties affect the momentum at the detector level. To be able to convert the related momentum scale uncertainties to surface level, a parameterization of the mean energy loss in the molasse predicted by the simulation of the L3+C surroundings is used:

$$\Delta E(\theta) = (a + b \cdot E)\, X(\theta) \,, \tag{6.44}$$

with energy loss constants $a = 2.29$ MeV/gcm^{-2} and $b = 4.81 \cdot 10^{-6}$/gcm^{-2}. The average traversed matter thickness as function of zenith angle θ can be approximated by

$$X(\theta) = X(\theta)_{\text{mag}} + \frac{X_0}{\cos\theta} + X_c\left(\frac{1}{\cos\theta} - 1\right) \,, \tag{6.45}$$

where $X_0 = 6854$ gcm^{-2} denotes the vertical molasse thickness and $X_c = 4146$ gcm^{-2} is a correction due to the curved ceiling above the L3 detector. The thickness of the L3 magnet is approximately constant with the zenith angle, because of its cylindrical shape: $X(\theta)_{\text{mag}} \approx 1227$ gcm^{-2} .

Magnetic field uncertainty

The muon momentum calculated from the track radius is directly related to the magnetic field strength, as can be seen from equation (3.1). The overall relative magnetic field strength uncertainty is estimated to be $\leq 0.4\%$ in [41], leading to a momentum scale uncertainty of

$$\delta_B = 0.004 \cdot [p - \Delta p(\theta)] \,, \tag{6.46}$$

where p denotes the muon momentum at surface and $\Delta p(\theta)$ is the mean momentum change from surface to detector level according to equation (6.44).

Muon chamber alignment

As discussed in the detector performance chapter, a muon chamber mis-alignment can introduce a bias ΔC to the measured track curvature $C = q/p$:

$$p = q/C \;\rightarrow\; p' = q/(C + \Delta C) \,. \tag{6.47}$$

The systematic uncertainty of the double octant curvature measurement was estimated to be $\Delta C \leq 0.070$ TeV^{-1} in section 5.2.2 for one octant pair. Assuming no correlation between the octants, this uncertainty should be diminished by a factor of $1/\sqrt{N}$ depending on the number of octant pairs N used in the muon flux measurement. The alignment related momentum scale uncertainty reads as

$$\delta_{\text{al}} = p^* \, \frac{\Delta C}{q/p^* + \Delta C} \,, \tag{6.48}$$

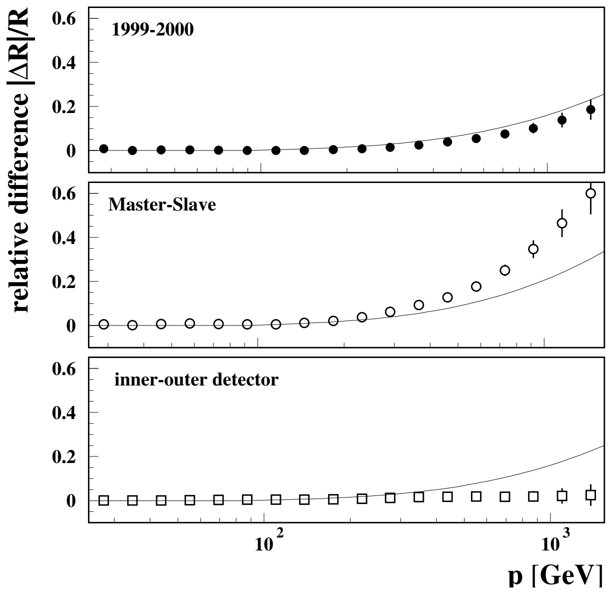

Fig. 6.10: *Charge ratio difference between data subsamples averaged over the zenith angle. The line shows the expected uncertainty.*

where $p^* = p - \Delta p(\theta)$ with the energy loss correction Δp as defined above.
The estimated alignment uncertainty ΔC is cross-checked by calculating the charge ratio difference between the data subsamples averaged over the zenith angle. Its momentum dependence is shown in figure 6.10. As can be seen, the order of magnitude of the observed difference is correctly predicted by this estimation, but in case of the master-slave analysis, a significantly larger difference is obtained. The observed difference is well described by $\Delta C = 0.075\ \mathrm{TeV}^{-1}$, thus either the cut variation performed in 5.2.2 underestimated the actual errors by a factor 1.6 or there exists an unknown correlation in between the alignment shifts on one detector side. For each zenith angle, the observed master-slave alignment difference is listed in table 6.3. Values close to zero, as for instance between 0.600 and 0.675, of course do not necessarily mean a good alignment, as only differences between the octants can be measured. Therefore, the maximum of the observed difference and the average difference will be used as an estimate of the alignment uncertainty as a function of zenith angle.

$\cos(\theta)$	ΔC [TeV^{-1}]
0.525-0.600	0.066
0.600-0.675	0.004
0.675-0.750	-0.017
0.750-0.825	0.101
0.825-0.900	0.125
0.900-0.938	0.152
0.938-0.975	0.100
0.975-1.000	0.080

Tab. 6.3: *Observed alignment differences between the master and slave side of the detector.*

Energy loss calculation

The `GEANT3` MC code, which is used in L3+C for the simulation of the detector and the energy loss calculation in the molasse overburden, is not a dedicated program for tracking high energy muons through thick layers of matter. Therefore it is crucial to check its validity over the full L3+C momentum range. As mentioned in section 4.3, the original code version was changed following the suggestions of [39] to fix the wrong treatment of photonuclear interactions and will be labeled `GEANT3+GMU` in the following. No theoretical calculations are available for the special L3+C molasse material, therefore monoenergetic muon beams with energy 100, 200, 400, 2000, and 4000 GeV are tracked through 30 meters of 'standard rock', which is one of the reference materials used to compare different calculations and is characterized by an average density of $\rho = 2.65$ gcm^{-3} and the mean charge per mass ratios $\langle Z/A\rangle = 0.5$ and $\langle Z^2/A\rangle = 5.5$. Thus it is fairly close to the L3+C molasse where $\rho = 2.38$ gcm^{-3}, $\langle Z/A\rangle = 0.5$ and $\langle Z^2/A\rangle = 5.8$. In figure 6.11(a) the obtained relative energy loss is compared to two calculations [74, 107], the simulation result of the original `GEANT3` version and a contemporary MC program [48]. As can be seen, the overall agreement is very good. For better visibility, the average of the theoretical calculations [74, 107] is subtracted from the determined relative energy losses, as shown in figure 6.11(b). In this representation a clear bias of the `GEANT3+GMU` energy loss calculation towards an about 0.3% to high energy loss can be seen. The reason can be traced back to a too high pair production cross section of `GEANT3` with respect to [74], which is compensated in the standard `GEANT3` implementation, due to the wrong low photonuclear interaction cross section. Since this bias was discovered after the MC production was finished, it is corrected

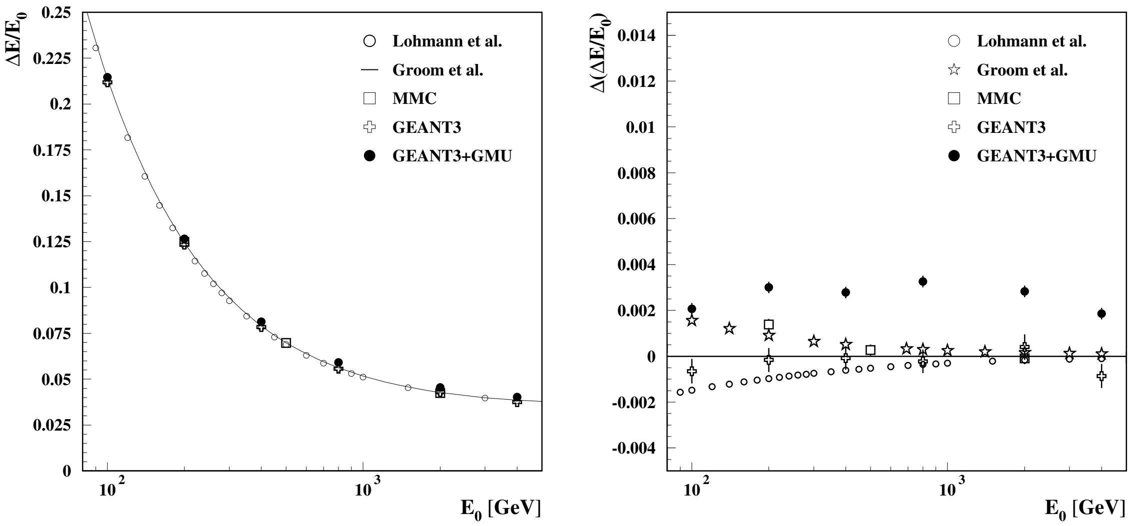

(a) *Relative energy loss in 30 meters of standard rock.*

(b) *Relative energy loss differences between the models.*

Fig. 6.11: Comparison of different energy loss calculations.

for a posteriori on an event by event basis by shifting the reconstructed MC momenta towards higher values. Given the crudeness of this method and the differences of the model predictions at lower energies, the full 0.3% are assigned as a systematic error on the relative energy loss corresponding to

$$\delta_{\text{eloss}} = 0.003 \, \frac{X(\theta)}{X(0)} \cdot p \,, \tag{6.49}$$

where $X(\theta)$ denotes the matter thickness as function of zenith angle θ, which is given in equation (6.45).

Molasse overburden

Apart from the actual model used to simulate the energy loss, an error in the estimated amount of molasse overburden X can cause an additional bias in the momentum scale. Two survey drillings at different locations close to L3+C have been performed in the years 1982 and 1996. The corresponding calculated average molasse densities agree within 0.1% [134]. The uncertainty due to molasse inhomogeneities and of surface installations not included in the L3+C simulation is estimated by studying the variance of the muon flux as a function of azimuthal angle. Since at L3+C energies geomagnetic

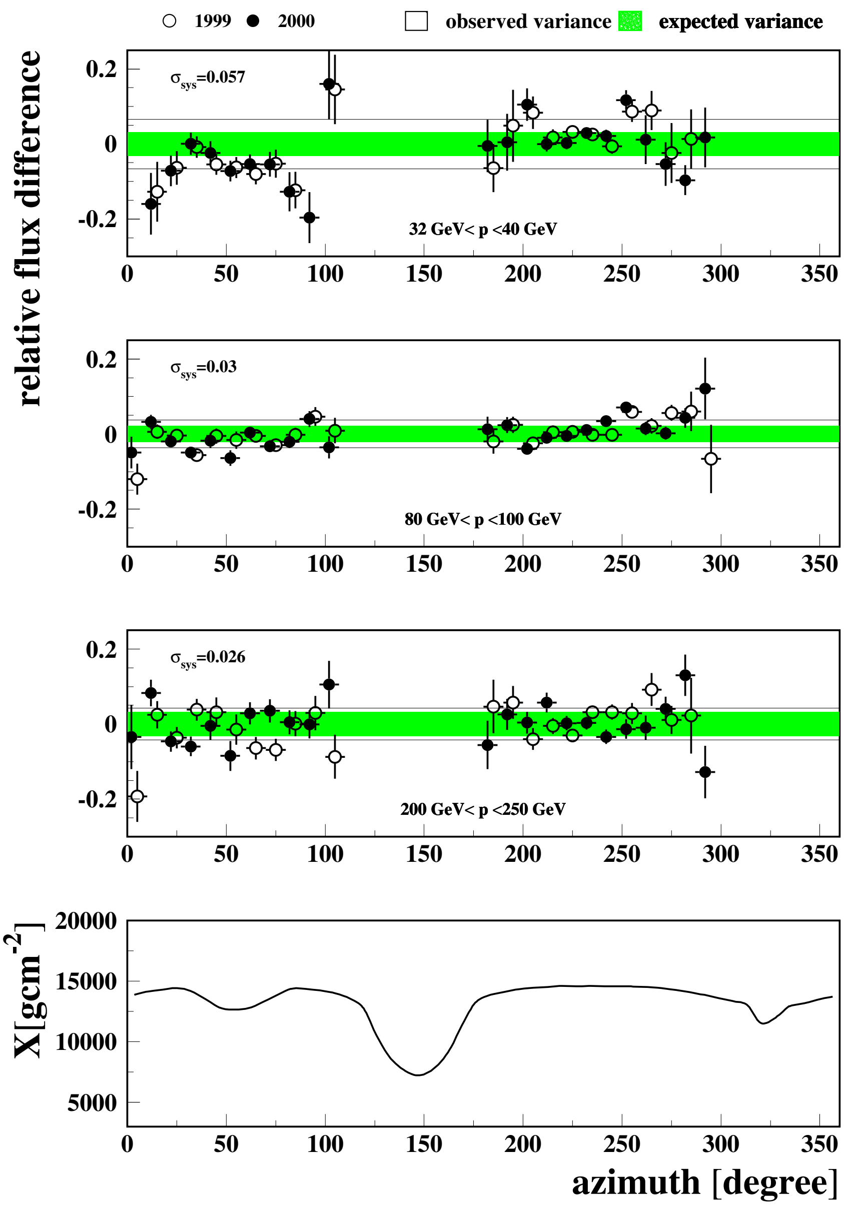

Fig. 6.12: *Example of the azimuth dependence of the relative muon flux difference for three different momenta at zenith angles between* $0.600 < \cos(\theta) < 0.675$. *The lowest plot illustrates the average mass profile within this zenith angle bin. The three access shafts (cf. figure 4.6(a)), for which the amount of traversed matter is lower, are visible at 50, 150 and 325 degrees. For two of the shafts, all events were deselected by the matter cut (6.26). The year 2000 fluxes are slightly shifted in azimuth for better visibility.*

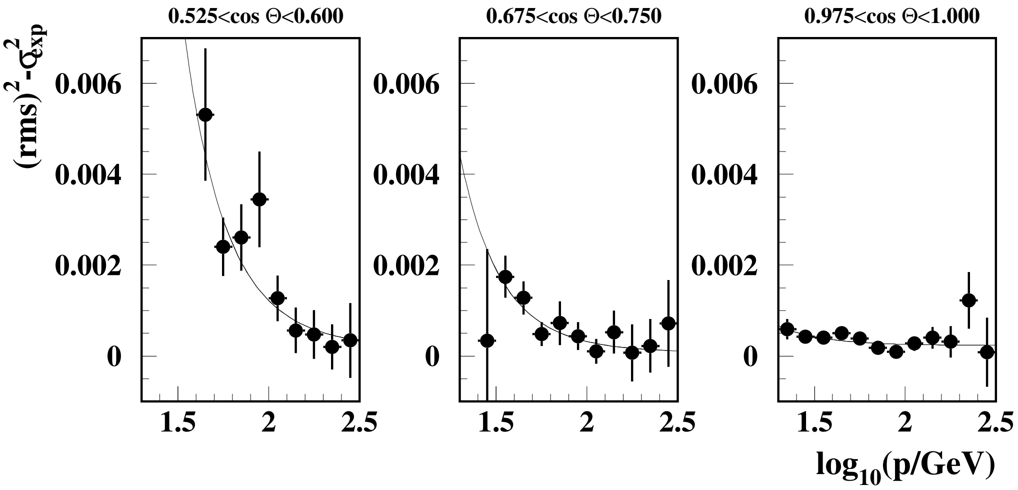

Fig. 6.13: *Systematic molasse error as a function of muon momentum for three different zenith angles. The line shows the fitted function (6.51) with parameters $\Delta\rho = 0.07$ (left), 0.04 (middle) and 0.02 gcm^{-3}(right).*

effects are not important, a flat distribution is expected within the errors. An example of the relative azimuthal variation of the muon flux around its mean value is shown in figure 6.12. The observed variation at low energies is clearly much larger than expected from the individual statistical errors. Moreover, a strong correlation of the difference is visible between the two data taking years, which indeed hints at local molasse density variations, rather than a detector efficiency effect, as the detector status differs for the two periods. The systematic effect is quantified by comparing the observed root mean square to the expected variance $\sigma_{\rm exp}$ calculated on the bases of the statistical errors of the flux measurements

$$\sigma^2_{\rm sys} = ({\rm rms})^2 - \sigma^2_{\rm exp} \,. \tag{6.50}$$

The momentum dependence of $\sigma^2_{\rm sys}$ is shown in figure 6.13 for each of the studied zenith angle bins. Assuming that the observed increase of $\sigma^2_{\rm sys}$ at low energies is due to a deviation of the average molasse density from its nominal value $\rho_0 = 2.38$ gcm^{-3}, the distributions are fitted with

$$\sigma^2_{\rm sys} = \left(\frac{\Phi(p,\theta) - \Phi(p+\delta_X,\theta)}{\Phi(p,\theta)}\right)^2 + \Delta^2_{\rm n} \,, \tag{6.51}$$

where $\Phi(p,\theta)$ is the muon flux averaged over all azimuth angles and $\Delta_{\rm n}$ describes the asymptotically flat systematic influence of the detector acceptance. The effective momentum shift δ_X is given by

$$\delta_X = (a + b \cdot p)\ (X(\theta) - X(\theta)') \tag{6.52}$$

with energy loss constants a and b and the nominal matter thickness X as defined in equations (6.44) and (6.45). The matter thickness at a density different from the nominal one is

$$X(\theta)' = X_{\text{mag}} + \frac{\rho_0 + \delta\rho}{\rho_0}\left[\frac{X_0}{\cos\theta} + X_c\left(\frac{1}{\cos\theta} - 1\right)\right]\ . \tag{6.53}$$

The fitted Δ_{n} are between 0.6 and 2.8% and the obtained density deviations $\delta\rho$ range from 0.02 to 0.07 gcm^{-3}. Examples of the momentum dependence of the systematic errors are shown in 6.13 for three different zenith angles. in figure 6.13. An increase of $\delta\rho$ with the zenith angle is observed, which is interpreted as the result of the rising probability for encountering a molasse inhomogeneity, because the scanned molasse volume increases with $\cos(\theta)^{-1}$. The average density deviation

$$\langle\delta\rho\rangle = 0.05\ \text{gcm}^{-3} \tag{6.54}$$

is used for the estimated molasse related momentum scale uncertainty.
This corresponds to a 2% error on the density, which is much larger than the difference of 0.1% between the two test drillings mentioned above. However, at a given depth, the two measured density profiles show differences of up to 0.2 gcm^{-3}, which indeed indicates the presence of large variations of the molasse density. Moreover, a variation of the effective surface height of 30 m $\cdot$ 0.02 = 0.6 m does not seem unlikely given the fact, that the buildings and other surface installations above L3 are not taken into account in the L3+C MC model of the L3 surroundings.

Total momentum scale uncertainty

The different contributions to the vertical momentum scale uncertainty as well as the total uncertainty obtained by adding the individual errors in quadrature is shown in figure 6.14. At low energies the molasse uncertainty contributes the largest fraction, whereas above 100 GeV the alignment uncertainties dominate.

6.4.2 Normalization uncertainties

The accuracy of the overall normalization of the muon flux is limited by the precision of the detector efficiency measurements and the extent to which the real detector is

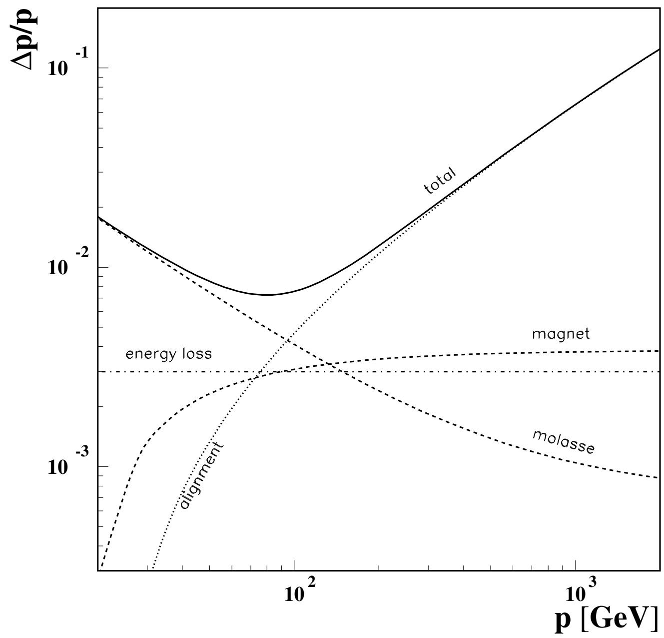

Fig. 6.14: *Relative systematic momentum scale uncertainty as a function of surface momentum for the vertical direction.*

described by the simulation model.
The systematic uncertainty of the live-time and the trigger and scintillator efficiencies estimated in chapter 5 give rise to a global relative normalization uncertainty of $\Delta_{\mathrm{g}} = 0.007$, dominated by the scintillator efficiency uncertainty.
Furthermore, the different quality selection efficiencies for data and MC observed in section 6.2 may introduce a biased normalization in case they are not fully compensated by the selection efficiency correction method. Therefore, the stability of the calculated acceptance under the variation of the quality selection cuts is investigated. The following cuts are varied:

- the requirement on the reduced circle fit χ^2 is changed from 4 to 25,
- the minimum cut on the number of hits on a Z-subtrack is put to 2 (below obviously no Z-track-reconstruction is possible),
- the quality cut on the normalized hit resolution function $f_{\mathrm{hit}}/f_{\mathrm{nom}}$ is increased from 1.5 to 3,
- the requirement on the local track angle wrt. the sense wire plane (ϕ_{loc}) is changed

from 25 degrees to 23 and 27 degrees and

- the minimum number of P-segments constituting the track in the xy-plane is lowered from 6 to 5.

For tracks with position measurements in vertically aligned drift cells, the reconstruction algorithm sometimes fails to determine the correct charge. In the migration matrix, these events populate the diagonal line, which is perpendicular to the band of maximal probability as shown in figure 6.8(b). In order to study the influence of this charge confusion on the muon charge ratio,

- events reconstructed in vertically aligned cells are deselected.

In addition, a possible difference between data and MC regarding the resolution of the extrapolation back to the scintillator plane, as well as different characteristics of the real and simulated scintillator noise are investigated:

- the scintillator matching fiducial volume cut, by default placed exactly on the border of a scintillator cassette, is altered by ± 5cm,

corresponding to about 2.5 σ of the backtracking resolution according to [117].
The resulting relative changes of the measured flux Φ and charge ratio R are listed in table 6.4 as a function of zenith angle. The relative change of raw data events is also shown. It ranges from 0% in case the phase space corresponding to the zenith angle bin under study is not affected by the cut up to over 100% for the P-segment variation. As can be seen, both Φ and R are remarkably stable under the cut variation. The arithmetic average over all zenith angles of the total variation obtained by adding up the individual contributions in quadrature is

$$\left(\frac{\Phi' - \Phi_0}{\Phi_0}\right)_{\text{cut}} = {}^{+0.011}_{-0.015} \qquad \text{and} \qquad \left(\frac{R' - R_0}{R_0}\right)_{\text{cut}} = {}^{+0.003}_{-0.005} \,. \tag{6.55}$$

As expected, the charge ratio is more robust with respect to the cut variation, as some of the normalization uncertainties cancel out, in case they are equal for positive and negative muons. The main contribution to the total flux change stems from the variation of the number of P-segments and the redefinition of the scintillator match fiducial areas.
Another estimate of the normalization uncertainty may be derived from the azimuth variation of the muon flux and charge ratio, which was already used above to determine the molasse overburden uncertainty. At high energies small molasse density variations

$\cos(\theta)$		χ^2/ndf 4→25	Z-hits 4→2	$\phi_{\mathrm{loc}} = 25^o$ →23 ^{o}	→27^o	no vert. cells	$f_{\mathrm{hit}}/f_{\mathrm{nom}}$ 1.5→3.0	P-seg. 6→5	scint.-match -5cm	+5cm	total	Δ_{n} (azimuth)	Δ_{y} (subsample)	Δ_Z	Δ_{D}	**max**
0.525-0.600	$\Delta N/N$	0.038	0.167	0.000	0.000	-0.056	0.025	0.599	-0.132	0.062						
	$\Delta\Phi/\Phi$	0.001	0.002	0.000	0.000	-0.001	-0.001	-0.008	-0.014	-0.033	$^{+0.002}_{-0.037}$	0.009± 0.022	0.017	0.007	0.015	**0.037**
	$\Delta R/R$	-0.001	0.000	0.000	0.000	-0.002	0.001	0.001	0.000	0.000	$^{+0.001}_{-0.003}$	0.012± 0.010	0.014	0.004	0.011	**0.014**
0.600-0.675	$\Delta N/N$	0.062	0.153	0.000	0.000	-0.160	0.020	0.632	-0.128	0.049						
	$\Delta\Phi/\Phi$	0.002	0.001	0.000	0.000	0.001	0.001	-0.011	0.008	0.004	$^{+0.009}_{-0.011}$	0.006± 0.021	0.003	0.023	0.014	**0.023**
	$\Delta R/R$	-0.001	-0.002	0.000	0.000	-0.003	0.000	-0.003	0.000	0.002	$^{+0.002}_{-0.005}$	0.014± 0.006	0.004	0.001	0.003	**0.014**
0.675-0.750	$\Delta N/N$	0.080	0.166	-0.004	0.012	-0.356	0.030	0.716	-0.136	0.035						
	$\Delta\Phi/\Phi$	0.000	0.001	0.000	0.001	0.001	0.000	-0.013	0.007	0.009	$^{+0.011}_{-0.013}$	0.007± 0.010	0.007	0.004	0.017	**0.017**
	$\Delta R/R$	-0.001	0.002	-0.001	0.000	-0.008	0.002	0.000	0.000	0.001	$^{+0.003}_{-0.008}$	0.000± 0.008	0.002	0.018	0.005	**0.018**
0.750-0.825	$\Delta N/N$	0.031	0.184	-0.073	0.122	-0.003	0.048	0.886	-0.126	0.036						
	$\Delta\Phi/\Phi$	0.002	0.000	-0.002	0.004	0.000	0.001	-0.010	0.009	0.012	$^{+0.015}_{-0.010}$	0.027± 0.004	0.002	0.009	0.015	**0.027**
	$\Delta R/R$	0.000	0.000	-0.001	-0.000	0.000	0.000	0.000	0.005	-0.001	$^{+0.005}_{-0.002}$	0.010± 0.007	0.004	0.010	0.001	**0.010**
0.825-0.900	$\Delta N/N$	0.031	0.186	-0.292	0.686	-0.017	0.086	1.052	-0.115	0.039						
	$\Delta\Phi/\Phi$	0.002	0.007	0.003	-0.002	0.000	0.000	-0.019	0.006	0.011	$^{+0.015}_{-0.020}$	0.017± 0.020	0.009	0.000	0.019	**0.020**
	$\Delta R/R$	0.001	0.000	-0.013	0.004	-0.001	0.000	0.003	0.001	0.002	$^{+0.005}_{-0.013}$	0.005± 0.004	0.002	0.011	0.007	**0.013**
0.900-0.938	$\Delta N/N$	0.032	0.224	-0.433	0.470	-0.008	0.105	0.966	-0.123	0.052						
	$\Delta\Phi/\Phi$	0.003	0.007	0.008	-0.004	0.000	0.001	-0.018	0.007	0.009	$^{+0.016}_{-0.018}$	0.024± 0.005	0.014	0.002	0.015	**0.024**
	$\Delta R/R$	-0.001	0.000	0.000	0.000	0.000	0.002	-0.004	0.002	-0.001	$^{+0.003}_{-0.004}$	0.023± 0.010	0.003	0.021	0.014	**0.023**
0.938-0.975	$\Delta N/N$	0.040	0.338	-0.008	0.287	-0.037	0.034	0.698	-0.141	0.021						
	$\Delta\Phi/\Phi$	0.002	0.007	0.000	-0.001	0.000	0.002	-0.003	0.004	0.008	$^{+0.011}_{-0.003}$	0.028± 0.003	0.018	0.004	0.007	**0.028**
	$\Delta R/R$	-0.001	0.000	0.000	0.005	-0.001	-0.002	0.002	-0.004	0.001	$^{+0.005}_{-0.004}$	0.023± 0.003	0.002	0.011	0.004	**0.023**
0.975-1.000	$\Delta N/N$	0.057	0.351	0.000	0.000	-0.134	0.040	1.058	-0.138	0.021						
	$\Delta\Phi/\Phi$	0.002	0.002	0.000	0.000	-0.001	-0.001	-0.011	0.005	0.008	$^{+0.010}_{-0.011}$	0.015± 0.002	0.017	0.003	0.002	**0.017**
	$\Delta R/R$	0.001	-0.001	0.000	0.000	0.000	0.001	0.001	-0.001	0.001	$^{+0.002}_{-0.002}$	0.015± 0.003	0.008	0.012	0.011	**0.015**

Tab. 6.4: *Relative changes of the number of selected data events N and fully corrected muon flux Φ and charge ratio R for different selection cuts at surface energies between 100 and 200 GeV. The normalization uncertainties as obtained from the azimuth and subsample analysis are also shown. In the last column, the estimated total error is listed.*

have only negligible influence on the relative energy loss. Therefore any variation of the measured flux with the azimuth angle can be addressed to differences between the simulated and the real detector, as for a given zenith angle different azimuth angles also correspond to different detector regions. The asymptotic relative flux changes Δ_n values as obtained in the fit according to equation (6.51) are listed in of table 6.4. On average relative differences of

$$\left(\frac{\Phi' - \Phi_0}{\Phi_0}\right)_{\varphi} = 0.017 \pm 0.005 \qquad \text{and} \qquad \left(\frac{R' - R_0}{R_0}\right)_{\varphi} = 0.013 \pm 0.002 \tag{6.56}$$

are estimated. For the muon flux, the azimuth and cut variation analysis yield the same result within the errors. For the charge ratio however, a significantly larger normalization uncertainty is obtained by the cut variation. Using part of the MC events as 'data' it has been checked that in the absence of normalization errors a relative difference compatible with zero is obtained, proofing that the errors in equation (6.50) are calculated correctly.

Finally, the flux and charge ratio differences of the data subsamples provide another check of the normalization. The errors obtained from the three data subdivisions are listed in the second last column of table 6.4. As can be seen, in the direction close to vertical, the largest flux differences are observed between the two data taking years, whereas for more horizontal muons the difference between the inner and outer detector volume is the dominating error source. Averaging the maximum of the three subsample contributions over the zenith angle yields the following mean uncertainties:

$$\left(\frac{\Phi' - \Phi_0}{\Phi_0}\right)_{\text{sub}} = 0.018 \qquad \text{and} \qquad \left(\frac{R' - R_0}{R_0}\right)_{\text{sub}} = 0.013\,. \tag{6.57}$$

Given the fact, that all of the above methods are just different ways of estimating the same uncertainty, the results are not added together, but rather the respective maximum value is used to estimated the normalization uncertainty, as indicated in the last column of 6.4.

6.4.3 Detector matrix uncertainty

The available MC statistics limit the precision of the detector matrix **D**. Below 200 GeV they dominate the total statistical error in the denominator of (6.13) contributing about 0.5% to the total error per zenith angle bin.

The minimization according to equation (6.13) is repeated with a momentum resolution altered by ± 8%, corresponding to its uncertainty estimated in section 5.2.3. As can

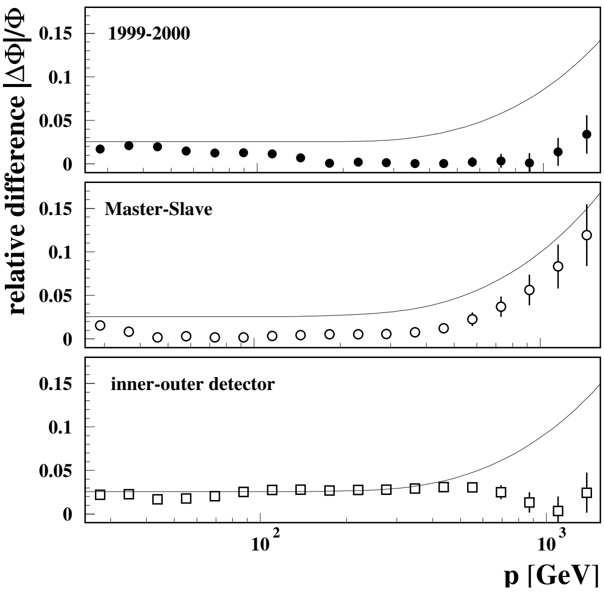

Fig. 6.15: *Muon flux difference between data subsamples averaged over the zenith angle. The line shows the expected uncertainty composed of the normalization uncertainty, the alignment error and the momentum resolution uncertainty.*

be seen in 6.16(a), the observed relative flux change $\Delta_\mathbf{R}$ is well described by

$$\Delta_\mathbf{R} \approx \begin{cases} a_r \cdot (p - 0.2\,\mathrm{TeV}), & p \geq 200 \text{ GeV} \\ 0, & p < 200 \text{ GeV} \end{cases} \tag{6.58}$$

with $a_r = 0.03\,\mathrm{TeV}^{-1}$. As the detector resolution affects both muon charges the same way, the corresponding charge ratio change is much smaller. It stays below 1% up to 1 TeV and is thus negligible compared to the systematic error due to the alignment of the muon detector. The behavior of the subsample muon flux difference at high energies is shown in figure 6.15. As can be seen, both the different data taking years and the spectra from the inner and outer detector show a remarkably good agreement in the shape of the muon spectrum. The spectrum differences of the detector halfs along the z-direction however exhibit a much faster rise as expected from the alignment and resolution errors together. In order to account for this observation, a systematic resolution parameter of

$$a_r \leq 0.06\,\mathrm{TeV}^{-1} \tag{6.59}$$

will be assumed.

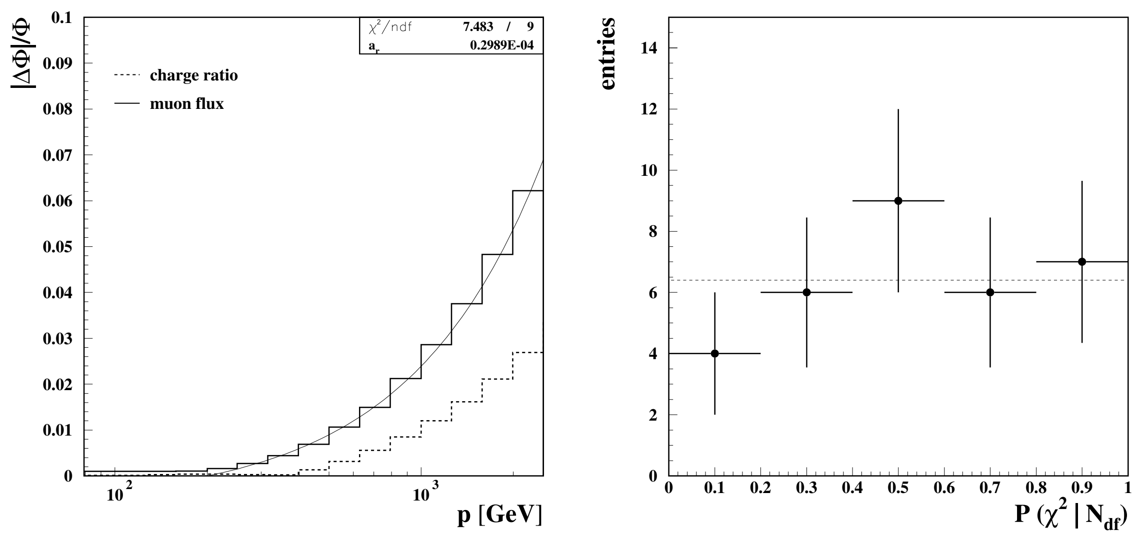

(a) *Relative uncertainty of the muon flux and charge ratio due to the uncertainty of the momentum resolution. The line shows the parameterization of the flux uncertainty.*

(b) *Probability distribution of the flux fit χ^2. The dashed line indicates the expected distribution.*

Fig. 6.16: *Uncertainties due to the momentum resolution and fitting function.*

6.4.4 Fit function bias

The choice of the fit function (6.11) may introduce a bias, if it does not describe the actual momentum dependence of the muon spectrum. The probability distribution of the fitting χ^2 after the minimization of equation (6.13) is shown in figure 6.16(b) for 32 independent spectra (8 zenith angle bins, two data taking years and two detector halfs). The observed probabilities agree very well with the expected flat distribution, therefore no additional systematic error is assumed.

6.4.5 Long term stability and atmospheric effects

So far, the long term stability of the measured flux was only tested by the 1999/2000 data subdivision. For a more detailed monitoring of the L3+C rates, the influence of atmospheric effects needs to be separated from the possible detector related efficiency changes.
Theoretical predictions [29, 121] as well as experimental observations [17] suggest a positive correlation of the muon rate at high energies with the temperature of the upper

layers of the atmosphere. In the framework of the analytic approximation discussed in chapter 2, this can be understood as the expansion of the isothermal atmosphere (2.5). For larger atmospheric scale heights h_0, also the critical energies in equation (2.19) increase, because the mesons are produced in thinner regions of the atmosphere and thus they have more time to decay to a muon before they interact.
At low energies, the h_0 dependence of the mean production height in equation (2.23) should lead to a negative correlation due to an increased probability for the muon decay. Ignoring the small kaon contribution to the muon flux, a linear expansion of the analytic muon flux formula (2.33) multiplied with the muon decay term (2.24) leads to the following expected relative flux change:

$$\frac{\Phi(h_0) - \Phi(\langle h_0 \rangle)}{\Phi(\langle h_0 \rangle)} = \frac{h_0 - \langle h_0 \rangle}{\langle h_0 \rangle} \cdot (\alpha_\mu^{\rm dec} + \alpha_\pi^{\rm dec}) \tag{6.60}$$

with

$$\alpha_\mu^{\rm dec} = -\frac{m_\mu \langle h \rangle}{E \cos\theta \, x_\mu} \tag{6.61}$$

and

$$\alpha_\pi^{\rm dec} = \left(\frac{B_{\mu\pi}}{E\cos\theta} + 1 \right)^{-1} , \tag{6.62}$$

where $x_\mu = 659$ m and $B_{\mu\pi} = 110$ GeV. Similar relations can be derived for the flux change induced by the energy loss change with X_0, i. e. the ground level pressure, which are however small at L3+C energies and for the pressure changes during the data taking.
Data from meteorological balloon flights [76, 77, 125] flown one to four times each day 100 km away from the detector are fitted with the isothermal model (2.6) at high altitudes yielding an average scale height of 6.34 km with a root mean square of 1.3%. The latter constitutes an estimate of the expected rate changes caused by the atmospheric effect for high energies where the positive correlation is at maximum ($\alpha_\mu^{\rm dec} + \alpha_\pi^{\rm dec} \to 1$). Unfortunately, the real atmosphere is far from being isothermal, and a considerable bias might be introduced by the above approximations. Up to the heights of 30 km, corresponding to about the maximum height the balloons can reach, the pressure dependence is well described by the parameterization of [109]:

$$X(h)/\mathrm{gcm}^{-2} = \begin{cases} A(h_b - h/\mathrm{km})^{(\alpha+1)}, & h \le h_t \\ Be^{-\frac{h}{h_0}}, & h > h_t \end{cases} \tag{6.63}$$

Using this ansatz, the balloon data averaged over two weeks are fitted and the observed L3+C rate changes are compared to the output of an air shower simulation with the `TARGET` program for the corresponding atmospheric parameters. An example of the

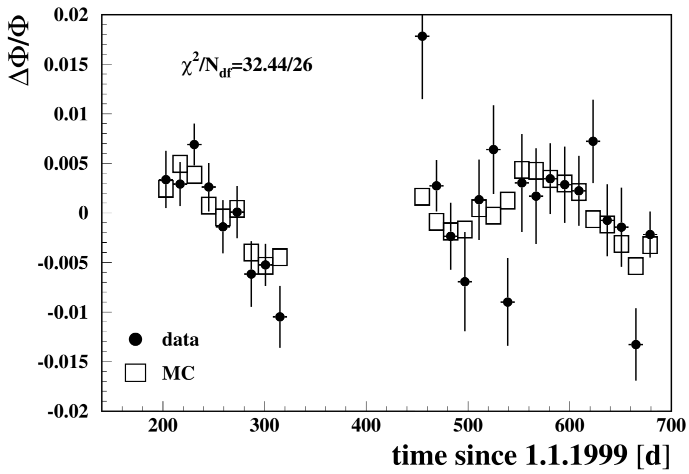

Fig. 6.17: *Relative rate change vs. time at from 50 to 62 GeV compared to a prediction of the atmospheric effect with the* **TARGET** *air shower simulation. The value of a χ^2 comparison of data and MC is also shown.*

predicted and observed rate changes is shown in figure 6.17 for the momentum bin from 50 to 62 GeV and zenith angles < 32 degrees. The data were averaged for each data taking year separately. A good correlation between the simulation and the data can be seen. The full comparison to the rates in 26 weeks and 14 momentum bins yields a χ^2/N_{df} of 526/364. This large value can be either attributed to data instabilities not corrected for in the acceptance calculation or an incomplete modeling of the atmosphere. An additional systematic error of 0.3% is needed to reach $\chi^2/N_{\mathrm{df}} = 364/364$. Conservatively, the full 0.3% will be regarded as the systematic uncertainty of the L3+C data stability and added in quadrature to the normalization uncertainty.

6.4.6 Total uncertainty

The total systematic uncertainty of each zenith angle measurement is calculated by adding all the above uncertainties in quadrature.
The momentum scale uncertainties are translated to a muon flux uncertainty according to equation (6.42). Together with the normalization uncertainties Δ_{n} and the momentum resolution uncertainty Δ_{R}, six sets of new parameters a'_m are obtained by repeating the muon flux fit of equation (6.13) with the shifted spectra. These parameters are

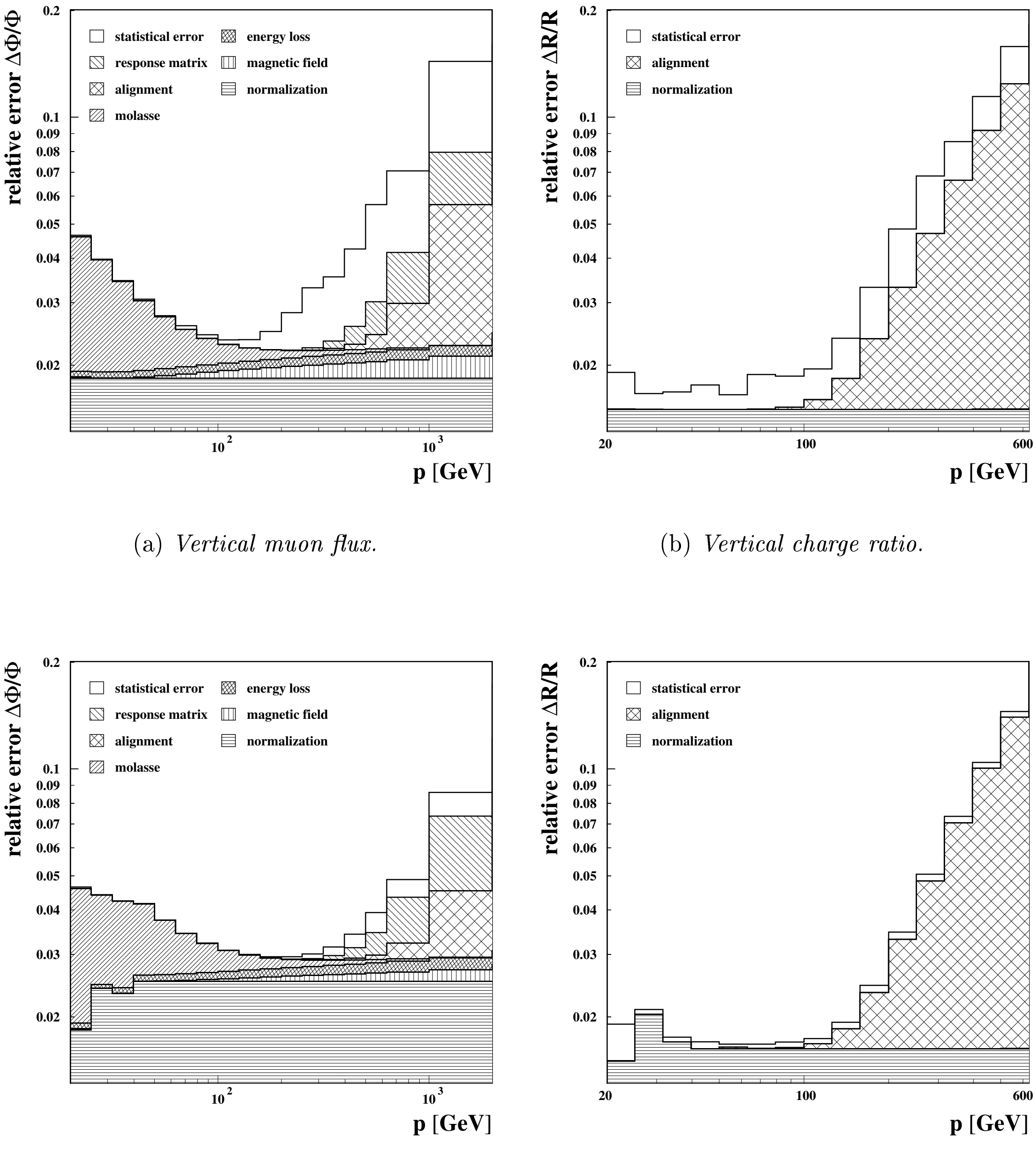

(a) *Vertical muon flux.* (b) *Vertical charge ratio.*

(c) *Average muon flux.* (d) *Average charge ratio.*

Fig. 6.18: *Contributions to the systematic uncertainties of the muon flux and charge ratio as a function of surface momentum. The individual components were subsequently added in quadrature. The uncorrelated statistical errors according to equation (6.20) are also shown.*

used to construct the total systematic covariance matrix of the parameters a_m:

$$V_{mn}^{\rm sys} = \sum_{k=1}^{6} (a_m - a'_{mk})(a_n - a'_{nk}) \ . \tag{6.64}$$

The obtained covariance matrices can be found in the appendix.
The corresponding total uncertainties of the vertical muon flux and charge ratio are shown in figures 6.18(a) and (b) along with the uncorrelated statistical error according to equation (6.20). The muon flux uncertainty is dominated by the uncertainties of the molasse overburden at low energies and by the statistical error at high momenta. The minimal uncertainty is 2.4% around 100 GeV. The vertical charge ratio uncertainty is below 2% up to momenta of 100 GeV. Above this momentum, it rapidly rises as the alignment uncertainties gain importance.
The uncertainties averaged over the full zenith angle acceptance is shown in figures 6.18(a) and (d). Conservatively, the systematic errors are assumed to be fully correlated in between the zenith angles and are thus averaged arithmetically, whereas of course the independent statistical errors are diminished considerably by the averaging process, as they are added in quadrature. As can be seen, the full data set is therefore not limited by the statistical error, but the systematic errors of the flux measurement dominate over the full momentum range. Due to the larger amount of molasse in comparison to the vertical measurement, the minimum of the muon flux error occurs at sightly higher energies around 200 GeV where it is 3.0%. Despite the first momentum interval, where only the vertical direction contributes, the charge ratio error is also dominated by systematics over the full momentum range. The minimum error is 1.6% at around 60 GeV.

6.5 Muons from Z^0 decays

The location of the L3+C experiment at a particle accelerator provides the unique possibility to cross-check the understanding of the detector acceptance and efficiencies: Even during the high energy LEP runs in 1999 and 2000, the accelerator was providing data for calibration purpose at center of mass energies around the mass of the Z^0 boson of about 91 GeV. At this energy the cross section for producing a muon pair via

$$e^+e^- \to Z^0 \to \mu^+\mu^- \tag{6.65}$$

is maximal. This process was precisely measured by the four LEP experiments during the high statistics low energy LEP runs in the 1990'ies, therefore L3+C can validate its ability to measure the absolute muon flux by extracting the absolute dimuon cross section $\sigma_{\mu^+\mu^-}$ from the data collected during the LEP calibration fills. The principle of this measurement is quite similar to the measurement of the muon flux Φ_μ:

$$\Phi_\mu \propto \frac{N_\mu}{\varepsilon\tau} \qquad \leftrightarrow \qquad \sigma_{\mu^+\mu^-} \propto \frac{N_{\mu^+\mu^-}}{\varepsilon L}\,. \tag{6.66}$$

Here the role of the livetime τ is replaced by the time integrated luminosity L, which contains the dependence of the number of produced dimuon pairs on the beam characteristics, i. e. the delivered particle collisions, and the effective running time. Both measurements need to determine the absolute number of events and therefore the detector efficiency ε appears in the denominator.

Data preselection

To be able to reduce the number of background atmospheric muons for this special analysis, the L3 common stop signal, sent after each beam crossing to the L3 TDC's, was fed into the L3+C DAQ system since the end of 1999. As it was shown in a pilot study [106], the time difference between this beam crossing related signal and the muon scintillator time measured in L3+C can be used to preselect muons originating from the accelerator after correcting for a constant time offset of approximately 1.5 µs caused by delays in the electronics and cables. A preselection gate of ± 80 ns is chosen, which reduces the number of events from the $7{\cdot}10^7$ cosmic class 1 triggers collected during the year 2000 LEP calibration runs to $1.3{\cdot}10^6$ Z^0 event candidates.
The efficiency of this preselection is influenced by the functionality of the TDC chip used in L3+C to measure the L3 common stop signal. Its efficiency is studied on a

run by run basis by comparing the number of signals from the scintillator CPC, which are measured by the same chip, to the expected number derived from the CTT trigger decision. On average, a chip efficiency of 87.52±0.01% is found.

Determination of the luminosity

Since in practice the derivation of the luminosity from the particle accelerators' beam parameters introduces large uncertainties, it is usually determined by counting the number of produced events of a process with a known cross section. L3 uses low angle Bhabha scattering $e^+e^- \to e^+e^-$, which is a theoretically well understood process. At $z = \pm 2.73$ m away from the interaction point two electromagnetic calorimeters for the identification of electrons are placed covering a polar angular range of 24.7 mrad $< \theta <$ 69.3 mrad. Given the acceptance and efficiencies of these detectors, the number of identified electrons can be converted to the luminosity with a precision better than 0.1% [40] using the theoretical prediction of the Bhabha scattering cross section.
L3+C does not read out the L3 luminosity monitors, therefore the luminosity has to be derived from the L3 data:

$$L_{\mathrm{L3+C}} = L_{\mathrm{L3}}\, \frac{N_{\mathrm{1Hz}}}{t_{\mathrm{L3}}/s}\,. \tag{6.67}$$

Here $L_{\mathrm{L3+C}}$ and L_{L3} denote the L3+C and L3 luminosities respectively. N_{1Hz} is the number of 1Hz trigger recorded in L3+C during the time t_{L3} when L3 was recording data from the LEP calibration runs. The common stop preselection signals are only sent, if L3 is active. Therefore the L3 DAQ efficiency, included in L_{L3}, needs not to be corrected for.
In the year 2000, LEP delivered a luminosity of about 4380 nb^{-1} at energies around the Z^0-mass. L3 recorded data corresponding to 4054±9 nb^{-1} out of which 3583±13 nb^{-1} was received by L3+C. After application of the run quality criteria, 3020±12 nb^{-1} remain for the analysis. The quoted errors include the statistical error due to the number of selected Bhabha events for L3 and in addition the statistical error from the number of 1Hz triggers for L3+C. The luminosity weighted LEP center of mass energy was 91.27 GeV with a spread of 0.02 GeV.

Z^0 data reconstruction and event simulation

The preselected Z^0 candidate data needed to be reconstructed with slight modifications to the standard reconstruction algorithm: Muons originating from the center of

the detector need about 30 ns to reach the scintillator and to produce a $t0$-hit there, whereas atmospheric muons pass the scintillators before they reach the drift chambers. Therefore a different time of flight correction is applied to the drift times of the preselected sample.
A special MC set was produced using standard event generators to simulate the expected signal events and also e^+e^- reactions which could mimic the process (6.65) as listed in the table below.

process	number of events	generator
$e^+e^- \rightarrow \mu^+\mu^-$	$2 \cdot 10^6$	KORALZ [86]
$e^+e^- \rightarrow \tau^+\tau^-$	$4 \cdot 10^5$	KORALZ
$e^+e^- \rightarrow q\bar{q}$	$2 \cdot 10^6$	PYTHIA [126]
$e^+e^- \rightarrow e^+e^-\mu^+\mu^-$	$3 \cdot 10^6$	LEP4F [136]

Tab. 6.5: *Simulated signal and background processes.*

$\mathbf{Z^0}$ Data analysis

The Z^0 analysis uses the same* selection cuts as used in the default spectrum selection, because the aim of this study is to verify the acceptance calculation.
In addition to the usual analysis procedure the following cuts are imposed to reduce the background from atmospheric muons:

- **vertex origin:** The estimated distance of closest approach (dca) to the center of the detector should be smaller than 9 cm.

- **time difference to scintillator hit:** The time difference Δt of the selected scintillator hit to the L3 common stop signal should be within -15 ns $< \Delta t <$ 10 ns. The asymmetric cut is chosen to avoid missing events with a large photo multiplier time slewing. Events outside this window are used to estimate the contamination due to atmospheric muons.

- **energy:** The energy of the muon should be at least 60% of half of the center of mass energy.

*Cuts specific to the atmospheric muon data, as the shaft-deselection and double octant fit requirement are of course not applied.

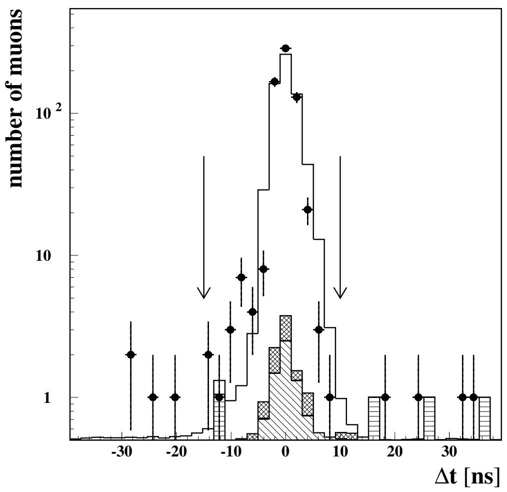

(a) time difference

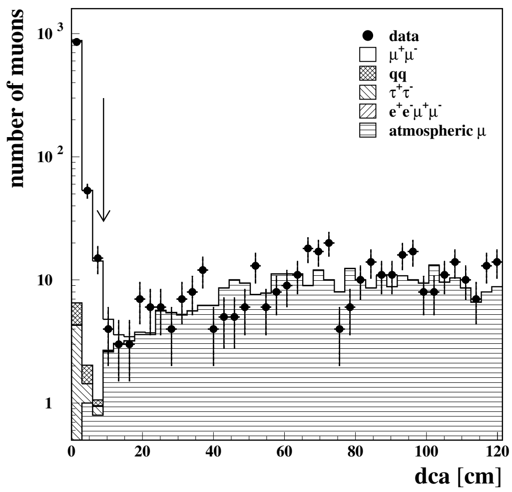

(b) distance of closest approach

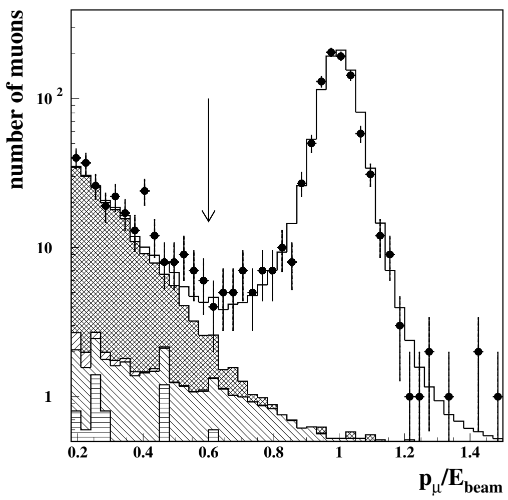

(c) muon energy

Fig. 6.19: *The three Z^0 selection cuts (indicated by the arrow) for single and double selected events. The displayed MC distributions are normalized to L3+C luminosity using the Standard Model cross sections and scaled according to the determined selection efficiency corrections.*

	$\mathbf{N}^{\text{data}}$	$\mathbf{N}^{\text{cos}}$	$\mathbf{N}^{\text{bkg}}$	$\mathbf{N}^{\mu^+\mu^-}$
N_1	494	1.8 $\pm$0.6	7.0 $\pm$ 0.4	512.4 $\pm$ 1.0
N_2	431	0.4 $\pm$0.3	0.6 $\pm$ 0.2	452.7 $\pm$ 0.9
N_{12}	291	0	0.01 $\pm$ 0.01	315.3 $\pm$ 0.8

Tab. 6.6: *Number selected data and MC events.*

The event distributions after releasing one of these cuts are shown in figure 6.19. Whereas the first two selections reject most of the atmospheric muon background, the cut on the muon energy reduces the background from other processes than (6.65), leaving the final sample almost background free.

The selection efficiency corrections calculated in section 6.3.1 can not be applied directly to the Z^0 sample, as the muons produced in e^+e^- annihilations traverse different detector regions than atmospheric muons. Instead, the following system of equations is solved taking into account the statistical errors and their correlations:

$$\begin{aligned} N_1^{\text{data}} &= N_1^{\text{cos}} + (N_1^{\text{bkg}} + N_1^{\mu^+\mu^-} \cdot a)\, \varepsilon_1 \\ N_2^{\text{data}} &= N_2^{\text{cos}} + (N_2^{\text{bkg}} + N_2^{\mu^+\mu^-} \cdot a)\, \varepsilon_2 \\ N_{12}^{\text{data}} &= N_{12}^{\text{cos}} + (N_{12}^{\text{bkg}} + N_{12}^{\mu^+\mu^-} \cdot a)\, \varepsilon_1\varepsilon_2 \end{aligned} \tag{6.68}$$

Here N_1 and N_2 denote the number events which passed the selection criteria in detector hemisphere 1 or 2 and N_{12} events with two selected tracks in the upper and lower hemisphere of the detector respectively. It should be noted, that these numbers are not independent, i.e. the total number of selected events is not $N_1 + N_2 + N_{12}$ but rather $N_1 + N_2 - N_{12}$, because the double selected events are a subsample of both N_1 and N_2. N^{cos} stands for the estimated number of selected atmospheric muons and N^{bgk} denotes the MC prediction of background hadronic, tau and four fermion events. The MC signal expectation for dimuon Z^0 events is $N_{12}^{\mu^+\mu^-}$. The selected MC events are normalized to the L3+C luminosity

$$N^{\text{MC,i}} = \sigma_i^{\text{SM}} \left(\frac{n_{\text{sel}}^{\text{MC,i}}}{n_{\text{gen}}^{\text{MC,i}}} \right) L_{\text{L3+C}}\, \varepsilon_{\text{ps}} \tag{6.69}$$

using the relevant Standard Model cross sections σ_i^{SM}, which were calculated with the `ZFITTER` program [27]. Furthermore, the measured preselection efficiency ε_{ps} is corrected for. The corresponding event numbers are listed in table 6.6.

Finally, the three unknown parameters are the two selection efficiency corrections ε_1

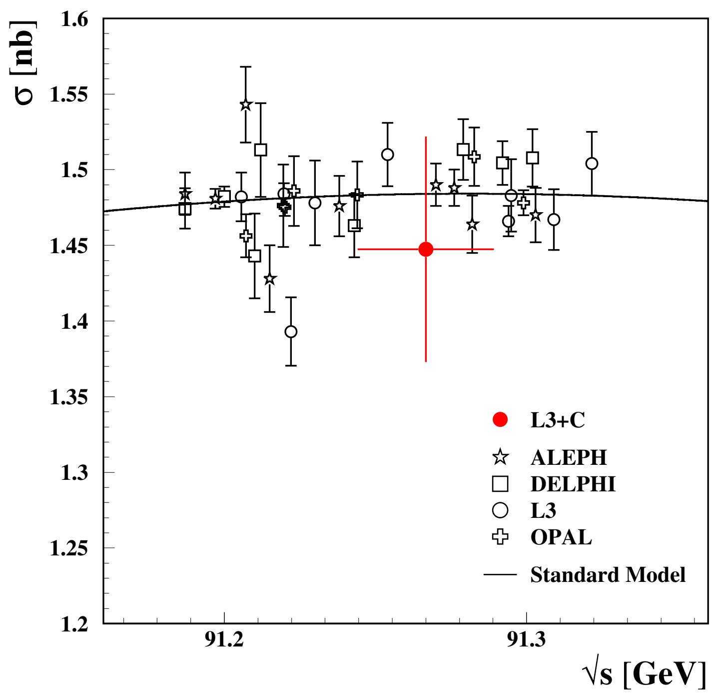

Fig. 6.20: Comparison of the L3+C dimuon cross section result with the LEP precision measurements [1–5, 26] and the Standard Model prediction. The data of [3] was corrected to the full kinematic and geometric acceptance using `KORALZ`.

and ε_1 and the MC normalization factor a,

$$a = \frac{\sigma^{\mathrm{L3+C}}_{\mu^+\mu^-}}{\sigma^{\mathrm{SM}}_{\mu^+\mu^-}}, \tag{6.70}$$

which is the ratio of the cross section $\sigma^{\mathrm{L3+C}}_{\mu^+\mu^-}$ derived with the L3+C detector to its Standard Model prediction.

$\mathbf{Z^0}$ results

Solving (6.69), the following cross section for the process $e^+e^- \to Z^0 \to \mu^+\mu^-$ is obtained:

$$\sigma^{\mathrm{L3+C}}_{\mu^+\mu^-} = 1.447 \pm 0.071\ (\mathrm{stat.}) \pm 0.021\ (\mathrm{syst.})\ \mathrm{nb}\,. \tag{6.71}$$

The stated systematic error includes only errors which are *not* relevant for the spectrum analysis. This is the statistical error of the luminosity corresponding to 0.006 nb and the error due to the additional Z^0 selection cuts. The latter is estimated to be 0.020 nb

cut value	cross section [nb]
dca < 18cm	1.430±0.071
-40ns < Δt < 40ns	1.467±0.072
$E/E_{\mathrm{beam}} > 70\%$	1.449±0.073
$E/E_{\mathrm{beam}} > 50\%$	1.452±0.072

Tab. 6.7: *Cross sections obtained with different preselection cuts.*

by varying the selection cuts as indicated in table 6.7. A subdivision of the data sample in six samples of approximately equal luminosities revealed no further systematic errors (see table 6.8).

LEP fill range	L3+C luminosity [nb^{-1}]	$\varepsilon_{\mathrm{ps}}$	cross section [nb]
6811-6821	458.9±5.1	0.891	1.41±0.19
6827-6831	558.1±5.1	0.855	1.31±0.18
6834-6842	557.2±5.3	0.841	1.50±0.17
6846-6847	420.4±4.6	0.957	1.52±0.18
7249-8176	447.4±4.5	0.854	1.33±0.17
8177-8454	578.3±4.8	0.869	1.61±0.19

Tab. 6.8: *Cross sections obtained for different data taking periods. The comparison to the Standard Models expectation (6.72) yields* $\chi^2/Ndof = 2.6/6$.

This measured cross section is in good agreement with the LEP precision measurements (see figure 6.20) and to the Standard Model prediction of

$$\sigma^{\mathrm{SM}}_{\mu^+\mu^-} = 1.4840 \pm 0.0013\,\mathrm{nb}\,. \tag{6.72}$$

The small error is due to the experimental errors [75] of the input parameters of the `ZFITTER` program.

The obtained selection efficiencies read as $\varepsilon_1 = 0.969 \pm 0.032$ and $\varepsilon_2 = 0.972 \pm 0.044$. Recalling that the average selection efficiency correction in the year 2000 was found to be 0.877 in section 6.3.1, the determined parameters $(\varepsilon_1, \varepsilon_2, a)$ can be compared to the expectation of $(\sqrt{0.877}, \sqrt{0.877}, 1)$. Taking into account the correlations between ε_1, ε_2 and a, a χ^2 comparison to this expectation yields a χ^2/ndf of 1.3/3 and it can be concluded that the selection efficiencies obtained in the Z^0 analysis are in good agreement to the ones used for the spectrum calculation.

Thus, with this study the normalization of L3+C could be verified within 5%. Although this number is much larger than the estimated systematic uncertainty of the muon flux normalization, it provides an absolute systematic cross-check qualitatively different from the relative comparisons of the previous section.

6.6 Results

6.6.1 The atmospheric muon flux as function of momentum, charge and zenith angle

The angular acceptance of the experiment is limited by the scintillator coverage of the detector, which allows to measure muons with zenith angles down to 58^o. At low energies, due the shielding of the molasse overburden, the starting momenta range from 20 to 40 GeV, depending on the zenith angle bin under study. At high energies the muon flux is measured up to 2000 GeV and the charge ratio up to 630 GeV. Above these values the total errors on Φ and R exceed 20%, as shown in the previous section.

The fitted muon flux parameters **a** of the function (6.11) are listed in the appendix along with their statistical and systematic covariance matrices. The measured muon spectra are displayed in figures 6.21 and 6.22 on the next two pages. Both the uncorrelated data points derived according to equation (6.18) and the smooth fitted functions (6.11) are shown. Naturally, the total error calculated for the latter is much smaller at high energies, as the number of free parameters is only eight in this case, which reduces the statistical uncertainty considerably.
For better visibility, the steep muon flux distributions were multiplied with the mean momentum momentum to the third power. Following the suggestion from [99], the mean momentum $\langle p \rangle$ inside a momentum bin $[p_1, p_2]$ is determined by solving

$$\Phi(\langle p \rangle) = \frac{1}{p_2 - p_1} \int_{p_1}^{p_2} \Phi(p)\, dp\ . \tag{6.73}$$

As can be seen, in this representation the maximum of $\langle p \rangle^3 \cdot \Phi$ is shifted towards higher momenta with increasing zenith angles. This is due to the fact, that vertical muons have shorter path lengths for reaching the detector and therefore their decay probability and energy loss in the atmosphere is smaller. The overall flux at maximum grows with the zenith angle, as the muons' parent mesons have longer path lengths in the thin regions of the upper atmosphere and correspondingly a higher probability to decay to a muon neutrino pair before they interact.
It is worthwhile noting that neither a correction for the detector altitude nor the atmospheric conditions was applied to the measured muon flux data in order to avoid additional theoretical uncertainties. Instead, the L3+C detector height of 449 m above sea level and the average atmospheric profile as measured in the balloon flights close to L3+C can be used to correct the presented fluxes to arbitrary altitudes and atmo-

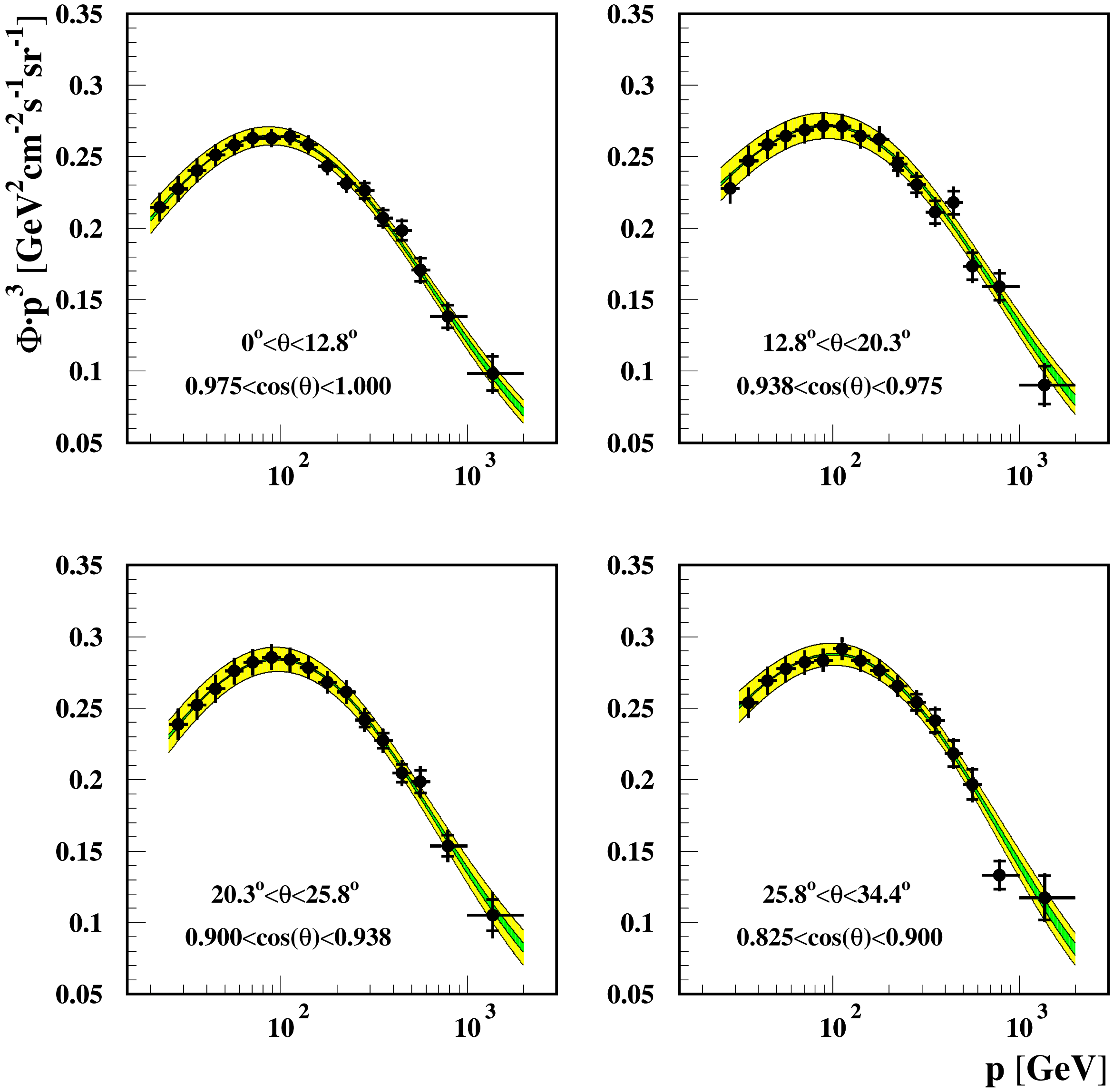

Fig. 6.21: *The measured muon spectrum for zenith angles from 0° to 34.4°. The inner error bars and dark areas denote the statistical error, the full error bar and light areas show the total error. The shaded areas correspond to the fitted function (6.11), the dots show the data points as derived with equation (6.18).*

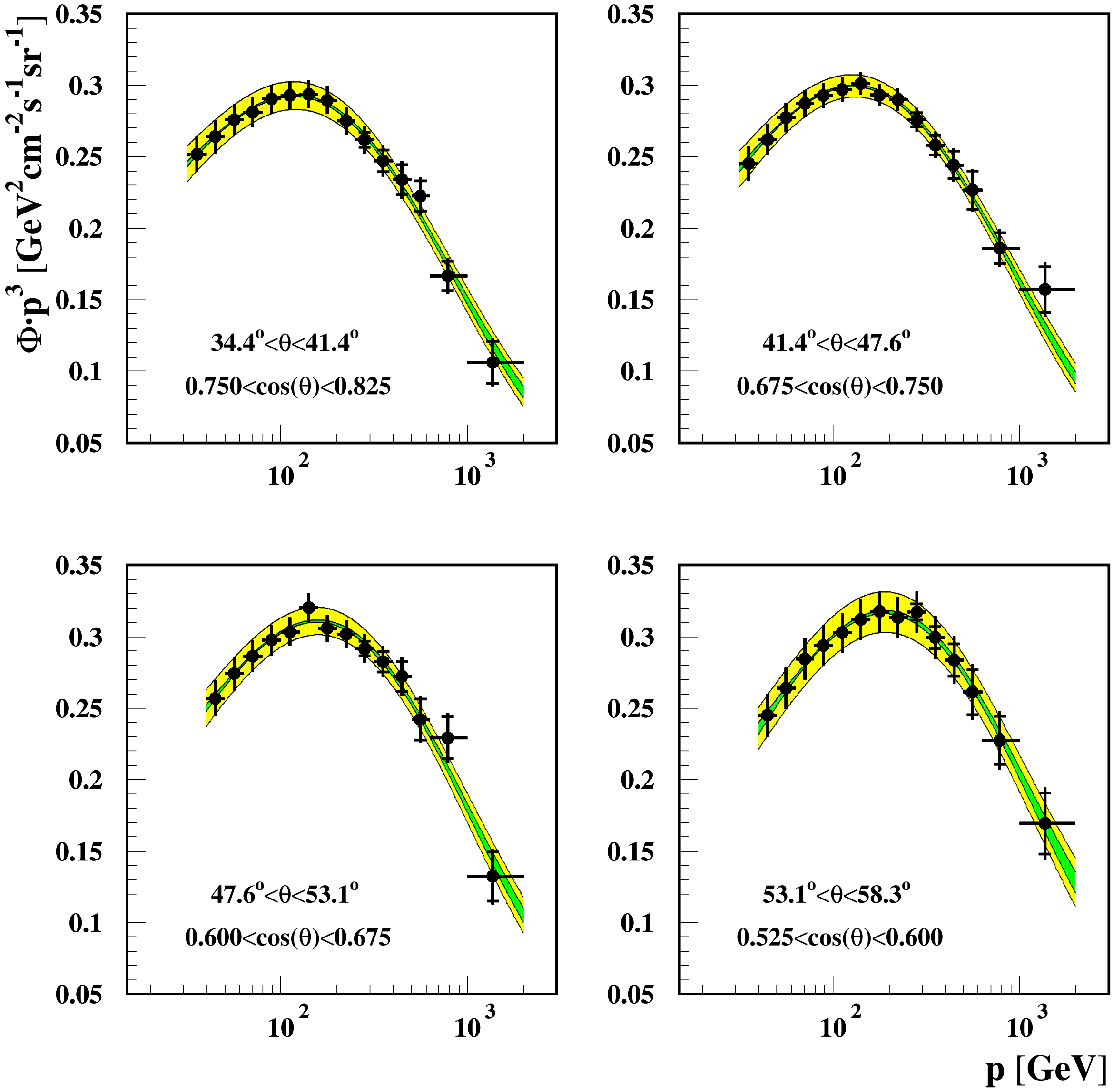

Fig. 6.22: *The measured muon spectrum for zenith angles from 34.4° to 58.3°. The inner error bars and dark areas denote the statistical error, the full error bar and light areas show the total error. The shaded areas correspond to the fitted function (6.11), the dots show the data points as derived with equation (6.18).*

spheric conditions given a certain theoretical muon flux model. The live-time weighted balloon data yield the following parameters for the atmosphere parameterization according to equation (6.63): $A = 8.078 \cdot 10^{-5}$, $B = 1332$, $h_b = 39.17$, $h_0 = 6.370$ km, and $\alpha = 3.461$, with $h_t = 11$ km.

The measured charge ratios are presented in figures 6.23 and 6.24. Within the errors, no dependence on the zenith angle or momentum is observed. Assuming uncorrelated alignment errors between zenith angle bins not sharing the same octants leads to a ratio of the average charge ratios at 110 and 550 GeV of

$$\frac{R_{550}}{R_{110}} = 1.16 \pm 0.01(\text{stat.}) \pm 0.15(\text{sys.}) \tag{6.74}$$

for the fitted flux functions and

$$\frac{R_{550}}{R_{110}} = 1.11 \pm 0.05(\text{stat.}) \pm 0.15(\text{sys.}) \tag{6.75}$$

for the unconstrained data points, which is both compatible with 1.
In the vertical direction, a mean charge ratio of

$$R_{\text{vert}} = 1.287 \pm 0.004(\text{stat.}) \pm 0.014(\text{sys.}) \tag{6.76}$$

is calculated for the uncorrelated data points with a $\chi^2/\text{Ndf} = 16.6/17$. Averaging further over the zenith angles, the charge ratio of the full data sample was found to be

$$\langle R \rangle = 1.277 \pm 0.002(\text{stat.}) \pm 0.011(\text{sys.})\ . \tag{6.77}$$

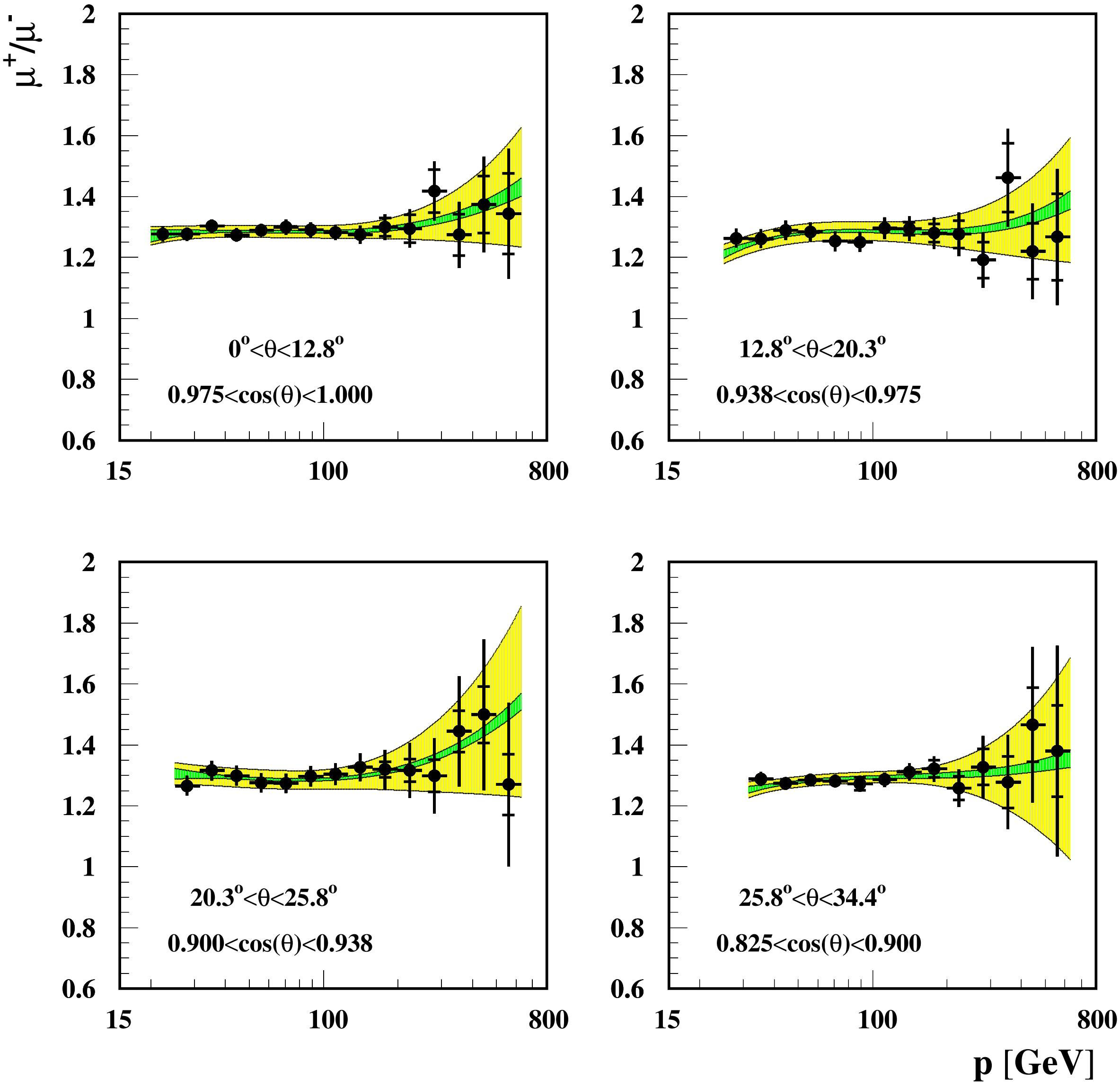

Fig. 6.23: *The measured muon charge ratio for zenith angles from 0° to 34.4°. The inner error bars and dark areas denote the statistical error, the full error bar and light areas show the total error. The shaded areas correspond to the fitted function (6.11), the dots show the data points as derived with equation (6.18).*

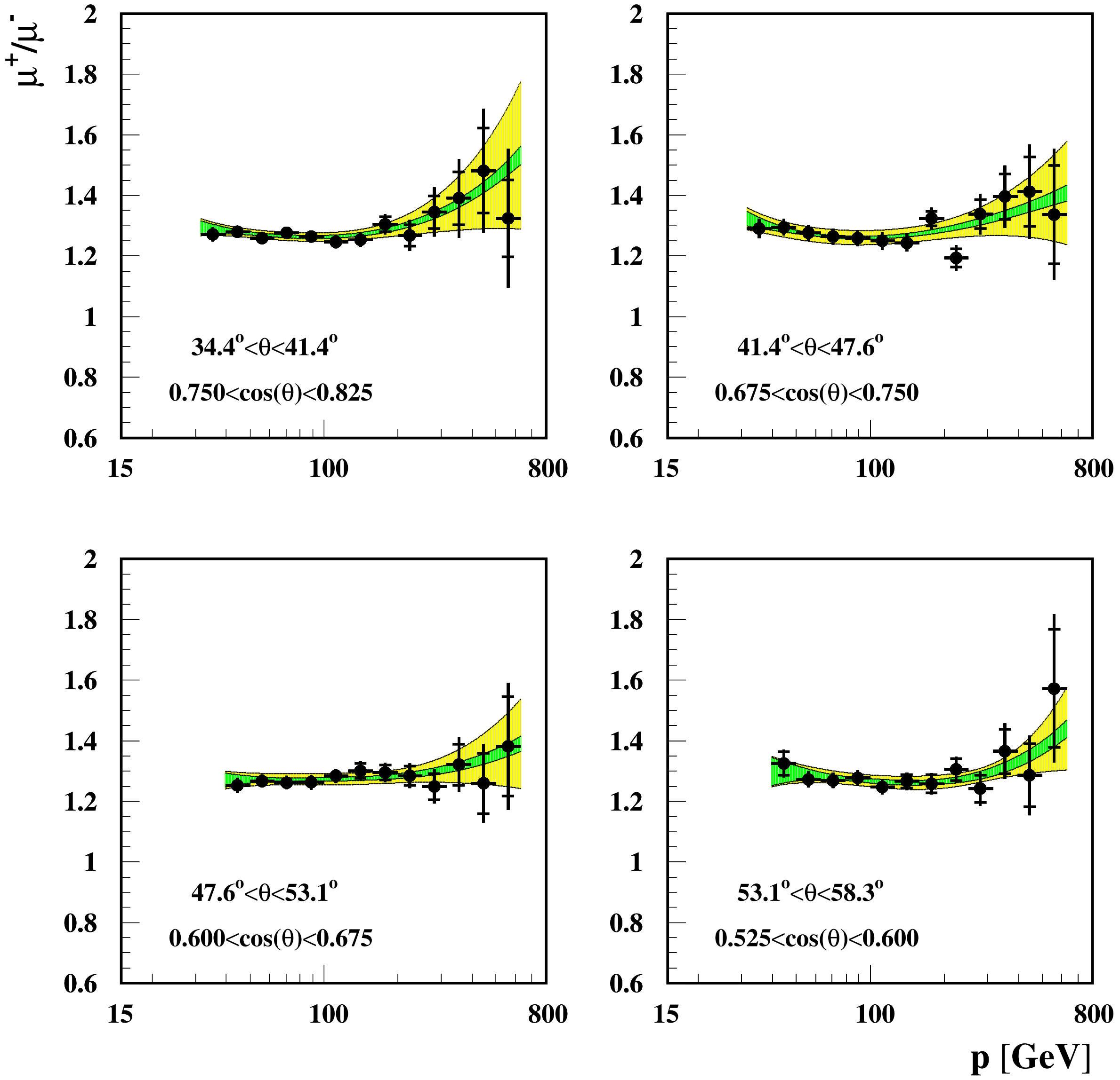

Fig. 6.24: *The measured muon charge ratio for zenith angles from 34.4° to 58.3°. The inner error bars and dark areas denote the statistical error, the full error bar and light areas show the total error. The shaded areas correspond to the fitted function (6.11), the dots show the data points as derived with equation (6.18).*

6.6.2 Comparison to previous L3+C results

Two L3 studies of the atmospheric muon spectrum were preceeding this analysis:
The pilot work from [111] was using a small data set, which was taken in 1991 during special calibration runs, when the L3 detector was triggering on atmospheric muons. The major aim of [111] was to proof the feasibility of the L3+C project. The small exposure and large systematic errors related to the muon track reconstruction and the absence of a dedicated readout system for the measurement of atmospheric muons did not allow for a precise flux measurement. At 100 GeV, a total error of 13% was achieved in the vertical direction.
The data recorded by L3+C in 1999 were already analyzed in [117] using the algorithm of [51] to deconvolute the raw detector rates to a surface spectrum and the identical muon chamber and scintillator efficiencies introduced in chapter 5 for the acceptance calculation. The major improvements of the work presented here with respect to these intermediate results can be summarized as follows:

- The complete data from the years 1999 and 2000 were analyzed here. In addition to the obvious increase of the total exposure and the related smaller statistical errors, this allowed for a stringent check of the time dependence of the detector performance.

- Due to the improved momentum reconstruction, the maximum detectable momentum of the detector was increased by about a factor four with respect to the weighted single octant average used in [117] and correspondingly a smaller correction is needed here to correct the measured high energetic muon flux (cf. figure 5.9).

- The MC model of the detector was revised for this analysis concerning the generation of the drift chamber hits and the delta ray production above and in the detector. In addition, fiducial volume cuts were introduced to exclude detector regions with a poor agreement between data and MC. As a result, the selection efficiency corrections according to equation (6.34) are smaller here. In section 6.3.1, the asymptotic selection efficiency correction were found to be 0.897 for 1999, whereas they amount to about 0.77 in [117].

- A more thorough evaluation of the systematic errors was possible by including the check of the method with 400 simulated L3+C experiments, the subsample analysis, the fit function bias and the additional acceptance cross check with the Z^0 events.

The long term stability of the measured rates was found to be 2.5% in [117], and is 0.3% here (0.5% if atmospheric effects are not corrected for). Depending on the zenith angle, the previous study quoted flux normalization uncertainties ranging from 3.2 to 12%, whereas here the estimated uncertainties are all below 3.9%.
The vertical muon spectrum and charge ratio of the two analyses, as well as the zenith angle dependence of the flux at momenta around 300 GeV are compared in figure 6.25. The unfolding procedure applied in [117] constitutes a regularization constraint similar to the flux fit according to equation 6.13, therefore in both of the cases the shown errors are dominated by the systematic uncertainties.
For the purpose of this comparison, the flux normalization of the previous measurement was corrected for the event loss explained in section 4.4 a posteriori, as it was not known at the time of that analysis.
Neglecting the overall normalization, good agreement is found concerning the shape of the vertical muon spectrum at high momenta. The asymptotic normalization difference between the two analyses in the vertical direction is larger than expected from the estimated normalization uncertainties. On average however, the flux from [117] agrees with this result as can be seen in figure 6.25(b)*.
Due to an error in a previous version of the simulation of the molasse overburden, the vertical matter thickness X_0 (see equation (6.45)) was assumed about 960 gcm^{-2} too low corresponding to an underestimation of the vertical energy loss of about 3 GeV for surface momenta of 100 GeV. Whereas here a revised version of the molasse simulation was used, the approximate procedure applied in [117] to correct this flaw did not allow to examine events with a surface momentum below 40 GeV. The observed shape difference between the two analyses at low energies may be related to this problem, the details of the discrepancy are however not understood.
Excellent agreement is found for the vertical charge ratio. In this analysis, the smaller alignment uncertainties of the double octant fit allowed for an extension of the investigated momentum range by a factor two.

*Note that the vertical zenith angle range of [117] is different in figures 6.25(a) and (c) ($\cos(\theta) > 0.985$) and figure 6.25(b) ($\cos(\theta) > 0.970$).

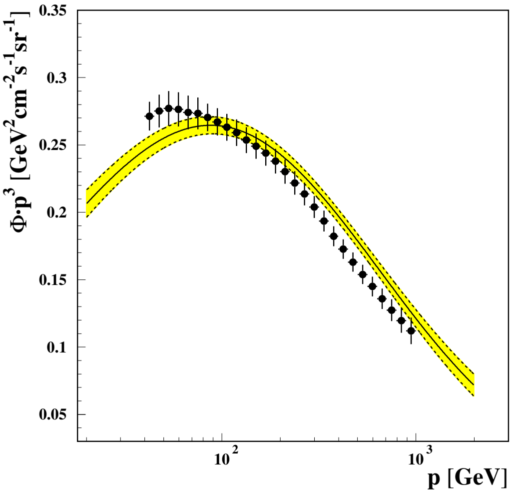

(a) vertical muon spectrum

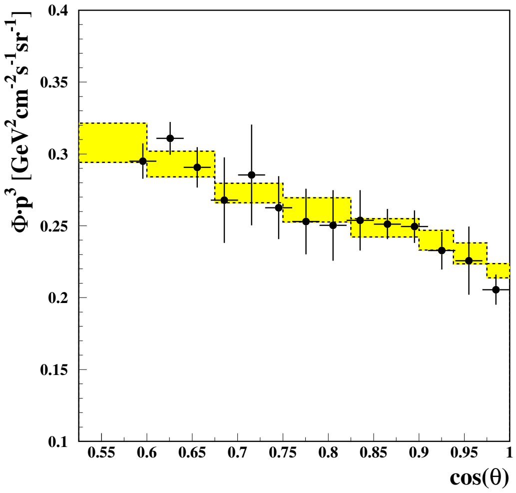

(b) zenith angle dependence of muon flux between 281 and 316 GeV

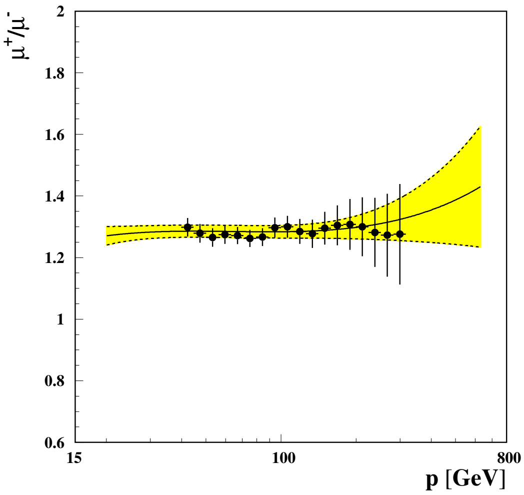

(c) vertical charge ratio

Fig. 6.25: *Comparison to previous L3+C results. The solid line and the shaded areas denote the flux fit result of this analysis, dots are taken from [117]. The shaded areas and error bars denote the total error estimated in the respective analysis.*

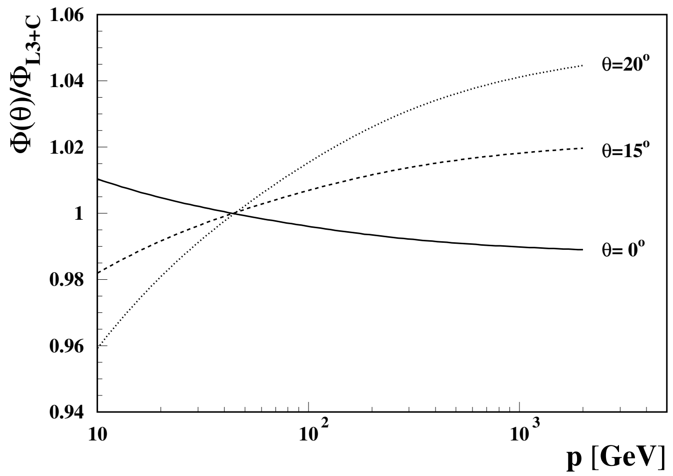

Fig. 6.26: *Expected vertical flux ratio to L3+C for experiments measuring a mean* $\cos(\theta)$ *corresponding to 0, 15 and 20°. For this analysis* $\langle\cos\theta\rangle = 0.988$.

6.6.3 Comparison to previous experiments

In figure 6.27, this muon flux measurement is compared to results from previous experiments. Only experiments providing an absolute normalization [16,22,31,38,52,67,92] have been taken into account. As no previous continuous zenith angle measurements exist in the large energy range examined here, only the vertical direction can be compared. The definition of 'vertical' is presumably different for each experiment, however, only two of them state the opening angle of their apparatus. The CAPRICE [38,92] apparatus measured the flux within its opening angle of 20^o, whereas the AHM79 [67] experiment was determining the muon flux within zenith angles of $< 9^o$. Even for these two experiments, a correction for the opening angle difference with respect to L3+C is not straightforward, as the zenith angle dependence of the acceptance within the vertical solid angle needs to be known to calculate the mean cosine of the zenith angle. The expected flux ratio deviations to L3+C, as calculated with the analytic formulae from chapter 2, are however below 5% even for large opening angle differences, as shown in figure 6.26.
Due to the decay and energy loss of atmospheric muons, the muon flux depends also on the detector height. Therefore all flux measurements were corrected to the L3+C detector height using the formula given in [79].

In the upper part of figure 6.27, previous measurements of the low energetic muon flux can be seen. Very good agreement between this results and the AHM71 flux [31]

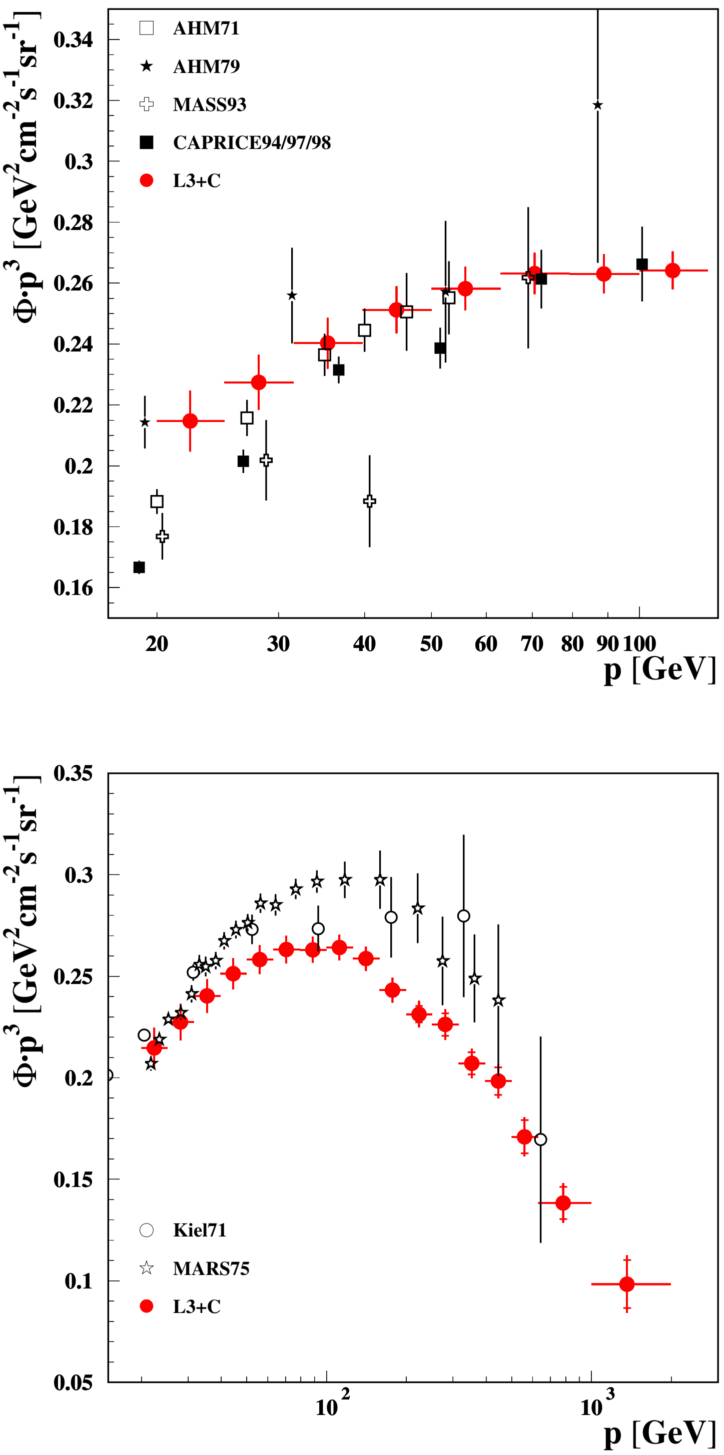

Fig. 6.27: *Comparison of the muon flux results of this analysis to previous measurements. All flux data are corrected to the L3+C altitude using the formula given in [79].*

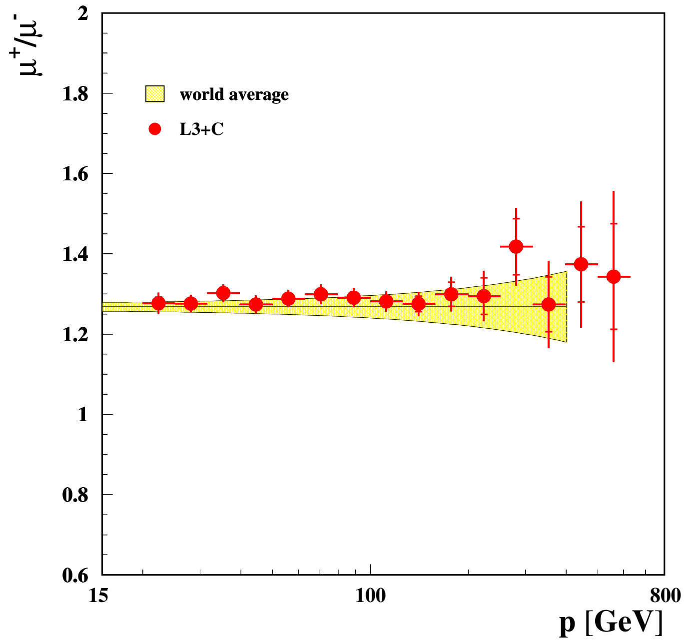

Fig. 6.28: *Comparison of the muon charge ratio to world average calculated in [79].*

is found. The spectra from the CAPRICE experiment, which were averaged here over the three measurement campaigns, agree within a few percent in normalization to the L3+C spectrum. However, at very low energies a systematic slope difference seems to be present, part of which may be due to the different opening angle as explained above.

At high energies only two experiments measured a normalized spectrum. The shape of the Kiel measurement [16] agrees very well with this result over the full momentum range, but a lower flux normalization was determined in L3+C. The data obtained with the MARS apparatus [22] significantly disagree both in shape and normalization with the spectrum presented here. Given the large errors of these two experiments above 200 GeV, it can be stated, that L3+C extended the knowledge on the muon momentum spectrum by a factor 10 in the momentum range.

Finally, the vertical charge ratio is compared to the world average calculated in [79]. Good agreement is found over the full momentum range. It is worthwhile pointing out, that the total error of one zenith angle bin from this experiment is compatible with the error from the average of all previous experiments.

Chapter 7

COMPARISON TO AIR SHOWER SIMULATIONS

In this chapter, the measured muon fluxes and charge ratios will be compared to theoretical predictions obtained with air shower simulations.
These calculations were performed with the `TARGET` [57] transport code in its one dimensional version, i. e. all secondary particles are assumed to follow the direction of the incoming primary particle. To cross-check a possible systematic error due to the implementation of the particle transport through the atmosphere, the results were compared to a calculation with the `CORSIKA` transport code [80] using the same primary flux and high energy interaction model. No significant difference was observed in the energy range above 100 GeV (below, no comparison was possible due to the different low energetic interaction models implemented in the two programs).

Interaction models

The following three high energy interaction models are available within the `TARGET` program:

- `TARGET2.1` [57] is a phenomenological model, based on the parameterization of accelerator data, which are extrapolated to the full phase space, energies and target nuclei needed in atmospheric air showers. Calculations of the neutrino flux [8] based on this model are extensively used to interpret the data of atmospheric neutrino detectors.

- `QGSJET01` [89] and `SIBYLL2.1` [56, 61] are microscopic models, which predict the hadronic interactions from first principles and consequently have a much smaller number of free parameters as the phenomenological `TARGET` model. For large momentum transfers between the projectile and target nucleus, the well tested perturbative QCD theory is applicable. For momentum transfers below a few GeV, the hadronic interactions are modeled based on the Gribov-Regge theory [69,120] in case of `QGSJET01`, whereas they are described by the production of colored strings [46] in `SIBYLL2.1`.

As no low energy model other than `TARGET` is implemented in the current version of the transport code all interactions below a laboratory energy of 100 GeV are handled by this model.

Primary flux model

For the absolute normalization of the simulated muon flux, a model of the primary particle flux is needed. Figure 7.1 displays direct measurements of the primary proton and helium component of the cosmic particle flux. Obviously, the indirect measurements of the primary flux mentioned in chapter 2 can not be used for this purpose, as there interaction models are needed to infer the flux from the ground level observations.
Below 100 GeV, for both elements good measurements with an acceptable statistical accuracy exist. At high energies even the two most precise balloon experiments [20,21] exhibit large statistical uncertainties. Assuming that the power law ansatz for the primary flux holds up to a few hundreds of TeV, the low energy measurements alone provide a sufficiently large lever arm to determine the two flux parameters in equation (2.4). Unfortunately, the low energy measurement do not agree with each other within the quoted statistical errors, which indicates the presence of systematic errors not accounted for. For protons, the major difference is between the two CAPRICE measurements and the results from BESS and AMS. Therefore, the parameterization from [65], based on the two latter experiments, and the fit from CAPRICE [38], will be used as an upper and lower estimate of the proton flux. Both parameterizations are indicated by lines in figure 7.1(a).
In case of the helium component the situation is similar, but here the two high energy measurements show a systematic normalization difference. The parameterization of the same authors as above is shown in figure 7.1(b). The minimum of the CAPRICE fit and GH2 will be used as a lower limit of the helium flux, the GH1 fit as an upper limit.
The contribution of heavier nuclei to the all nucleon spectrum are taken from [65].

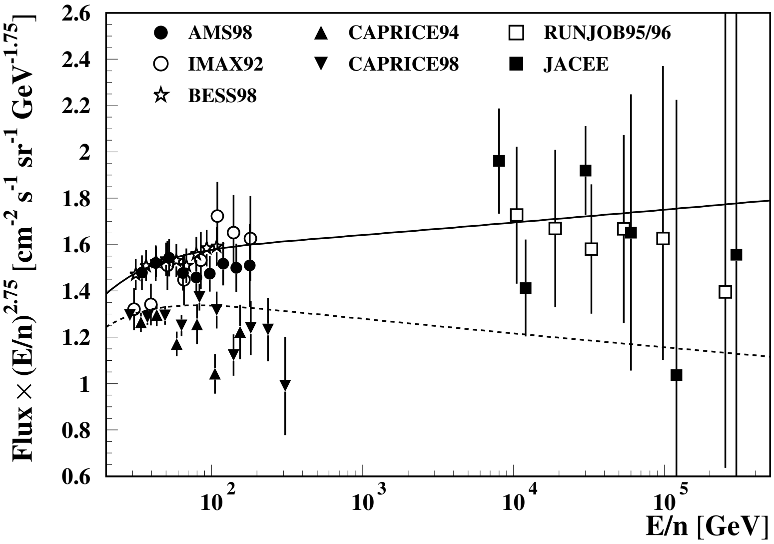

(a) *Protons*

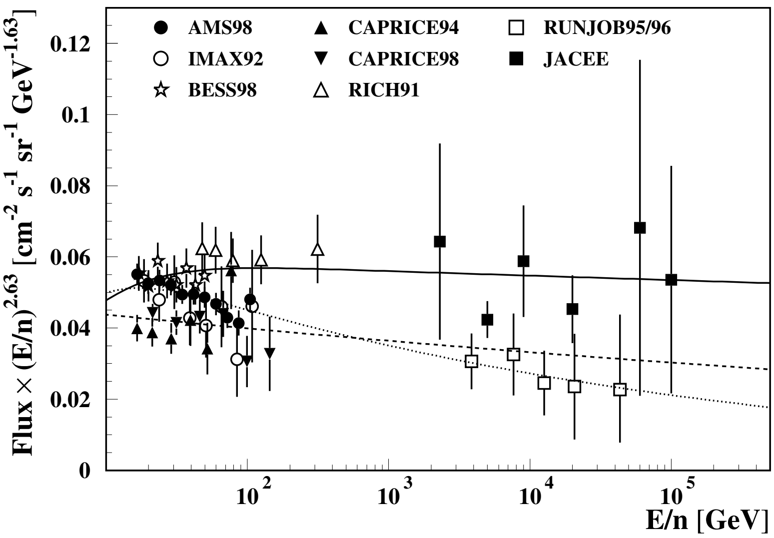

(b) *Helium*

Fig. 7.1: *Primary proton and helium flux as a function of energy per nucleon from direct measurements (AMS: [12, 13], BESS: [122], CAPRICE: [36, 37], IMAX [110], JACEE [21], RICH [43] and RUNJOB [20]). The lines are fits to the low energy data from [38] (dashed) and [65] (solid and dotted).*

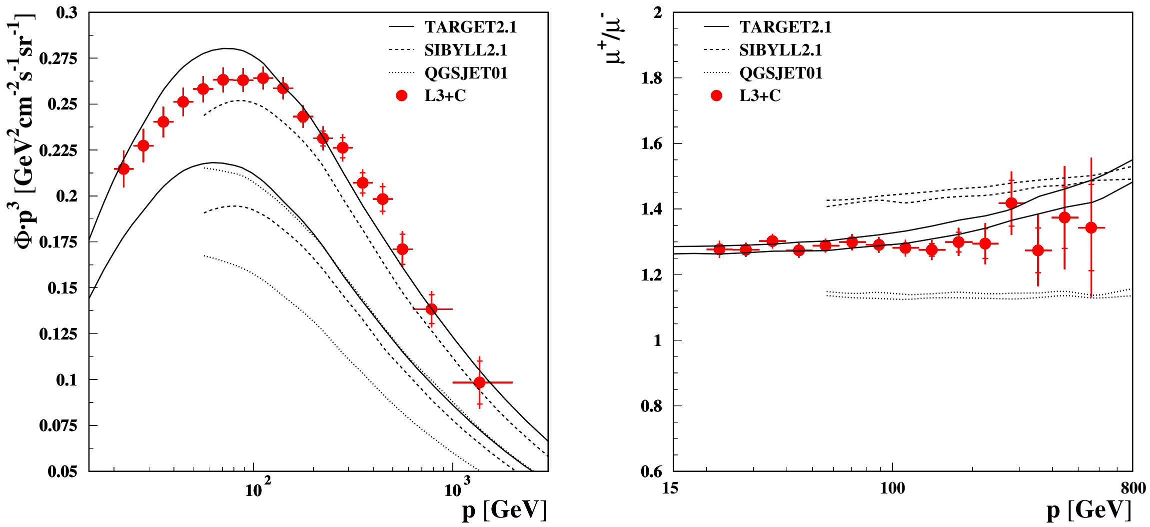

(a) *Muon flux*　　(b) *Charge ratio*

Fig. 7.2: *Simulated muon fluxes with different interaction models and primary fluxes compared to this measurement.*

Muon flux and charge ratio

The simulated muon fluxes and charge ratios are presented in figure 7.2. In order to distinguish clearly between the models, the results from `QGSJET` and `SIBYLL` are only displayed down to 60 GeV, above which the low energy interaction model does not contribute to the simulated flux. For each interaction model two results are shown, corresponding to 'worst case' combinations of the four proton and helium spectra. For the muon flux this is given by the combination of the two maximum and minimum fluxes (denoted as Φ^+ and Φ^- respectively). The charge ratio is influenced by the primary neutron to proton ratio, therefore the combinations of the high proton and low helium flux and vice versa result in the largest differences (denoted as $\Phi^\pm$ and $\Phi^\mp$ respectively).

The best agreement with the L3+C data is obtained with the Φ^+ primary flux and the simple `TARGET` model. Also the Φ^+-`SIBYLL` flux prediction is close to this data and could be easily matched by using an even slightly higher primary flux. The `QGSJET` spectrum is significantly too low for both of the cases and an about 20-40% higher flux as the Φ^+ parameterization would be needed to match it with this result, which is not supported by the current primary flux data. Using the Φ^- normalization, all of the

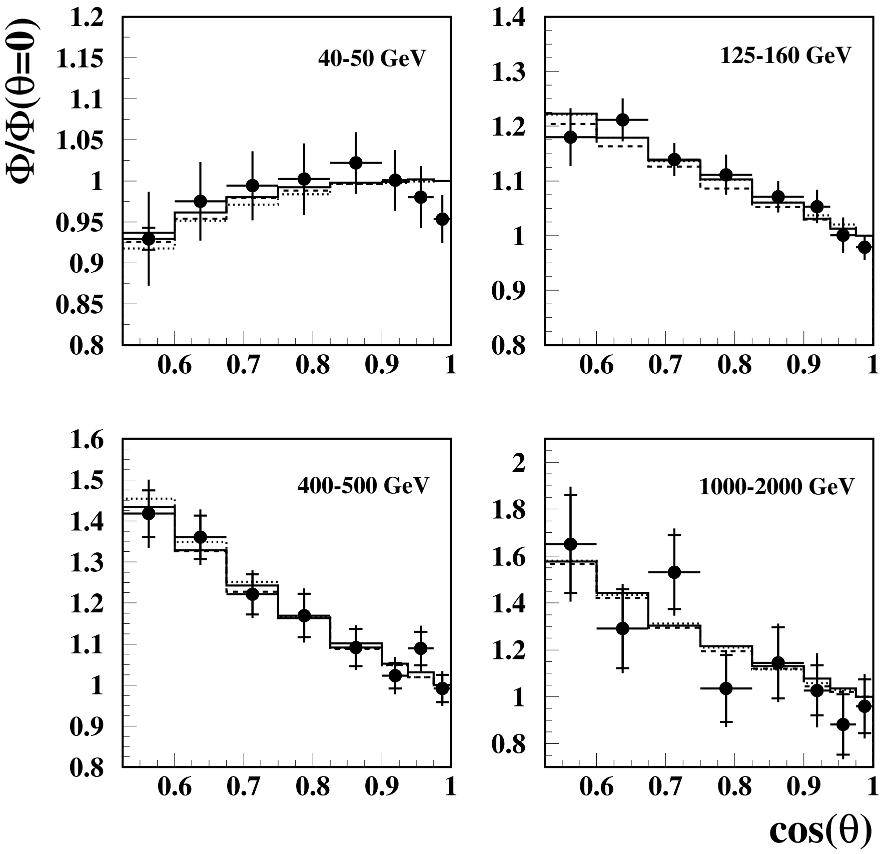

Fig. 7.3: *L3+C zenith angle dependence of muon flux at four momenta compared to the air shower simulations (solid:* `TARGET2.1`*, dashed:* `SIBYLL` *and dotted:* `QGSJET`*).*

resulting muon spectra are significantly too low compared to L3+C.

For the muon charge ratio, shown in figure 7.2(b), the influence of the different primary flux models $\Phi^{\pm}$ and $\Phi^{\mp}$ is only of the order of percent. Again the predictions of the `TARGET` model are compatible with this measurement. The rise of the charge ratio at high energies can be attributed to large fraction of positive K-mesons, responsible for 20% of the muon flux at 600 GeV. The systematic errors of the detector alignment however do not allow for a stringent check of the magnitude of the effect, as the data would also allow for a flat charge ratio momentum dependence (see the previous chapter). The `SIBYLL` model predicts a significantly too large muon charge ratio due to both a large π^+/π^- and $K^+/(\pi + K)$ ratio over the full investigated momentum range. The opposite is true for `QGSJET`, exhibiting a correspondingly much too low charge ratio.

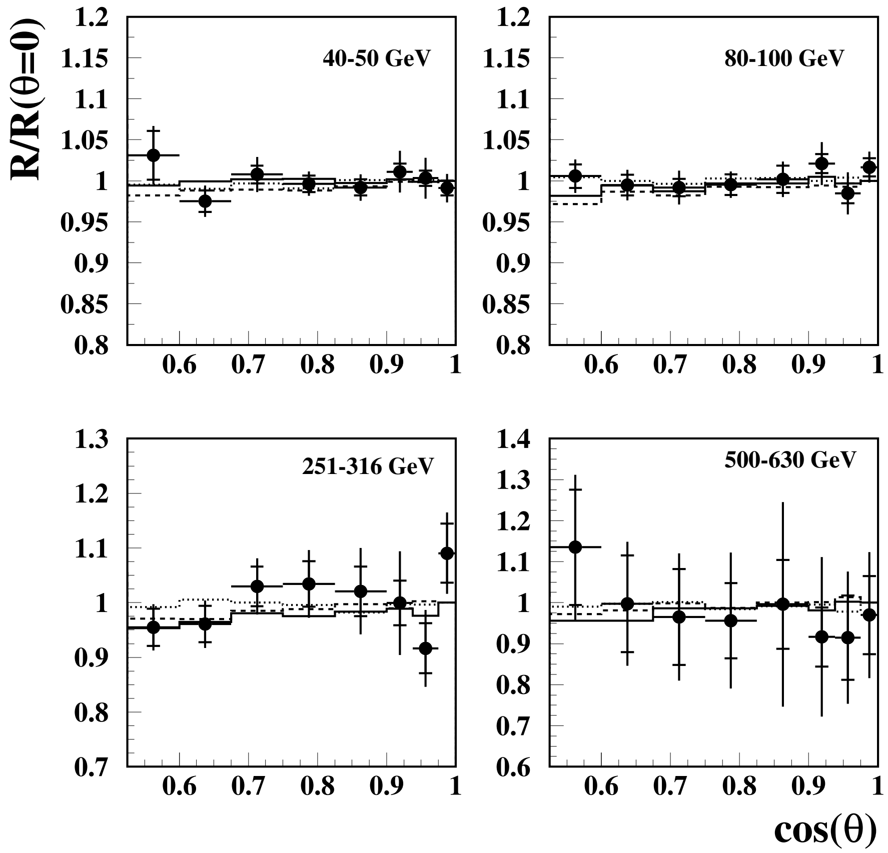

Fig. 7.4: *L3+C zenith angle dependence of charge ratio at four momenta compared to the air shower simulations (solid: `TARGET2.1`, dashed: `SIBYLL` and dotted: `QGSJET`).*

Zenith angle dependence

According to the analytical approximation introduced in chapter 2, besides trivial factors and the muon decay, the relative zenith angle dependence of the muon flux is introduced by the difference between the meson and nucleon attenuation length in equation (2.32). The simulated zenith angle dependence and muon charge ratio are shown in figures 7.3 and 7.4 for four different momenta. In order to disentangle the relative zenith angle dependence from the overall normalization and absolute charge ratio, both data and MC were normalized to the vertical zenith angle bin. Excellent agreement is found both between the simulation and the L3+C data demonstrating the reliability of the transport code.

Constraining the neutrino spectrum

A calculation of the atmospheric neutrino flux is beyond the scope of this work, which focused on the experimental determination of the muon flux. However, it is interesting to estimate the expected improvement on the knowledge of the neutrino flux using the muon flux to constrain the neutrino flux predictions.
For this purpose, the muon flux constraint is studied with the air shower simulations discussed in the previous sections. The simulated neutrino fluxes for the different interaction models and the Φ^+ and Φ^- primary fluxes are shown in figure 7.5(a). As can be seen, both the uncertainties on the primary flux and interactions in the atmosphere have a large impact on the predicted neutrino fluxes.
In this study, it is assumed, that the 'observed' muon and 'true' neutrino spectrum follow the ones obtained with `TARGET` and the average of the Φ^+ and Φ^- primary flux model. Inspired by the analytic approximations of the muon and neutrino spectrum (2.30) given in chapter 2, each simulated muon flux Φ_{μ_i} is fitted to the observed muon spectrum and charge ratio by rescaling the fluxes according to

$$\Phi'_{\mu_i} = (\Phi^{\mu^+}_{\pi,i} + \Phi^{\mu^-}_{\pi,i} + b \cdot \Phi^{\mu^+}_{K,i} + \Phi^{\mu^-}_{K,i}) \cdot a \cdot p^{\Delta\gamma} \tag{7.1}$$

and

$$R' = \frac{\Phi^{\mu^+}_{\pi,i} + b \cdot \Phi^{\mu^+}_{K,i}}{\Phi^{\mu^-}_{\pi,i} + \Phi^{\mu^-}_{K,i}} \,. \tag{7.2}$$

Here $\Phi^{\mu^\pm}_{\pi/K}$ denote the positive and negative muon fluxes from parent pions and kaons respectively, a is a global normalization factor, b adjusts the fraction of muons originating from the decay of K^+ mesons and $\Delta\gamma$ is the difference between the simulated and true primary nucleon spectral index.
Given the large systematic error of the measured charge ratio at high momenta, the charge ratio constraint is only applied below 150 GeV.
The obtained parameters a, b and $\Delta\gamma$ are then used to rescale the simulated neutrino fluxes as follows:

$$\Phi'_{\nu_i} = (\Phi^{\nu}_{\pi,i} + \Phi^{\overline{\nu}}_{\pi,i} + b \cdot \Phi^{\nu}_{K,i} + \Phi^{\overline{\nu}}_{K,i}) \cdot a \cdot p^{\Delta\gamma} \,. \tag{7.3}$$

The resulting constrained neutrino fluxes are shown in figure 7.5(b). As it was to be expected from equation (2.35), the uncertainties due to the primary flux vanish almost completely, if the hadronic interaction model is known. Also the difference between the `QGSJET` and `TARGET` Z-factors (cf. table 2.1) is reduced. The largest deviations of the constrained to the true neutrino spectrum is observed for `SIBYLL` at high energies. This

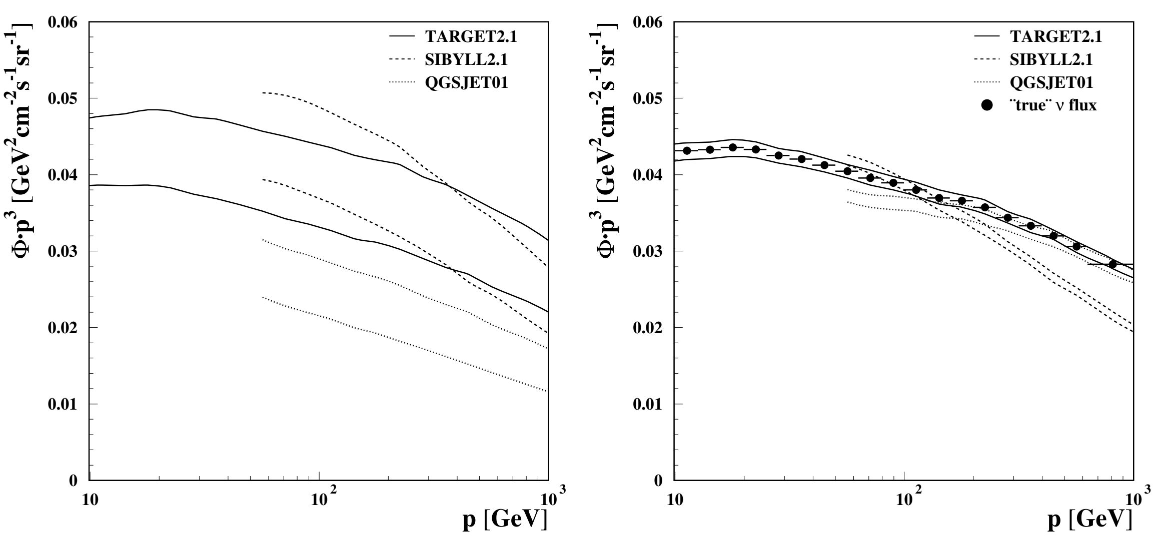

(a) *Unconstrained*

(b) *Constrained to muon flux and low energy charge ratio*

Fig. 7.5: *MC study on the neutrino flux constraint. For each interaction model two different primary fluxes are used, as indicated by the two curves per model.*

can be traced back to the different energy dependence of the kaon Z-factors predicted by `TARGET` and `SIBYLL`, which are increasing with the energy in the former case and decreasing in the latter.

Nevertheless, it can be concluded, that even with the very simple approach used here, a considerable improvement on the knowledge on the absolute neutrino flux can be achieved by constraining the theoretical neutrino flux predictions with the measured muon flux. For a thorough evaluation of the remaining systematic errors, also different low energy models, such as `GHEISHA` [60] and `UrQMD` [30], need to be investigated, and the study of other widely used high energy interaction models, such as `NeXuS` [53] and `DPMJET` [119] is needed.

Chapter 8

SUMMARY AND OUTLOOK

In this thesis, a new measurement of the atmospheric muon spectrum using the L3+C detector is presented. Due to the large exposure of the experiment, its large magnetic volume and an improved momentum determination algorithm, the muon flux could be measured in a momentum range from 20 to 2000 GeV.
During the analysis special attention was given to the precise determination of all relevant detector and environmental parameters needed to convert the raw data distributions to an absolute surface level flux. Due to the large amount of available statistics, extensive studies of the residual systematic uncertainties were possible. The current overall normalization uncertainty of the vertical muon spectrum from previous measurements [79] could be reduced from 7% to 2.4% in the vertical direction at 100 GeV. The measurement covered a wide zenith angle range from 0 to 58^o for both the muon flux and the charge ratio. The latter could be determined up to 630 GeV. The average total uncertainty of the muon flux is 3.0% at 200 GeV. The best average precision of the charge ratio was achieved at 60 GeV and amounts to 1.6%.
The comparison to previous absolute flux measurements showed good overall agreement at low energies, whereas at high energies a lower normalization with respect to the results from [16, 22] was determined.

The work provides an extensive and accurate data set with which the validity of atmospheric neutrino flux calculations can be cross-checked. With the help of the absolute normalization and spectral shape of the measured muon spectrum, the meson production model and the assumed primary particle fluxes used in these calculations can be tested. For a given ratio of positive to negative pion production in the atmosphere, the measured muon charge ratio can furthermore be used to constrain the contribution of positive kaons, which constitute an important source of atmospheric muon neutrinos.

Because of the systematic uncertainties of the measured charge ratio at high energies, the predicted rise of the charge ratio due to the positive kaon contribution to the muon flux could not be confirmed here. Future atmospheric muon measurements, as for instance planned with the ACORDE detector [14] at the LHC, should therefore focus on an accurate detector alignment to keep the related systematics under control.

The study of current high energetic interaction models showed, that only one of the three investigated models succeeds to reproduce the full data set. Interesting enough, this is the phenomenological `TARGET` model, whereas the more sophisticated theoretical models are incompatible with this data even within the large assumed errors of the primary cosmic particle flux.

In the near future, several experiments will close the gap in between the low and high energy primary flux measurements. The upgraded BESS spectrometer [10] will be able to extend the measurement to 600 GeV, the ATIC [9] calorimeter will measure the primary spectrum from 30 to 100 TeV in long duration balloon flights and the AMS [11] detector, when finally launched to the international space station, will have an unprecedented exposure allowing for a high statistics measurement up to several TeV. Thus both, the incoming particle beam and muonic end products on ground level will be known precisely and stringent tests of the high energetic interaction models will be possible.

APPENDIX: TABULATED MUON FLUX RESULTS

Below, the parameters of the muon flux fit for each zenith angle bin are listed along with their statistical and systematic errors σ and the corresponding correlation matrices ρ_{ij}. According to the standard rule of error propagation, the covariance of two flux values $f = \Phi$ or charge ratio values $f = R$ at two arbitrary momenta p_k and p_l is given by

$$V_{kl} = \sum_{i,j=1}^{8} \frac{\partial f_k}{\partial a_i} \frac{\partial f_l}{\partial a_j} \sigma_i \, \sigma_j \, \rho_{ij} \, ,$$

where a_i denote the eight muon flux fit parameters $a_1 = a_1^-, \ldots, a_8 = a_4^+$ as defined in equation (6.11).
For the muon flux the partial derivatives are given by

$$\frac{\partial \Phi_k}{\partial a_i} = \ln(10) \, g_i^k \, \Phi_k^{q_i}$$

and for the charge ratio they read as

$$\frac{\partial R}{\partial a_i} = q_i \, \ln(10) \, g_i^k \, R_k \, .$$

The coefficient functions g_i^k are the derivatives of the exponent F_k in equation (6.11) with respect to the parameters a_i:

$$\begin{aligned}
g_1^k &= \frac{1}{2} (y_k - 2)(y_k - 3) \, y_k \\
g_2^k &= -\frac{1}{3} (y_k - 1)(y_k - 3)(2y_k - 1) \\
g_3^k &= \frac{1}{6} (y_k - 1)(y_k - 2) \, y_k \\
g_4^k &= \frac{1}{3} (y_k - 1)(y_k - 2)(y_k - 3)
\end{aligned}$$

and

$$g_5^k = g_1^k, \; g_6^k = g_2^k, \; g_7^k = g_3^k, \; g_8^k = g_4^k \, .$$

Here $y_k = \log_{10} p_k$ and the charge q_i is given by

$$q_i = \begin{cases} -, & i \leq 4 \\ +, & i > 4 \end{cases} ,$$

which should be read as a label in case of the flux and as a sign in case of the charge ratio.

A.1 Muon flux from $0.525 < \cos\theta < 0.600$ between 40 and 2000 GeV

fit result

parameter	value	stat. error	syst. error
a_1^-	-0.232	0.091	0.078
a_2^-	-2.878	0.002	0.017
a_3^-	-6.111	0.014	0.058
a_4^-	-2.706	0.273	0.293
a_1^+	-0.155	0.088	0.066
a_2^+	-2.775	0.002	0.023
a_3^+	-5.897	0.010	0.045
a_4^+	-2.448	0.254	0.183

correlation matrix of statistical errors

	a_1^-	a_2^-	a_3^-	a_4^-	a_1^+	a_2^+	a_3^+	a_4^+
a_1^-	1.000	-0.641	-0.415	-0.993	-0.034	0.023	0.015	0.034
a_2^-	-0.641	1.000	0.126	0.642	0.023	-0.019	-0.007	-0.023
a_3^-	-0.415	0.126	1.000	0.490	0.017	-0.009	-0.024	-0.018
a_4^-	-0.993	0.642	0.490	1.000	0.034	-0.023	-0.017	-0.035
a_1^+	-0.034	0.023	0.017	0.034	1.000	-0.682	-0.292	-0.995
a_2^+	0.023	-0.019	-0.009	-0.023	-0.682	1.000	0.080	0.687
a_3^+	0.015	-0.007	-0.024	-0.017	-0.292	0.080	1.000	0.354
a_4^+	0.034	-0.023	-0.018	-0.035	-0.995	0.687	0.354	1.000

correlation matrix of systematic errors

	a_1^-	a_2^-	a_3^-	a_4^-	a_1^+	a_2^+	a_3^+	a_4^+
a_1^-	1.000	0.544	-0.610	-0.904	0.362	0.449	0.554	0.038
a_2^-	0.544	1.000	0.219	-0.217	0.688	0.984	0.409	-0.271
a_3^-	-0.610	0.219	1.000	0.888	0.425	0.259	-0.476	-0.529
a_4^-	-0.904	-0.217	0.888	1.000	0.025	-0.142	-0.590	-0.314
a_1^+	0.362	0.688	0.425	0.025	1.000	0.631	-0.290	-0.850
a_2^+	0.449	0.984	0.259	-0.142	0.631	1.000	0.407	-0.235
a_3^+	0.554	0.409	-0.476	-0.590	-0.290	0.407	1.000	0.745
a_4^+	0.038	-0.271	-0.529	-0.314	-0.850	-0.235	0.745	1.000

A.2 Muon flux from $0.600 < \cos\theta < 0.675$ between 40 and 2000 GeV

fit result

parameter	value	stat. error	syst. error
a_1^-	-0.165	0.055	0.079
a_2^-	-2.875	0.001	0.012
a_3^-	-6.142	0.013	0.060
a_4^-	-2.730	0.176	0.265
a_1^+	-0.093	0.054	0.059
a_2^+	-2.770	0.001	0.017
a_3^+	-5.968	0.009	0.036
a_4^+	-2.569	0.167	0.119

correlation matrix of statistical errors

	a_1^-	a_2^-	a_3^-	a_4^-	a_1^+	a_2^+	a_3^+	a_4^+
a_1^-	1.000	-0.667	-0.445	-0.991	-0.004	0.002	0.013	0.006
a_2^-	-0.667	1.000	0.071	0.636	0.004	-0.016	0.003	-0.004
a_3^-	-0.445	0.071	1.000	0.527	0.005	0.006	-0.048	-0.009
a_4^-	-0.991	0.636	0.527	1.000	0.005	-0.001	-0.017	-0.008
a_1^+	-0.004	0.004	0.005	0.005	1.000	-0.708	-0.324	-0.993
a_2^+	0.002	-0.016	0.006	-0.001	-0.708	1.000	0.043	0.690
a_3^+	0.013	0.003	-0.048	-0.017	-0.324	0.043	1.000	0.399
a_4^+	0.006	-0.004	-0.009	-0.008	-0.993	0.690	0.399	1.000

correlation matrix of systematic errors

	a_1^-	a_2^-	a_3^-	a_4^-	a_1^+	a_2^+	a_3^+	a_4^+
a_1^-	1.000	0.530	-0.693	-0.923	0.890	0.407	0.509	-0.858
a_2^-	0.530	1.000	0.148	-0.231	0.765	0.954	0.320	-0.483
a_3^-	-0.693	0.148	1.000	0.915	-0.328	0.178	-0.476	0.524
a_4^-	-0.923	-0.231	0.915	1.000	-0.666	-0.146	-0.551	0.749
a_1^+	0.890	0.765	-0.328	-0.666	1.000	0.641	0.238	-0.903
a_2^+	0.407	0.954	0.178	-0.146	0.641	1.000	0.351	-0.348
a_3^+	0.509	0.320	-0.476	-0.551	0.238	0.351	1.000	-0.012
a_4^+	-0.858	-0.483	0.524	0.749	-0.903	-0.348	-0.012	1.000

A.3 Muon flux from $0.675 < \cos\theta < 0.750$ between 32 and 2000 GeV

fit result

parameter	value	stat. error	syst. error
a_1^-	-0.208	0.038	0.061
a_2^-	-2.881	0.001	0.010
a_3^-	-6.182	0.013	0.060
a_4^-	-2.492	0.131	0.196
a_1^+	-0.007	0.036	0.052
a_2^+	-2.781	0.001	0.015
a_3^+	-6.013	0.010	0.041
a_4^+	-2.745	0.118	0.106

correlation matrix of statistical errors

	a_1^-	a_2^-	a_3^-	a_4^-	a_1^+	a_2^+	a_3^+	a_4^+
a_1^-	1.000	-0.590	-0.466	-0.989	-0.058	0.026	0.046	0.063
a_2^-	-0.590	1.000	-0.005	0.533	0.029	-0.056	0.005	-0.026
a_3^-	-0.466	-0.005	1.000	0.556	0.037	0.006	-0.112	-0.048
a_4^-	-0.989	0.533	0.556	1.000	0.061	-0.023	-0.056	-0.067
a_1^+	-0.058	0.029	0.037	0.061	1.000	-0.637	-0.378	-0.990
a_2^+	0.026	-0.056	0.006	-0.023	-0.637	1.000	-0.013	0.589
a_3^+	0.046	0.005	-0.112	-0.056	-0.378	-0.013	1.000	0.466
a_4^+	0.063	-0.026	-0.048	-0.067	-0.990	0.589	0.466	1.000

correlation matrix of systematic errors

	a_1^-	a_2^-	a_3^-	a_4^-	a_1^+	a_2^+	a_3^+	a_4^+
a_1^-	1.000	0.624	-0.618	-0.898	0.729	0.442	0.465	-0.507
a_2^-	0.624	1.000	0.104	-0.298	0.840	0.865	0.201	-0.584
a_3^-	-0.618	0.104	1.000	0.900	0.035	0.094	-0.620	-0.125
a_4^-	-0.898	-0.298	0.900	1.000	-0.388	-0.202	-0.594	0.222
a_1^+	0.729	0.840	0.035	-0.388	1.000	0.667	-0.089	-0.885
a_2^+	0.442	0.865	0.094	-0.202	0.667	1.000	0.285	-0.384
a_3^+	0.465	0.201	-0.620	-0.594	-0.089	0.285	1.000	0.491
a_4^+	-0.507	-0.584	-0.125	0.222	-0.885	-0.384	0.491	1.000

A.4 Muon flux from $0.750 < \cos\theta < 0.825$ between 32 and 2000 GeV

fit result

parameter	value	stat. error	syst. error
a_1^-	-0.130	0.044	0.062
a_2^-	-2.889	0.001	0.013
a_3^-	-6.264	0.015	0.076
a_4^-	-2.756	0.155	0.221
a_1^+	-0.004	0.025	0.049
a_2^+	-2.788	0.001	0.016
a_3^+	-6.023	0.010	0.054
a_4^+	-2.712	0.091	0.119

correlation matrix of statistical errors

	a_1^-	a_2^-	a_3^-	a_4^-	a_1^+	a_2^+	a_3^+	a_4^+
a_1^-	1.000	-0.591	-0.545	-0.990	-0.021	0.010	0.011	0.021
a_2^-	-0.591	1.000	0.041	0.536	0.012	-0.006	-0.005	-0.012
a_3^-	-0.545	0.041	1.000	0.628	0.012	-0.005	-0.009	-0.013
a_4^-	-0.990	0.536	0.628	1.000	0.020	-0.010	-0.011	-0.021
a_1^+	-0.021	0.012	0.012	0.020	1.000	-0.506	-0.413	-0.986
a_2^+	0.010	-0.006	-0.005	-0.010	-0.506	1.000	-0.087	0.430
a_3^+	0.011	-0.005	-0.009	-0.011	-0.413	-0.087	1.000	0.513
a_4^+	0.021	-0.012	-0.013	-0.021	-0.986	0.430	0.513	1.000

correlation matrix of systematic errors

	a_1^-	a_2^-	a_3^-	a_4^-	a_1^+	a_2^+	a_3^+	a_4^+
a_1^-	1.000	0.457	-0.677	-0.903	0.516	0.438	0.607	-0.117
a_2^-	0.457	1.000	0.176	-0.131	0.714	0.983	0.208	-0.351
a_3^-	-0.677	0.176	1.000	0.926	0.250	0.113	-0.740	-0.470
a_4^-	-0.903	-0.131	0.926	1.000	-0.126	-0.155	-0.718	-0.192
a_1^+	0.516	0.714	0.250	-0.126	1.000	0.617	-0.217	-0.837
a_2^+	0.438	0.983	0.113	-0.155	0.617	1.000	0.283	-0.237
a_3^+	0.607	0.208	-0.740	-0.718	-0.217	0.283	1.000	0.691
a_4^+	-0.117	-0.351	-0.470	-0.192	-0.837	-0.237	0.691	1.000

A.5 Muon flux from $0.825 < \cos\theta < 0.900$ between 32 and 2000 GeV

fit result

parameter	value	stat. error	syst. error
a_1^-	-0.070	0.029	0.086
a_2^-	-2.902	0.001	0.009
a_3^-	-6.234	0.015	0.131
a_4^-	-2.815	0.113	0.366
a_1^+	-0.029	0.020	0.042
a_2^+	-2.790	0.001	0.014
a_3^+	-6.083	0.012	0.063
a_4^+	-2.591	0.079	0.105

correlation matrix of statistical errors

	a_1^-	a_2^-	a_3^-	a_4^-	a_1^+	a_2^+	a_3^+	a_4^+
a_1^-	1.000	-0.407	-0.547	-0.986	-0.005	-0.001	0.006	0.006
a_2^-	-0.407	1.000	-0.102	0.322	-0.000	-0.002	0.001	0.000
a_3^-	-0.547	-0.102	1.000	0.643	0.006	0.002	-0.010	-0.007
a_4^-	-0.986	0.322	0.643	1.000	0.006	0.001	-0.007	-0.006
a_1^+	-0.005	-0.000	0.006	0.006	1.000	-0.298	-0.516	-0.985
a_2^+	-0.001	-0.002	0.002	0.001	-0.298	1.000	-0.175	0.196
a_3^+	0.006	0.001	-0.010	-0.007	-0.516	-0.175	1.000	0.619
a_4^+	0.006	0.000	-0.007	-0.006	-0.985	0.196	0.619	1.000

correlation matrix of systematic errors

	a_1^-	a_2^-	a_3^-	a_4^-	a_1^+	a_2^+	a_3^+	a_4^+
a_1^-	1.000	0.308	-0.872	-0.954	0.291	0.325	0.810	0.141
a_2^-	0.308	1.000	0.094	-0.074	0.771	0.943	0.121	-0.426
a_3^-	-0.872	0.094	1.000	0.979	0.195	-0.013	-0.876	-0.513
a_4^-	-0.954	-0.074	0.979	1.000	-0.002	-0.144	-0.877	-0.373
a_1^+	0.291	0.771	0.195	-0.002	1.000	0.624	-0.181	-0.826
a_2^+	0.325	0.943	-0.013	-0.144	0.624	1.000	0.248	-0.235
a_3^+	0.810	0.121	-0.876	-0.877	-0.181	0.248	1.000	0.665
a_4^+	0.141	-0.426	-0.513	-0.373	-0.826	-0.235	0.665	1.000

A.6 Muon flux from $0.900 < \cos\theta < 0.938$ between 25 and 2000 GeV

fit result

parameter	value	stat. error	syst. error
a_1^-	-0.162	0.025	0.042
a_2^-	-2.906	0.001	0.009
a_3^-	-6.302	0.012	0.069
a_4^-	-2.569	0.094	0.093
a_1^+	-0.046	0.013	0.039
a_2^+	-2.796	0.001	0.017
a_3^+	-6.063	0.009	0.070
a_4^+	-2.494	0.055	0.091

correlation matrix of statistical errors

	a_1^-	a_2^-	a_3^-	a_4^-	a_1^+	a_2^+	a_3^+	a_4^+
a_1^-	1.000	-0.449	-0.458	-0.984	-0.003	-0.000	0.003	0.003
a_2^-	-0.449	1.000	-0.099	0.373	0.000	-0.001	0.000	-0.000
a_3^-	-0.458	-0.099	1.000	0.565	0.003	0.001	-0.006	-0.004
a_4^-	-0.984	0.373	0.565	1.000	0.003	0.000	-0.004	-0.003
a_1^+	-0.003	0.000	0.003	0.003	1.000	-0.272	-0.425	-0.979
a_2^+	-0.000	-0.001	0.001	0.000	-0.272	1.000	-0.201	0.161
a_3^+	0.003	0.000	-0.006	-0.004	-0.425	-0.201	1.000	0.548
a_4^+	0.003	-0.000	-0.004	-0.003	-0.979	0.161	0.548	1.000

correlation matrix of systematic errors

	a_1^-	a_2^-	a_3^-	a_4^-	a_1^+	a_2^+	a_3^+	a_4^+
a_1^-	1.000	0.691	0.405	-0.923	0.900	0.349	-0.460	-0.947
a_2^-	0.691	1.000	0.253	-0.476	0.816	0.847	-0.003	-0.501
a_3^-	0.405	0.253	1.000	-0.392	0.097	-0.009	-0.816	-0.339
a_4^-	-0.923	-0.476	-0.392	1.000	-0.734	-0.146	0.649	0.994
a_1^+	0.900	0.816	0.097	-0.734	1.000	0.636	-0.061	-0.787
a_2^+	0.349	0.847	-0.009	-0.146	0.636	1.000	0.293	-0.170
a_3^+	-0.460	-0.003	-0.816	0.649	-0.061	0.293	1.000	0.579
a_4^+	-0.947	-0.501	-0.339	0.994	-0.787	-0.170	0.579	1.000

A.7 Muon flux from $0.938 < \cos\theta < 0.975$ between 25 and 2000 GeV

fit result

parameter	value	stat. error	syst. error
a_1^-	-0.052	0.024	0.037
a_2^-	-2.926	0.001	0.010
a_3^-	-6.279	0.015	0.052
a_4^-	-2.925	0.095	0.082
a_1^+	-0.059	0.012	0.039
a_2^+	-2.816	0.001	0.018
a_3^+	-6.097	0.011	0.056
a_4^+	-2.487	0.055	0.086

correlation matrix of statistical errors

	a_1^-	a_2^-	a_3^-	a_4^-	a_1^+	a_2^+	a_3^+	a_4^+
a_1^-	1.000	-0.310	-0.504	-0.984	-0.005	-0.002	0.005	0.005
a_2^-	-0.310	1.000	-0.174	0.208	-0.001	-0.006	0.003	0.002
a_3^-	-0.504	-0.174	1.000	0.611	0.005	0.003	-0.012	-0.007
a_4^-	-0.984	0.208	0.611	1.000	0.005	0.002	-0.006	-0.006
a_1^+	-0.005	-0.001	0.005	0.005	1.000	-0.101	-0.459	-0.979
a_2^+	-0.002	-0.006	0.003	0.002	-0.101	1.000	-0.257	-0.025
a_3^+	0.005	0.003	-0.012	-0.006	-0.459	-0.257	1.000	0.581
a_4^+	0.005	0.002	-0.007	-0.006	-0.979	-0.025	0.581	1.000

correlation matrix of systematic errors

	a_1^-	a_2^-	a_3^-	a_4^-	a_1^+	a_2^+	a_3^+	a_4^+
a_1^-	1.000	0.660	-0.056	-0.881	0.949	0.462	0.019	-0.786
a_2^-	0.660	1.000	0.251	-0.366	0.808	0.913	0.148	-0.422
a_3^-	-0.056	0.251	1.000	0.416	0.150	0.087	-0.677	-0.327
a_4^-	-0.881	-0.366	0.416	1.000	-0.732	-0.223	-0.050	0.701
a_1^+	0.949	0.808	0.150	-0.732	1.000	0.656	-0.033	-0.775
a_2^+	0.462	0.913	0.087	-0.223	0.656	1.000	0.349	-0.160
a_3^+	0.019	0.148	-0.677	-0.050	-0.033	0.349	1.000	0.598
a_4^+	-0.786	-0.422	-0.327	0.701	-0.775	-0.160	0.598	1.000

A.8 Muon flux from $0.975 < \cos\theta < 1.000$ between 20 and 2000 GeV

fit result

parameter	value	stat. error	syst. error
a_1^-	-0.150	0.020	0.035
a_2^-	-2.937	0.001	0.008
a_3^-	-6.324	0.014	0.053
a_4^-	-2.647	0.082	0.088
a_1^+	-0.065	0.011	0.036
a_2^+	-2.829	0.001	0.013
a_3^+	-6.132	0.010	0.051
a_4^+	-2.500	0.048	0.093

correlation matrix of statistical errors

	a_1^-	a_2^-	a_3^-	a_4^-	a_1^+	a_2^+	a_3^+	a_4^+
a_1^-	1.000	-0.248	-0.513	-0.983	-0.012	-0.007	0.015	0.015
a_2^-	-0.248	1.000	-0.204	0.140	-0.005	-0.025	0.011	0.009
a_3^-	-0.513	-0.204	1.000	0.623	0.013	0.013	-0.042	-0.020
a_4^-	-0.983	0.140	0.623	1.000	0.015	0.010	-0.020	-0.018
a_1^+	-0.012	-0.005	0.013	0.015	1.000	-0.112	-0.426	-0.974
a_2^+	-0.007	-0.025	0.013	0.010	-0.112	1.000	-0.265	-0.023
a_3^+	0.015	0.011	-0.042	-0.020	-0.426	-0.265	1.000	0.563
a_4^+	0.015	0.009	-0.020	-0.018	-0.974	-0.023	0.563	1.000

correlation matrix of systematic errors

	a_1^-	a_2^-	a_3^-	a_4^-	a_1^+	a_2^+	a_3^+	a_4^+
a_1^-	1.000	0.647	-0.267	-0.854	0.867	0.490	0.168	-0.547
a_2^-	0.647	1.000	0.210	-0.320	0.776	0.889	0.060	-0.448
a_3^-	-0.267	0.210	1.000	0.700	0.210	0.039	-0.710	-0.461
a_4^-	-0.854	-0.320	0.700	1.000	-0.527	-0.272	-0.362	0.252
a_1^+	0.867	0.776	0.210	-0.527	1.000	0.597	-0.213	-0.808
a_2^+	0.490	0.889	0.039	-0.272	0.597	1.000	0.262	-0.187
a_3^+	0.168	0.060	-0.710	-0.362	-0.213	0.262	1.000	0.728
a_4^+	-0.547	-0.448	-0.461	0.252	-0.808	-0.187	0.728	1.000

BIBLIOGRAPHY

[1] G. Abbiendi et al., Eur. Phys. J. **C16** (2000) 1.

[2] P. Abreu et al., Nucl. Phys. **B417** (1994) 3.

[3] P. Abreu et al., Eur. Phys. J. **C16** (2000) 371.

[4] M. Acciarri et al., Z. Phys. **C62** (1994) 551.

[5] M. Acciarri et al., Eur. Phys. J. **C16** (2000) 1.

[6] B. Adeva et al., Nucl. Instr. and Meth. **A289** (1990) 35.

[7] O. Adriani et al., Nucl. Instr. and Meth. **A488** (2002) 209.

[8] V. Agrawal et al., Phys. Rev. **D53** (1996) 1314.

[9] H. S. Ahn et al., Proc. 28th ICRC (2003) 1853.

[10] Y. Ajima et. al., Nucl. Instr. Meth. **A416** (2000) 71.

[11] J. Alcaraz et al., Phys. Lett. **B461** (1999) 387.

[12] J. Alcaraz et al., Phys. Lett. **B490** (2000) 27.

[13] J. Alcaraz et al., Phys. Lett. **B494** (2000) 193.

[14] B. Alessandro et al., Proc. 28th ICRC (2003) 1203.

[15] W. W. M. Allison et al., Phys. Lett. **B391** (1997) 491.

[16] O. C. Allkofer et al., Phys. Lett. **B36** (1971) 425.

[17] M. Ambrosio et al., Astropart. Phys. **7** (1997) 109.

[18] M. Ambrosio et al., Phys. Lett. **B434** (1998) 451.

[19] C. D. Anderson, Phys. Rev. **43** (1933) 491:498.

[20] A. Apanasenko et al., Astropart. Phys. **16** (2001) 13.

[21] K. Asakimori et al., ApJ **502** (1998) 278.

[22] C. A. Ayre et al, J. Phys. **G1** (1975) 584.

[23] J. Bähr et al., *Precision measurement of the cosmic ray muon momentum spectrum between 20 and 2000* GeV/c, 1996, L3 internal note No. 1977.

[24] J. Bähr et al., *An effective method to read out large scintillator areas with precise timing*, 1998, DESY preprint PHE98-003, and SCIFI97.

[25] A. Ball et al., *Search for Cosmic Ray Coincidences with Detectors in the LEP Tunnel*, 1994, LEPC 94-10.

[26] R. Barate et al., Eur. Phys. J. **C14** (2000) 1.

[27] D. Bardin et al., Z. Phys. **C44** (1989) 493.

[28] S. Barr, Phys. Lett. **1** (1993) 195.

[29] P. H. Barrett et al., Rev. Mod. Phys. **24** (1952) 133.

[30] S. A. Bass et al., Prog. Part. Nucl. Phys. (1998) 225.

[31] B. J. Bateman et al., Phys. Lett. **B36** (1971) 144.

[32] G. Battistoni et al., Astropart. Phys. **12** (2000) 315.

[33] P. L. Biermann, T. K. Gaisser, and T. Stanev, Phys. Rev. **D51** (1995) 3450.

[34] D. J. Bird et al., ApJ **424** (1994) 491.

[35] V. Blobel, *Unfolding methods in high-energy physics experiments*, 1985, 85-02.

[36] M. Boezio et al., ApJ **518** (1999) 457.

[37] M. Boezio et al., Astropart. Phys. **19** (2003) 583.

[38] M. Boezio et al., Phys. Rev. **D67** (2003) 72003.

[39] S. Bottai and L. Perrone, Nucl. Instr. and Meth. **A459** (2001) 319.

[40] I. C. Brock et al., Nucl. Instr. and Meth. **A381** (1996) 236.

[41] C. Brouwer et al., NIM **A313** (1992) 50.

[42] R. Brun et al., CERN Report **DD/EE/84-1** (1987).

[43] J. Buckley et al., ApJ **429** (1994) 736.

[44] E. V. Bugaev et al., *Cosmic Muons and Neutrinos*, Atomizdat, Moscow, (1970).

[45] E. V. Bugaev et al., Phys. Rev. **D58** (1998) 54001.

[46] A. Capella and A. Krzywicki, Phys. Rev. **D18** (1978) 3357.

[47] H. Chen et al., Phys. Rep. **282** (1997) 1.

[48] D. Chirkin and W. Rhode, *Muon Monte Carlo: A new high-precision tool for muon propagation through matter*, 2002, DESY-PROC-2002-01.

[49] J. Christiansen, *32 Channel general purpose Time to Digital Converter*, 1997, CERN/ECP-MIC.

[50] G. Cowan, "Statistical Data Analysis", (Oxford University Press, 1998).

[51] G. D'Agostini, Nucl. Instr. and Meth. **A362** (1995) 487.

[52] M. P. De Pascale et al., J. Geoph. Res. **98** (1993) 3501.

[53] H. J. Drescher et al., Phys. Rep. (2001) 93.

[54] P. Duinker et al., Nucl. Instr. and Meth. **A273** (1988) 814.

[55] R. Engel, T. K. Gaisser, and T. Stanev, Phys. Lett. **B472** (2000) 113.

[56] R. Engel et al., Proc. 26th ICRC (1999) 415.

[57] R. Engel et al., Proc. 27th ICRC (2001) 1381.

[58] M. Fabre, *The dimuon mass resolution of the L3 experiment at LEP* , Ph.D. thesis, ETH–Zürich, 1992.

[59] E. Fermi, Phys. Rev. **75** (1949) 1169.

[60] H. Fesefeldt, Report (1985), RWTH Aachen.

[61] R. S. Fletcher et al., Phys. Rev. **D50** (1994) 5710.

[62] W. R. Frazer and C. H. Poon, Phys. Rev. **D5** (1972) 1653.

[63] Y. Fukuda et al., Phys. Rev. Lett. **81** (1998) 1562.

[64] T. K. Gaisser, "Cosmic Rays and Particle Physics", (Cambridge University Press, 1990).

[65] T. K. Gaisser and M. Honda, Ann. Rev. of Nucl. Part. Sci. **52** (2002) 153.

[66] R. L. Glückstern, Nucl. Instr. and Meth. **24** (1963) 381.

[67] P. J. Green et al., Phys. Rev. **20** (1979) 1598.

[68] K. Greisen, Phys. Rev. Lett. **16** (1966) 784.

[69] V. N. Gribov, Sov. Phys. JETP **26** (1968) 414.

[70] N. L. Grigorov et al., Proc. 12th Int. Cosmic Ray Conf. (Hobart) **5** (1971) 1760.

[71] H. L. Groenstege et al., *NIMROD, the ROD for the Monitored Drift Tubes in ATLAS*, 1996, ETR 96-09.

[72] H. L. Groenstege et al., *Cosmic Personality Card for the L3+Cosmics experiment*, 1999, ETR 99-02.

[73] H. L. Groenstege et al., *The NIMROD*, 1999, ETR 99-06.

[74] D. E. Groom et al., Atom. Data Nucl. Data Tabl. **78** (2001) 183.

[75] K. Hagiwara et al., Phys. Rev. **D66** (2002) 10001.

[76] T. Hebbeker, *The effective atmospheric temperature*, 2000, L3+C internal note.

[77] T. Hebbeker, *Atmospheric temperature data for the year 2000*, 2001, L3+C internal note.

[78] T. Hebbeker and A. Korn, *Simulation Programs for the L3+C Experiment*, 1998, L3+C internal note.

[79] T. Hebbeker and C. Timmermans, Astropart. Phys. **18** (2002) 107.

[80] D. Heck et al., Forschungszentrum Karlsruhe **FZKA 6019** (1998).

[81] V. F. Hess, Phys.Zeitschr. **13** (1912) 1084.

[82] A. Höcker and V. Kartvelishvili, Nucl. Instr. and Meth. **A372** (1996) 469.

[83] M. Honda et al., Phys. Rev. **D52** (1995) 4985.

[84] V. Innocente and E. Nagy, Nucl. Instr. and Meth. **A324** (1993) 297.

[85] V. Innocente et al., *GEANE: Average Tracking and Error Propagation Package*, 1991, CERN W5013 - E GEANE.

[86] S. Jadach et al., Comput. Phys. Commun. **79** (1994) 503.

[87] F. James, *MINUIT Reference Manual*, 1994, CERN D506.

[88] C. K. Jung et al., Ann. Rev. of Nucl. Part. Sci. **51** (2001) 451.

[89] N. Kalmykov et al., Nucl. Phys. **B (Proc. Suppl.)** (1997) 7.

[90] V. Karimäki, Nucl. Instr. and Meth. **A305** (1991) 187.

[91] A. Korn, *Cosmic muons in the L3 detector*, Diploma thesis, Humboldt-University, Berlin, 1998.

[92] J. Kremer et al., Phys. Rev. Lett. **83** (1999) 4241.

[93] G. V. Kulikov and G. B. Khristiansen, JETP **35** (1959) 3.

[94] L3 muon chamber group, Nucl. Instr. and Meth. **A277** (1989) 187.

[95] L3 muon chamber group, Nucl. Instr. and Meth. **A289** (1989) 335.

[96] L3 muon chamber group, Nucl. Instr. and Meth. **A290** (1990) 115.

[97] L3 muon chamber group, Nucl. Instr. and Meth. **A323** (1992) 109.

[98] P. G. Ladron, *The 'good-bad guys' selection*, 2000, L3+C internal note.

[99] G. D. Lafferty and T. R. Wyatt, Nucl. Instr. and Meth. **A355** (1995) 541.

[100] P. O. Lagage and C. Cesarsky, Astron. Astrophys. **118** (1983) 223.

[101] H. Leich, *GPSTIM User's Guide*, 1998.

[102] H. Leich, *L3CD User's Guide*, 1998.

[103] L. Li, *Cross-octant reconstruction program*, 2002, L3+C internal note.

[104] L. Lindemann and G. Zech, Nucl. Instr. and Meth. **A354** (1995) 516.

[105] P. Lipari, Astropart. Phys. **B214** (1988) 147.

[106] Z. Liu, *Z^0 Data Analysis in the L3+Cosmics experiment*, 2000, L3+C internal note.

[107] W. Lohmann et al., *Energy loss of Muons in the Energy range 1-10000 GeV*, 1985, CERN Report 85-03.

[108] X. Ma, *T0 calibration*, 2002, L3+C internal note.

[109] K. Medea, Fortschr. Phys. (1973) 113.

[110] W. Menn et al., ApJ **533** (2000) 281.

[111] A. Mill, *Cosmic ray muons in the L3 detector* , Ph.D. thesis, University of Nijmegen, 2001.

[112] M. Nagano et al., J. Phys. **G18** (1992) 423.

[113] R. Nahnhauer, private communication.

[114] S. H. Neddermeyer and C. D. Anderson, Phys. Rev. **51** (1937) 884:886.

[115] J. Onvlee, *The behaviour of the L3 muon chambers in a magnetic field* , Ph.D. thesis, University of Amsterdam, 1989.

[116] B. Petersen and T. A. M. Wijnen, *L3 COSMICS Data Aquisition*, 1998, L3+C internal note.

[117] B. Peterson, *The cosmic ray induced muon spectrum*, Ph.D. thesis, University of Nijmegen, 2002.

[118] R. Ramelli, *Search for Cosmic Ray Point Sources and Anisotropy Measurement with the L3+C Detector*, Ph.D. thesis, ETH Zürich, 2002.

[119] J. Ranft, Phys. Rev. (1995) 64.

[120] T. Regge, Nuovo Cim. **14** (1959) 951.

[121] S. Sagisaka, Phys. Rev. **95** (1954) 1573.

[122] T. Sanuki et al., ApJ **545** (1135) 545.

[123] V. Schmitt, *Analysis of multi muon events in the L3 detector* , Diploma thesis, Humboldt-University, Berlin, 2000.

[124] E. S. Seo et al., ApJ **378** (1991) 763.

[125] Service de Climatologie, Geneva.

[126] T. Sjöstrand, Comput. Phys. Commun. **82** (1994) 74.

[127] J. Sullivan, Nucl. Instr. and Meth. **95** (1971) 5.

[128] S. Swordy, `PAW` macro available at `http://astroparticle.uchicago.edu/cosmic_ray_spectrum_picture.htm`.

[129] A. N. Tikhonov, Sov. Math. **5** (1963) 1035.

[130] C. Timmermans, *TDC efficiency calculations for L3C*, 2003, L3+C internal note.

[131] M. Unger, *Detection of cosmic muons with scintillating tiles on top of the L3 detector* , Diploma thesis, Humboldt-University, Berlin, 1998.

[132] M. Unger, *Muon chamber alignment*, 2001, L3+C internal note.

[133] M. Unger, *L3+C scintillator efficiencies*, 2002, L3+C internal note.

[134] J. Utecht, *Low energy muons in the L3 detector*, Diploma thesis, Humboldt-University, Berlin, 2002.

[135] H. Verkooijen, *CTT-V2*, 1999, ETR 99-01.

[136] J. A. M. Vermaseren et al., Phys. Rev **D19** (1979) 137.

[137] J. . Wentz et al., Phys. Rev. **D67** (2003) 73020.

[138] K. Werner, Phys. Rep. (1993) 87.

[139] H. Wilkens, *Experimental study of high energy muons from Extensive Air Showers in the energy range 100 TeV to 10 PeV* , Ph.D. thesis, University of Nijmegen, 2003.

[140] H. Wilkens, private communication.

[141] G. T. Zatzepin and V. A. Kuzmin, Zh. Eksp. teor. Fiz. **4** (1966) 114.

ACKNOWLEDGMENTS

First of all I would like to thank my supervisor Rolf Nahnhauer for his continuous support and the time and attention he spent to discuss this analysis with me as it developed.

I am grateful to Thomas Hebbeker for introducing me to the L3+C experiment and for his critical remarks throughout the last years, which helped to improve this work substantially.

It was a pleasure to work with Rudolf Leiste, with whom I had many fruitful discussions on the details of the scintillator data and who helped me a lot running the L3+C MC production in Zeuthen.

Within the experiment, Pierre LeCoultre always managed to create a very pleasant working atmosphere. I would like to thank him for his patience during the ups and downs of the L3+C offline work.

This analysis gained a lot from the constructive competition with the Nijmegen muon spectrum group, Bert Peterson and Charles Timmermans.

Furthermore, the discussions with Henric Wilkens about the data reconstruction and with Simon Blyth about the L3 luminosity were of great help.

The development of the double octant fit and the detector alignment procedure would not have been possible without the technical support from Zhiguo Yao, who did a great job steering the data mass production at CERN.

Moreover, I would like to thank Ralph Engel for providing the `TARGET` program and for the time he spent answering all my questions about it.

Finally, I would like to thank my sister Tina for carefully reading this manuscript and Janis Meyer for checking the formulae.

This work is dedicated to the memory of Uta Unger.

Erklärung

Hiermit bestätige ich, die Dissertation selbständig und ohne unerlaubte Hilfe angefertigt zu haben.
Ich habe mich anderwärts nicht um einen Doktorgrad beworben und besitze einen entsprechenden Doktorgrad nicht.
Ich erkläre die Kenntnisnahme der dem Verfahren zugrunde liegenden Promotionsordnung der Mathematisch-Naturwissenschaftlichen Fakultät I der Humboldt-Universität zu Berlin.

Berlin, den 1. Oktober 2003

Michael Unger